SPATIAL, TEMPORAL AND PHYSICAL ORIGIN OF MATRIX-POOR TO MATRIX-RICH SANDSTONES, NEOPROTEROZOIC, WINDERMERE SUPERGROUP, BRITISH COLUMBIA, CANADA

by

Curran Wearmouth

Thesis submitted to in partial fulfillment of the requirements for the
MSc degree in Earth Science

Department of Earth and Environmental Sciences

Faculty of Science
Ottawa-Carleton Geoscience Centre
University of Ottawa

Abstract

At the Castle Creek study area a remarkably well exposed section in the Isaac Formation, Windermere Supergroup, was measured to document potential lateral and vertical changes in facies. Here, a consistent lateral succession of facies was observed consisting of matrix-poor sandstone to clayey sandstone to bipartite bed to sandy claystone, collectively overlain by a thin-bedded turbidite and mudstone cap. These changes are interpreted to reflect particle settling in a negligibly-sheared sand-mud suspension following detachment from the margins of an avulsion jet. Vertically, similar facies stack to form packages 2-7 beds thick implying temporary stabilization of jet-margin dynamics. At a larger scale facies stack to form three stratal assemblages. SA-1: intercalated matrix-rich and matrix-poor strata and SA-2: matrix-rich strata stack vertically and laterally but then are sharply overlain everywhere by classical turbidites of SA-3, indicating a dramatic change from deposition immediately downflow of an avulsion node to conventional levee deposition.

Résumé

Une section remarquablement bien exposée de la Formation Isaac, du supergroupe Windermere d'âge Néoprotérozoïque, a été mesurée pour décrire les changements potentiels latéraux et verticaux de faciès. Une tendance latérale de faciès a été observée, étant un grès avec peu de matrice à un grès argileux à un lit de grès (« bipartite ») à un claystone sableux qui sont collectivement surmontés par une turbidite à lits-minces et un mudstone. Ces changements sont interprétés comme reflétant la déposition de sable et de boue par suspension après le détachement des bords d'un jet d'avulsion. Les faciès sont semblables verticalement et sont empilés en paquets 2-7 lits d'épais suggérant la stabilisation temporaire de la dynamique des jets. Dans un contexte à plus grande échelle, les faciès s'empilent pour former trois assemblages stratales. SA-1 : strates intercalés à matrice argileuse, et avec peu de matrice, SA-2 : strates à matrice argileuse qui s'empilent verticalement et latéralement, ensuite surmontés partout par des turbidites typiques de SA-3 indiquant un changement soudain de déposition immédiatement en avant du « avulsion node » résultant en un dépôt de levée plus conventionnel.

Extended Abstract

At the Castle Creek study area a remarkably well-exposed section in the Isaac Formation, Windermere Supergroup, was measured in bed-by-bed detail to document changes in facies and facies association – note that matrix is considered to consist of silt or finer sediment. Based on these data five facies are recognized: F1.A) medium-bedded, scour-based, matrix-poor (<20% matrix), normally graded, structureless sandstone; F1.B) medium- to thin-bedded, scour-based to wavy-based, massive, matrix-intermediate (20-50%) structureless clayey sandstone; F2) medium- to thin-bedded, flat-based, matrix-rich (50-70%), massive, structureless sandy-claystone; F3.A) thin-bedded, fine sand to silt, traction-structured sandstone; F3.B) thin- to thick bedded, flat-based, planar and/or ripple cross-stratified, medium to fine sand sandstone, and F4) massive to graded mudstone. Mudstone intraclasts are common in F1.A, F1.B, and F2.

Laterally these facies exhibit a systematic change from matrix-poor (F1.A) to more matrix rich (F2) strata. Specifically, matrix-poor sandstone (F1.A) grades laterally into clayey sandstone (F1.B). Further laterally, the clayey sandstone becomes sharply overlain by a sandy claystone (F2). Collectively, these two parts, which are separated by a sharp planar surface, form a single bipartite bed. Laterally, the lower clayey sandstone thins and then pinches out, at which point the upper sandy claystone (F2) comprises the entire bed. Nevertheless, further laterally it too thins and then pinches out. Finally, the entire transect is draped by a traction-structured sandstone (F3.A) capped by mudstone (F4).

Stratigraphically upward, like facies typically succeed one another and form packages comprising 2 up to 7 beds. Additionally, beds within each package exhibit similar lithology and thickness. At a larger scale (several meters), packages stack vertically to form three distinctive

stratal assemblages: SA-1) made up of a single bed or stack of matrix-poor sandstone that is then overlain sharply by 1 to 2 packages of exclusively matrix-rich strata (clayey sandstone, bipartite beds, or sandy claystone) and collectively form dm- to m-thick bedsets that then repeatedly stack to form a 1.5-4.5 m thick assemblage; SA-2 is composed exclusively of matrix-rich packages (clayey sandstone, bipartite beds, and sandy claystone) that build assemblages up to 2.0 m thick; (SA-3) consists of classical (matrix-poor) turbidites that stack to form assemblages 2-6 m thick. Vertically, SA-1 and SA-2 stack and are sharply bounded by successions consisting exclusively of traction-structured turbidites (SA-3). Additionally, SA-1 transitions laterally to more distal facies and then into SA-2.

As suggested by other studies (Terlaky and Arnott 2014) and Angus (2016), deposition of the strata described here are related to vortex shedding from the lateral margins of a turbulent jet related to an upflow channel avulsion. The lateral facies change from matrix-poor (F1.A) to matrix-intermediate (F1.B) to matrix-rich (F2) strata is interpreted to reflect deposition from a negligibly-sheared, sediment-laden plume that became separated from the main avulsion flow. The now detached, negligibly-sheared suspension advected away from main jet and immediately began to collapse. Initially, the upward component of turbulence was the primary sediment support mechanism, enabling particles to settle according to their fall velocity. However, as the suspension moved further away from the main jet and collapsed toward the bed, hindered settling became increasingly important and eventually became the primary sediment support mechanism. Specifically, the downward (constant) mass flux of settling particles resulted in the upward displacement of ambient fluid and easily suspended fine-grained sediment and low-density mud clasts. The buildup of this fine sediment in the upper part of the collapsing suspension formed the sharply defined sandy clay(stone) layer in the upper part of a bipartite bed. Eventually the

basal part of the suspension became completely depleted of settling sediment through deposition as the upper part continually accumulated clay and developed cohesive matrix strength. The now exclusively mud-rich flow resembled a viscous plug flow, which like the now deposited basal layer, thinned and then pinched out. At all times the suspension was overlain by a low-density turbidity current that formed a well-sorted, traction-structured layer made up of sediment reworked from the underlying deposit (i.e. lateral facies succession). Lastly, any clay that remained in suspension settled forming a near-bed fluid mud layer that eventually gelled depositing a mudstone cap (F4) that marks the end of a single sedimentation event.

Vertically, deposition begins with the emplacement of a coarse, graded sandstone (F1.A) related to the local introduction of a single high-energy, sediment-laden vortex. This is then abruptly followed by a dramatic contraction of the jet margin and the episodic detachment of self-similar vortices that deposited a 2-7 bed-thick package made up of similar facies. Importantly, time between successive depositional events (i.e. each bed) was of sufficient duration to allow for the emplacement of the structured sandstone and overlying mudstone cap. At an even larger scale, the lateral and vertical juxtaposition of SA-1 and SA-2 is interpreted to reflect the abrupt lateral displacement of the axis of the main avulsion jet followed by a period of temporary stabilization. These avulsion-related strata are then abruptly overlain by a thick stack of classical turbidites (SA-3), which suggests that sedimentation downflow of the avulsion node ceased, most probably due to a upflow avulsion, and as a consequence a return to more typical extrachannel deposition, specifically levee growth. Alternatively, the abrupt superposition of SA3 turbidites could reflect the depletion of a locally erodible mud-rich sea floor, quite possibly due to scour down to a sufficiently compacted subsurface layer, or simply being buried in sand.

Acknowledgements

This work would not have been possible, nor as enjoyable, without the collaboration and support from the many people with whom I had the pleasure to work alongside. Firstly, I would like to profoundly thank my supervisor Dr. Bill Arnott for his never-ending support, collaboration, and mentorship. I consider myself extremely fortunate to have worked under his supervision. He taught me a great deal, beyond the scope of any textbook, and he continuously fuelled my passion for geology with his enthusiasm.

Significant thanks to Dr. Don Cummings and Dr. Quinten Gull for reviewing my thesis. Their questions and comments challenged me to consider my work from a different perspective and greatly improved the final product of this study.

Thank you to the Windermere Consortium as well as the University of Ottawa for financially supporting this research project, as well as many others. Their continued contributions enable the rigors of deep-marine sedimentology research, which build an ever-expanding and reliable body of knowledge.

A great number of thanks to Anika Bergen, Dylan Cochrane, Celeste Cunningham, Quinn Dabros, Genevieve Huyer, Leo Lee, Dave Lowe, Sean Ludzki, Derrick Midwinter, Lilian Navarro, Jag Ningthoujam, Nataša Popović, Kristina Schmidt, Viktor Terlaky, and Mike Tilston for your questions, words of advice, and insightful comments. I'm extremely lucky to have worked with a team of so many talented and encouraging geologists. A very special thanks to Katrina Angus for early mentorship and Gabriela Milczarek for her field support. This study would not have been the same without their assistance and collaboration.

Thank you to Alain Mauviel and George Mrazek for creating the many fantastic thin sections I required for this study. Thank you to Hélène De Gouffe, Lisa-Robin Murphy, and Caroline Bisson for their very kind support in the department.

Thank you to the McKirdy family for their logistical support in the field. Their help and expertise enabled me, as well as many others, to live out the sedimentologist's dream at beautiful Castle Creek.

Many thanks to Petar Vidjen and Will Tuer for their encouraging and generous support.

Finally, I would like to give a very sincere thank you to everyone that offered their kindest support to me and my family after the tragic passing of my beloved little sister Josie – I cannot thank you all enough for your help.

Dedication

To Josie, Tessa, Ian, Brian, Shelley and Greg.

Thank you for your everlasting love.

"They is my family…"

-Mother Mother

Table of Contents

List of Figures

List of Tables

1 Introduction

1.1 Thesis Rational

Few modern deep-marine sedimentary systems have been extensively explored, which in large part can be attributed to their inaccessibility and enormous spatial scale. These challenges make them arguably the most difficult sedimentary systems to study (Arnott 2010). Uncertainties are especially significant for sedimentologists working in the ancient deep-marine sedimentary record who are challenged not only with describing and correlating the preserved stratigraphic record, but also interpreting the formative physical processes that build up the largest depositional features on Earth (Bouma 1985). From an economic point of view these expansive, sand-rich systems host significant petroleum reserves that currently are being actively investigated for hydrocarbon exploration and production (Pettingill and Weimer 2002), which provides incentive to better understand reservoir geometry and connectivity of sandstone bodies (reservoirs) within them.

Fortunately, with recent improvement in 2D and 3D seismic acquisition and resolution, in addition to borehole data from the petroleum industry, significant advancements have been made in understanding the deep-marine sedimentary record (see form example, Posamentier and Kolla 2003, Posamentier and Walker 2007). Nevertheless, the poor vertical resolution of industry seismic (i.e. at subsurface depths where hydrocarbon reservoirs occur) and the limited lateral dimension of core requires data from outcrops to help merge these two spatially disparate data sets (Arnott 2010). Accordingly, studies like this one will help to improve our understanding of

deep-marine sedimentary systems, and therein reduce risk and improve predictability in subsurface petroleum exploration and production.

Sediment-gravity flows, namely turbidity currents and debris flows, in addition to mass movement processes, are the dominant mechanisms that transfer sediment into the deep sea. In nature, flows may mobilize as much as hundreds of cubic kilometres of sediment into the deep-marine environment during a single transport event (Normark and Piper 1991), but being relatively infrequent, unpredictable, inaccessible and often highly destructive, observing and measuring them in-situ is problematic. Accordingly, much of our knowledge of their physical mechanics has been developed through the description and interpretation of their deposits in both the modern and ancient sedimentary record (Mulder and Alexander 2001).

Since the pioneering work of Kuenen and Migliorini (1950) on the origin of graded bedding, and the description of the stratigraphic makeup of complete and partial turbidites (Bouma 1962, Lowe 1982), much has been learned about the sand-rich part of the deep-marine sedimentary record. Less well known are deep-marine sandstones rich in detrital fine-grained (i.e. mud) matrix, which include strata termed argillaceous sandstones (Enos 1969), slurry beds (Lowe and Guy 2000), linked debrites (Haughton et al. 2003), hybrid event beds (Haughton et al. 2009a), co-genetic turbidite-debrites (Talling et al. 2004), transitional flow deposits (Kane and Pontén 2012), and matrix-rich sandstones (Terlaky and Arnott 2014). In addition to the plethora of terms to describe these strata are the many proposed physical mechanisms responsible for their deposition. Much uncertainty arises because many of the examples are described from core or from discontinuous and generally poorly exposed outcrops; and, as such, details of any vertical, and especially, lateral variability, are generally unknown. Exceptional exposures of matrix-rich sandstones at the Castle Creek study area permit centimetre- to millimetre-scale

observations to be carried out over distances of 10's of metres vertically, but more significantly, 100's of metres laterally. This, then, provides an unparalleled opportunity to accurately investigate the textural, lithological, and mineralogical composition of matrix-rich sandstone deposits both vertically and laterally, and ultimately details of their vertical stacking architecture.

1.2 Thesis Objectives

The primary goal of this thesis is to 1) provide detailed facies descriptions and interpretations of matrix-rich and associated matrix-poor sandstones, 2) delineate lateral facies changes, in addition to evaluating the vertical stacking patterns of matrix-rich and associated matrix-poor sandstones, and 3) present a depositional model for the origin and evolution of the studied section.

1.3 Study Area

The Castle Creek study area (Figure 1-1), hereafter referred to as Castle Creek, is located in the northern Cariboo Mountains, eastern British Columbia. At Castle Creek, rocks of the Neoproterozoic Windermere Supergroup, specifically deep-marine basin floor deposits of the Upper Kaza Group and overlying slope deposits of the Isaac Formation are well exposed. The sedimentary sequence is nearly vertically dipping (~89˚) and is over ~2.5 km thick and has a ~7 km strike length. In addition, recent (<100 years) deglaciation has exposed strata that are generally free of debris and vegetation, which then provides the opportunity to confidently trace

individual beds not only vertically, but uninterrupted over 100's of metres laterally (Ross and Arnott 2007).

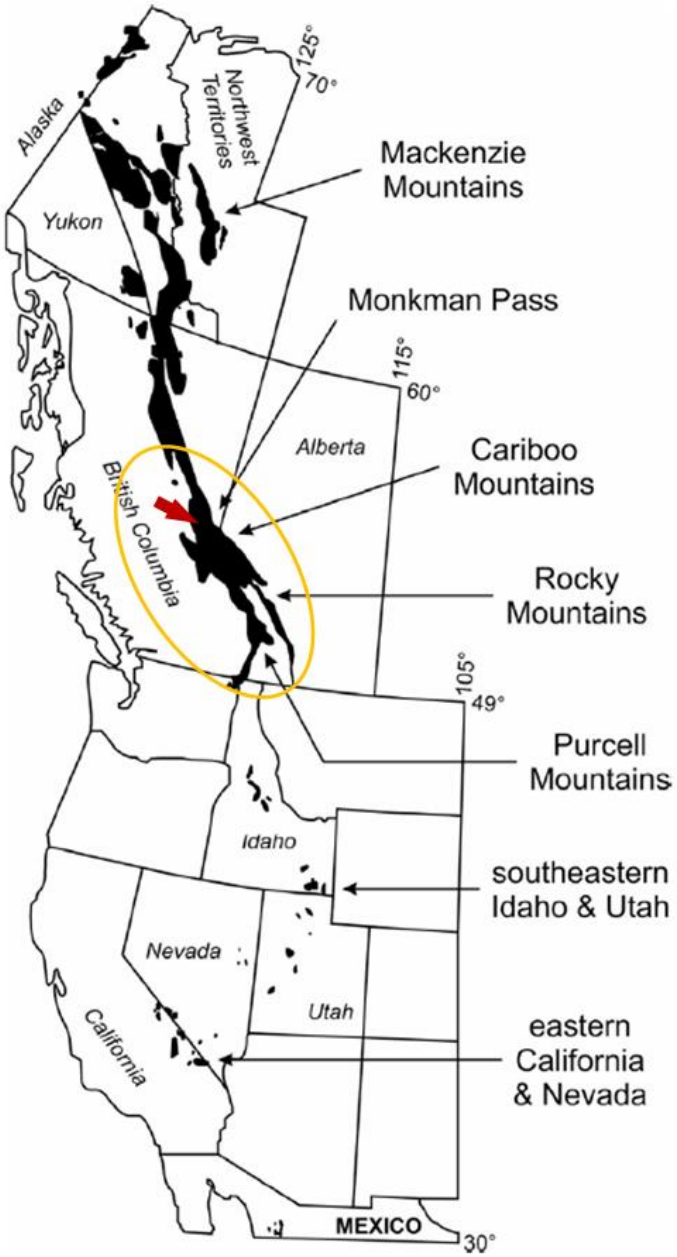

Figure 1-1 Distribution of exposed Windermere Supergroup strata in western North America. **Red arrow** indicates the study area location (50°03'17.43" N, 120°26'56.21"W). Orange oval designates the deep-marine portion of the Windermere Supergroup in the southern Canadian Cordillera (modified after Smith et al. 2014; from Ross 1991)

1.4 Regional Geology of the Windermere Supergroup in the Southern Canadian Cordillera

The Windermere Supergroup is an unconformity-bounded, several-kilometer-thick succession of Neoproterozoic sedimentary rocks that forms a discontinuous outcrop belt extending from Mexico to the Yukon-Alaska border (Stewart et al. 1972, Ross et al. 1989, Link 1993) (Figure 1-1). The Windermere sedimentary basin is interpreted to have formed during the rifting of the supercontinent Rodina, followed by sedimentation on the thermally-relaxed passive margin of Laurentia (Stewart 1972, Ross 1991). This two-stage tectonic history is recognized in two, few- to several-km-thick stratal assemblages. In the southern Canadian Cordillera, the first assemblage is a regionally discontinuous succession of mafic volcanic rocks and glaciogenic diamictites that, in southeastern B.C., are termed the Irene and Toby formations, respectively (Root 1987). These deposits are overlain by a second regionally extensive assemblage of basin floor deposits that shallows gradually over several kilometres to continental shelf deposits of the Yankee Belle Formation – a consequence of long-term progradation of the Laurentian continental margin into the proto-Pacific miogeocline (Stewart et al. 1972, Ross 1991, Ross and Arnott 2007). Alternatively, other authors, specifically Thompson et al. (2006), suggested that the deep-water Windermere basin was instead separated from the miogeocline (to the west) by an elevated area termed the Okanagan high, and that the final breakup and formation of a passive margin took place later and along the western margin of the Okanagan high.

Later, during the Mesozoic and Cenozoic, the Windermere's original miogeoclinal geometry was significantly altered by the Cordilleran Orogeny and its associated crustal thickening and metamorphism. In the southern Canadian Cordillera, rocks of the Windermere

Supergroup are exposed in the Main Ranges of the Western Fold-and-Thrust Belt and Omineca Belt – these two tectono-physiographic regions are separated by the Southern Rocky Mountain Trench (Stewart et al. 1972, Ross and Hein 1989, Link 1993). The exposed part of the deep-marine Windermere turbidite system in the southern Canadian Cordillera crops out over an area of 35,000 km^2 which, if conservatively palinspastically restored, would cover an area over 80,000 km^2, and therein make it dimensionally similar to the modern and economically important Mississippi and Amazon fans (Ross and Arnott 2007).

1.4.1 Terminology

Due to Mesozoic tectonism rocks of the Windermere Supergroup have undergone low (greenschist) to high (amphibole) grade metamorphism, and therefore are strictly metasedimentary rocks. However, in areas of low grade metamorphism, such as at Castle Creek, primary sedimentary features and textures are well preserved, enabling rocks to be described and classified using conventional sedimentary terminology (Ross and Arnott 2007).

1.4.2 Stratigraphic Nomenclature and Regional Markers

Regional correlation of Windermere Supergroup strata has proven challenging primarily due to its immense areal extent, structural complexity, and general paucity of biostratigraphic control. Nevertheless, in the southern Canadian Cordillera, three regionally extensive lithostratigraphic markers are recognized. The stratigraphically lowest is the Old Fort Point Formation that forms a regional marker across the entire Windermere deep-water basin (Ross et al. 1989, Smith et al. 2014). The Old Fort Point Formation ranges from 60 to 450 m, and stratigraphically upward comprises the Temple Lake, Whitethorn Mountain and Geikie Siding

members. The depositional age of the Old Fort Point Formation is constrained by a Re-Os date of 607.8 ±4.7 Ma, and is interpreted to have formed as a result of a major sea-level rise caused by the melting of the Marinoan ice sheet (Kendall et al. 2004).

Above this, two lithostratigraphic marker units occur in the Isaac Formation that are informally termed the first and second Isaac carbonates. They consist of silty to sandy limestone turbidites, marl-rhythmites, and mass-movement deposits (Ross and Murphy 1988, Ross and Arnott 2007) related to highstand shedding of carbonate detritus from a mixed shallow shelf siliciclastic-carbonate platform, which episodically completely terminated siliciclastic input and deposited only pure calci-turbidities (Navarro 2016).

Despite these regionally extensive markers, detailed basin-wide correlation remains difficult, and accordingly has led to the development of a diversity of stratigraphic names (see Figure 1-2) that generally are geographically specific (Smith et al. 2014). For example, in the southern Canadian Cordillera, high-order stratigraphic names for strata of the Windermere Supergroup include Horsethief Group in the Selkirk and Purcell Mountains, Miette Group in the western Rockies, and Kaza and Cariboo groups in the Cariboo Mountains (Ross and Arnott 2007, Smith et al. 2014), in addition to myriad lower order formation names.

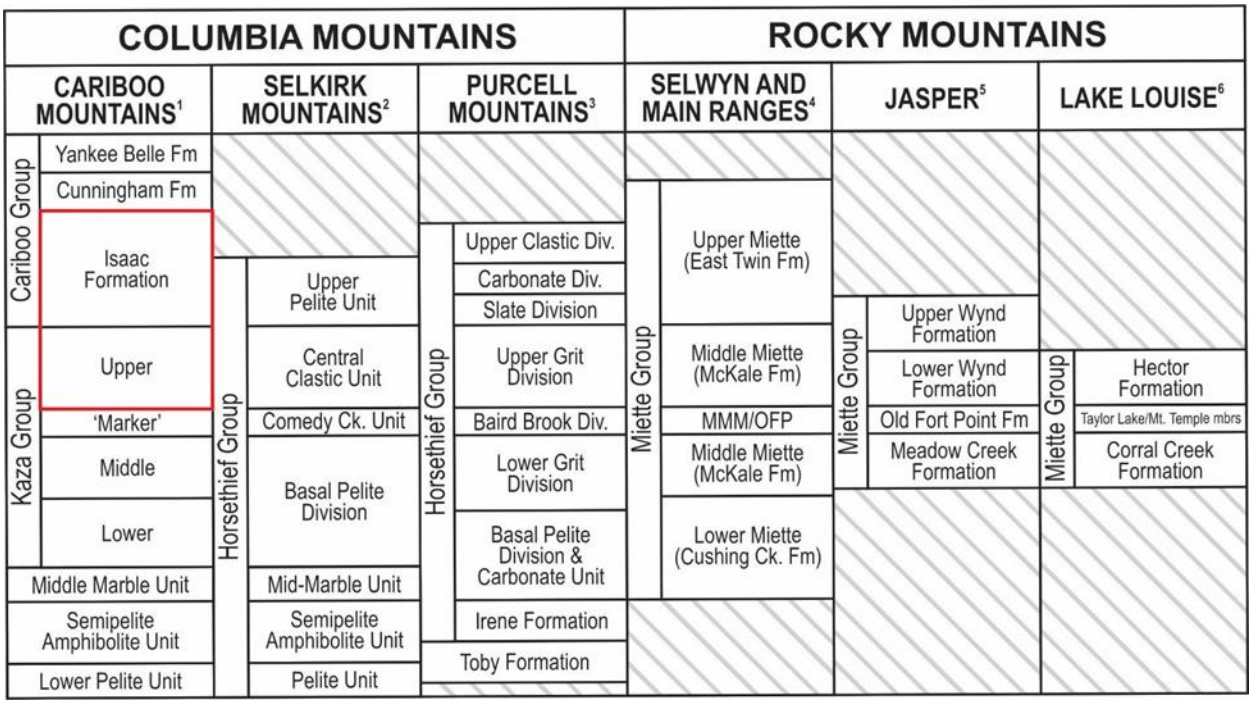

Figure 1-2 Stratigraphic nomenclature of the Windermere Supergroup, southern Canadian Cordillera. Sources include: 1) Campbell et al. 1973, Ferguson 1994, Ross and Ferguson 2003a, 2003b); 2)Grasby and Brown 1993);3)Kubli 1990, 1994, Kubli and Simony 1992, Warren 1996, 1997); 4) (McDonough 1989, Ross et al. 1989, McDonough and Murphy 1994) 5) (Charlesworth et al. n.d Charlesworth and Remington 1960); 6)(Walcott 1910, Gussow 1956, 1957, Aitken 1969; from Smith et al. 2014)

1.4.3 Geochronology

Due to a general lack of suitable lithologies for radiometric dating, as well as sparse Ediacaran biostratigraphy, the absolute age of the Windermere Supergroup is poorly constrained (Ross and Murphy 1988). Nonetheless, the onset of Windermere Supergroup sedimentation is younger than 728 +8/-7 Ma to 740 ± 36 Ma based on U-Pb dates of zircons from granitic gneisses that unconformably underlie the Windermere Supergroup (Evenchick et al. 1984, Parrish and Scammell 1988). In addition, mafic metavolcanic rocks in northeastern Washington, interpreted to be correlative to the Toby Formation in southeastern B.C., were dated at 762 ± 44

Ma from a Sm-Nd isochron (Devlin et al. 1988) The range of reported dates that occur at or near the base of the Windermere Supergroup differ along the Canadian Cordillera, suggesting that the onset of deposition differed along and across the axis of the rifted margin, possibly in stepwise events (Evenchick et al. 1984). Additional dates in the rift assemblage include U-Pb ages from felsic volcanics in central Idaho, which correlate with the Irene Formation in the southeastern B.C. and provide an age of 685 Ma ± 7 Ma (Lund et al. 2003). To date, the only date from rocks in the deep-water Windermere basin is from a Re-Os analysis of organic rich mudstones in the Old Fort Point Formation, specifically the Geike Siding Member, and suggests an age of 607.8 ± 4.7 Ma (Kendall et al. 2004, Smith et al. 2014). Unconformably overlying the Windermere Supergroup are volcanic rocks of the Hamill Group that have yielded a U-Pb zircon age of 570 ± 5 Ma (Colpron et al. 2002), and therein a maximum age for Windermere sedimentation.

1.4.4 Sediment Provenance

Detrital zircons from the Windermere Supergroup exhibit a bimodal U-Pb age distribution: Archean (2.6-3.3 Ga) and Early Paleoproterozoic (1.7-1.9 Ga). In this area of western North America, potential sediment sources include basement rocks of the Rimbey granites, Loverna Domain, and Medicine Hat Block located to the east-southeast (Ross and Parrish 1991). Dates from granitic dropstones in the Toby Formation also suggest a westerly source from the Monashee complex (Thompson et al. 2006). Sparse paleocurrent data collected from the Windermere indicate a general transport direction toward the north-northwest, consistent with a suggested sediment source to the southeast (Arnott and Hein 1986, Ross et al. 1989).

1.4.5 Stratigraphy

The Windermere Supergroup unconformably overlies meta-sedimentary rocks of the 1.5-1.4 Ga Belt-Purcell Supergroup (Evans et al., 2000) , or crystalline basement that ranges between 2.2 Ga to 0.7 Ga (Crowley 1999). The unconformity is interpreted to have formed during the Late Precambrian breakup of the supercontinental Rodinia (Stewart et al. 1972, Ross and Parrish 1991, Ross and Arnott 2007) and is overlain by an assemblage of rift related rocks of the Toby and Irene formations (Figure 1-3). The Toby Formation ranges from a few meters to over ~1800 m thick and is composed of thickly-bedded or lenticular masses of diamictite, with lesser intercalated conglomerate, sandstone, and argillite (Aalto 1971). Diamictites of the Toby Formation have been interpreted to be of glacial or glacial marine origin (Aalto 1971) and are attributed to the Sturtian glaciation (~700-750 ma) (Ross et al. 1995). Mafic igneous rocks of the Irene Formation, specifically pillowed volcanic flows, tuffs, tuff breccias and sills (Aalto 1971) overlie, and in places, interfinger with the Toby Formation, inferring synchronous igneous activity and accumulation during active rifting (Stewart 1972, Ross et al. 1995).

In the Cariboo Mountains, rocks of the rift assemblage are conformably overlain by a ~2-4 km thick succession of deep-water rocks of the Kaza Group, which represents the initial deposits along the thermally subsiding passive margin of Laurentia. The Kaza Group is subdivided into Lower, Middle, and Upper parts, in addition to the Old Fort Point Formation (see above), which separates the Middle and Upper parts of the Kaza Group. The Kaza Group is composed mostly of sheet-like feldspathic sandstone and mudstone (i.e. thin-bedded turbidites), and at least in the Middle and Upper Kaza group has a sandstone to mudstone ratio that ranges up to 75:25 (Ross and Arnott 2007). Sheet-like sandstones are interpreted to represent the

expansive sand-rich parts of depositional lobe complexes intercalated with mud-rich inter- and intra-lobe strata and rare laterally discontinuous debrites (Terlaky et al. 2016).

The Kaza Group is then conformably overlain by the ~1.5 km thick Isaac Formation, which is composed mostly of mudstone and lesser sandstone – sandstone to mudstone ratio of 25:75 (Ross and Arnott, 2007). Much of the finer-grained facies of the Isaac Formation represent levee and related inter-channel stratal elements (Ross and Arnott 2007, Davis 2011). These are interstratified and/or occur adjacent to coarse grained sandstone units interpreted to be continental slope channel complexes (Dumouchel 2015). Moreover, the commonality of mass-movement deposits in the Isaac Formation, compared to their rarity in the Kaza Group, suggests conditions of increased gravitational instability consistent with a continental slope setting (Ross and Arnott 2007).

Although the Isaac Formation is principally siliciclastic, sedimentation is interrupted episodically by the influx of carbonate detritus. Two regionally identifiable markers, the aforementioned first and second Isaac carbonates, occur within the Isaac Formation and consist mostly of silty to sandy limestone turbidites, marl-rhythmites and common mass-movement deposits including slides, slumps, and debrites.

The Cunningham Formation conformably overlies the Isaac Formation and is composed mostly of limestone with lesser dolostone, shale, siltstone, and sandstone, and reaches a maximum thickness of ~550 m (Brown et al. 1978, Gabrielse and Campbell 1991). The Cunningham Formation is interpreted to have recorded the evolution from a ramp to rimmed platform. The Cunningham Formation, in turn, is conformably overlain by the ~900 m thick Yankee Bell Formation composed of shale and siltstone with minor quartzite and limestone. The

Yankee Bell Formations has been interpreted to have accumulated on a high energy, shallow marine shelf (Ross et al. 1995).

An unconformity separates the Windermere Supergroup from Cambrian strata of the Hamill Group. The subtle, yet distinct angular unconformity that truncates the top of the Windermere Supergroup progressively deepens toward the east (Aitken 1969). This results in a strong preservational bias of deep-marine strata in western outcrops, versus the progressively more deeply eroded shallow marine strata to the east (Aitken 1969). Estimates suggest that 2-3 km of stratigraphy were eroded due to regional uplift associated with a latest Neoproterozoic to Cambrian rifting event that initiated the Western Canadian Sedimentary Basin (Ross and Hein 1989, Ross 1991, Ross et al. 1995).

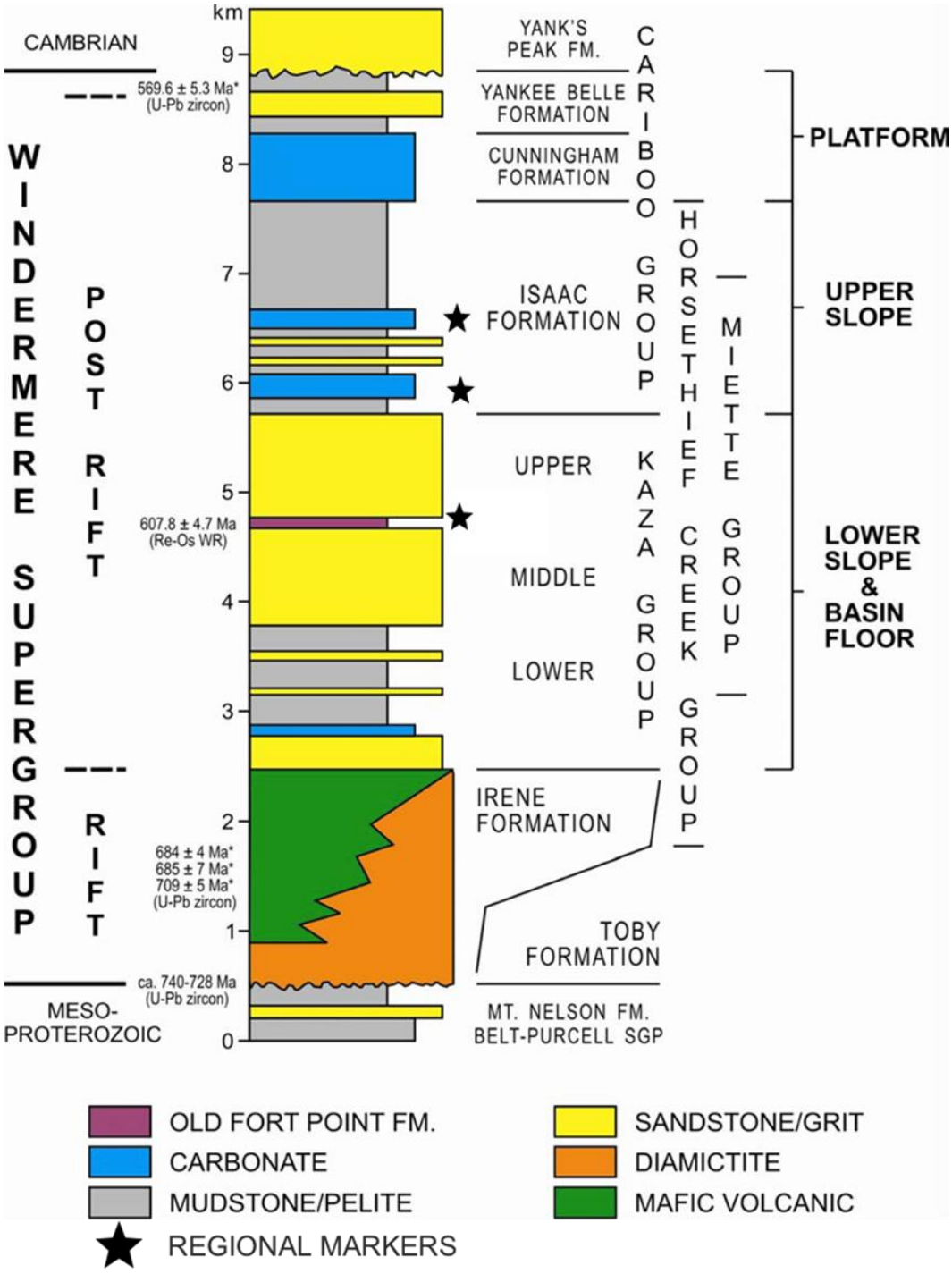

Figure 1-3 Generalized stratigraphic log of the Windermere Supergroup showing rift and post rift succession and interpreted paleogeographic locations. Geochronological dates from (Ross et al. 1995, Colpron et al. 2002, Lund et al. 2003, Kendall et al. 2004). Modified from Smith et al. 2014, redrawn from Ross and Arnott 2007).

1.4.6 Metamorphism and Structure

Due to the collision and accretion of allochthonous terranes during the middle Jurassic to early Tertiary the Windermere Supergroup has been deformed from its original miogeoclinal morphology to its present day structurally deformed geometry in the Canadian Cordillera (Monger et al. 1982). The Canadian Cordillera is made up of five distinct morphogeographic belts, which from east to west they are the Foreland Fold and Thrust Belt, Omineca Belt, Intermontane Belt, Coast Belt, and Insular Belt (Monger et al. 1982, Reid et al. 2002). The Castle Creek study area occurs within the Omineca Belt and has undergone four phases of structural deformation (D1, D2, D3, and D4) and two phases of low grade (greenschist facies) metamorphism (M1 and M2) (Murphy and Rees 1983, Murphy 1987a, 1987b). The first phase of deformation (D1) comprises tight to isoclinal, NW-trending metre-scale folds (

Figure 1-4). Concurrent with D1 is the first phase of metamorphism (M1) defined by a metamorphic mineral assemblage dominated by muscovite, chlorite, and biotite (Murphy 1987a). This deformation event is believed to have formed in response to the obduction of the first suspect terrane onto the western North American margin during the middle Jurassic (Murphy 1987a). The second deformation event (D2) represents the principal structural fabric in the Castle Creek study area, and includes centimetre-, metre-, and kilometere-scale, NW-trending, SW-verging folds and reverse faults (Murphy and Rees 1983, Murphy 1987a, Reid et al. 2002). The D2 event is believed to have initiated the second phase of second phase of low grade metamorphism (M2), as indicated by metamorphic mineral growth that overgrows D2 structures (Murphy 1987a). The third deformation event (D3) formed during the latter stages or postdated M2, producing dextral strike-slip faults and associated kilometer-scale folds (Reid et al. 2002).

The final deformation event (D4) produced NE trending, centimeter-scale kink bands and meter-scale kink folds (Murphy and Rees 1983, Murphy 1987a, Reid et al. 2002).

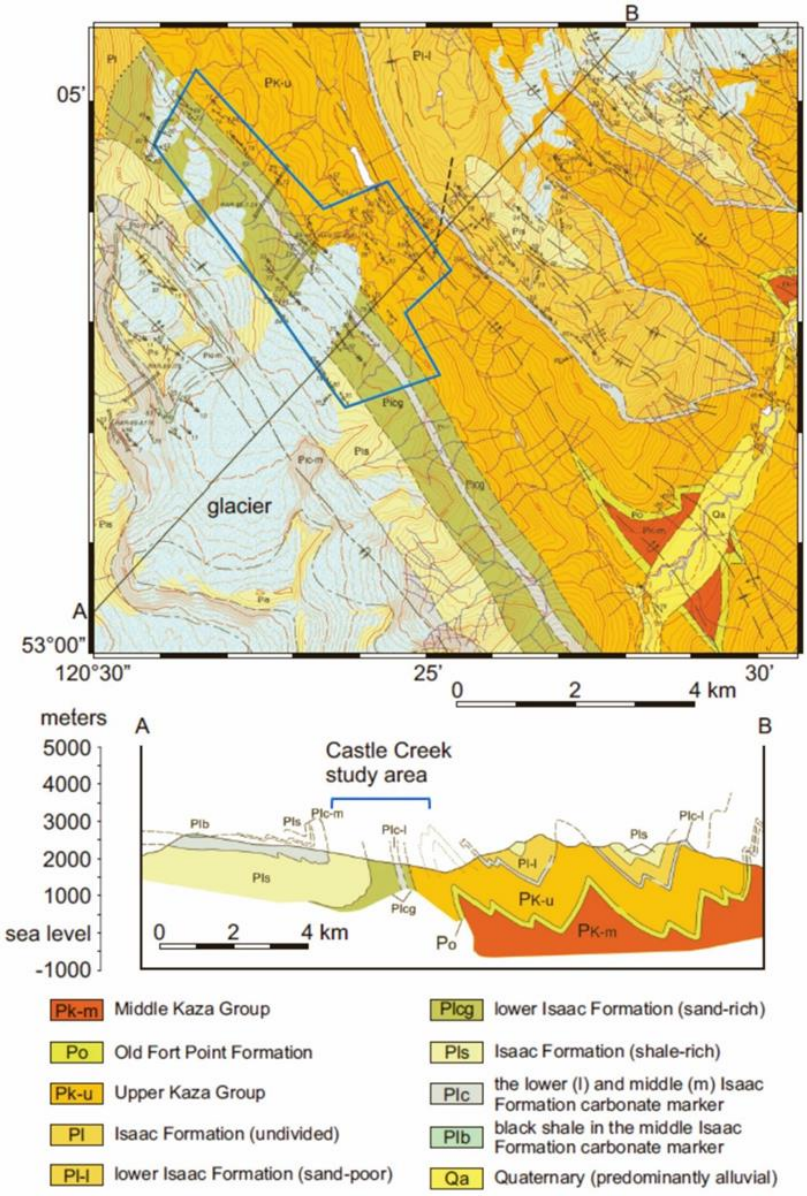

Figure 1-4 Regional geology of the Castle Creek study area **(outlined in blue)** (portion of the Eddy 1:50,000 map area of (Ross and Ferguson 2003a).

1.5 Methodology

Over the course of two field seasons from mid-July to late-August 2015 and 2016, a 270 m-wide (parallel to bedding) by 30 m-thick (perpendicular to bedding) section in base-of-slope strata of the Isaac Formation at the Castle Creek study area was measured on bed-by-bed scale (Figure 1-5). Eighteen stratigraphic logs were measured with thickness ranging from 10 m to 30 m and separated laterally by ~30 m to ~60 m depending on the quality of exposure (Figure 1-6). Additional, shorter stratigraphic logs (~ 2 m thickness) were located laterally ~5 m - 7 m apart to capture abrupt lateral transitions. Individual beds were correlated laterally by physically walking out their contacts while noting any lateral lithological changes.

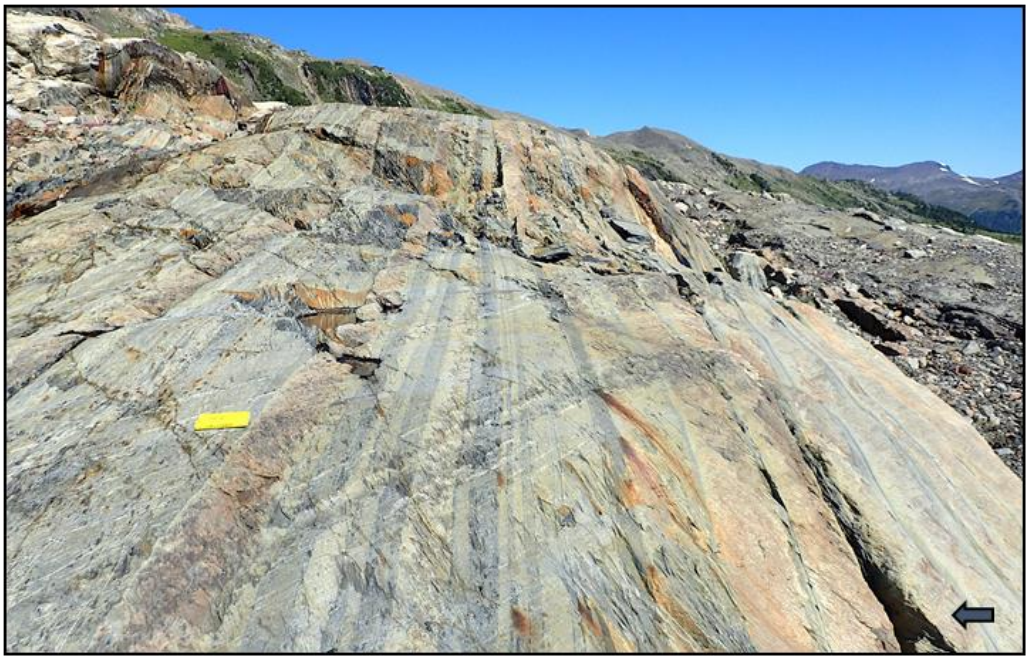

Figure 1-5 Depositional strike view (facing NW) of the study section in the Castle Creek study area. Note the easily traversed, glacially polished, vertically dipping strata of the Isaac Formation. Notebook for scale. Black arrow indicates stratigraphic up.

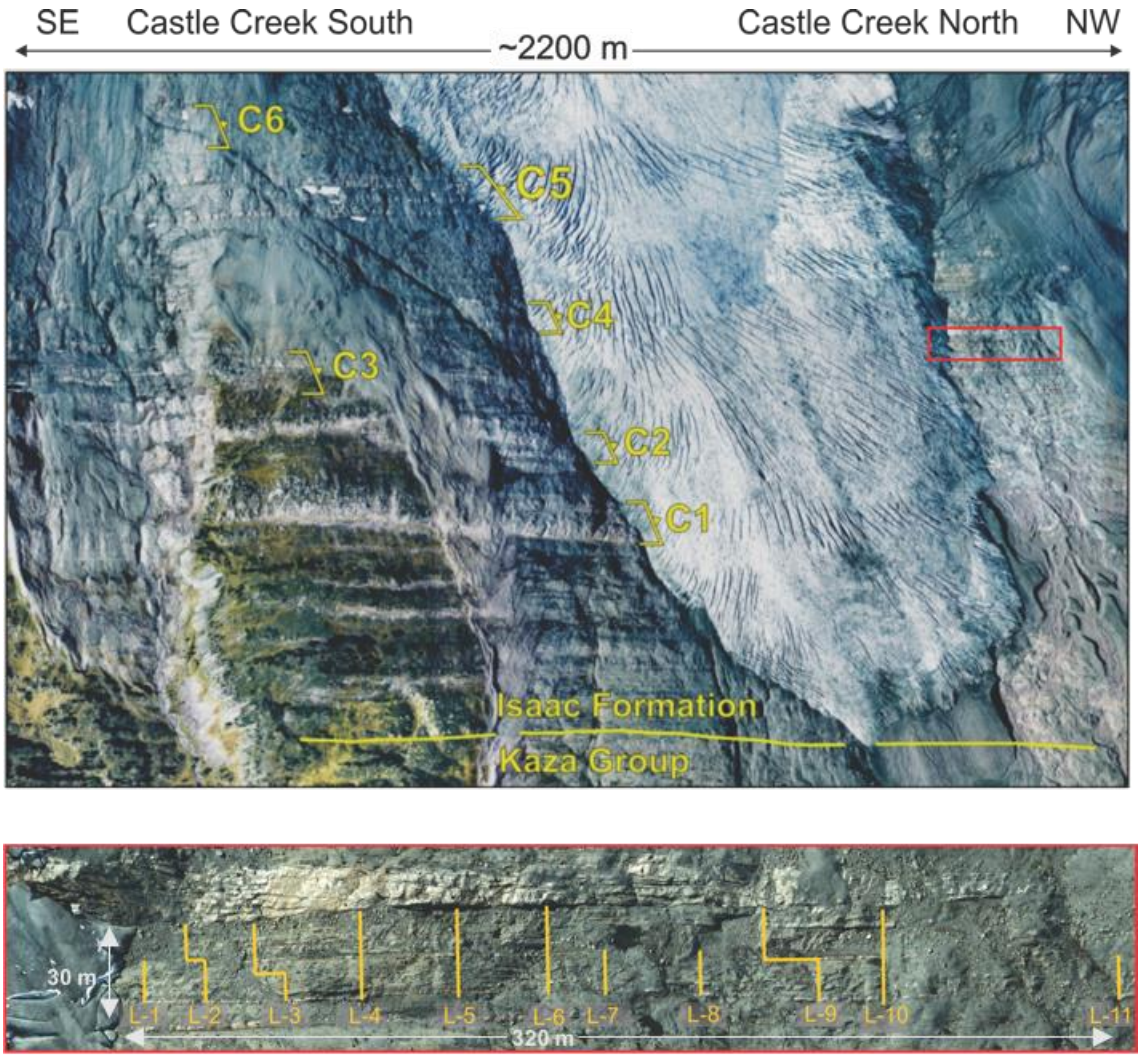

Figure 1-6 Location of measured stratigraphic logs **(in red)** in the study area. Logs are approximately ~30 m apart. Individual beds were walked out and any changes in lithology or texture noted and recorded.

Standard sedimentary descriptions were made of each bed, including bed thickness, basal contact morphology, colour, grain size, grain sorting, primary and secondary sedimentary structures, visual estimates of matrix content, and occurrence of mudstone intraclasts. In the field, grain size measurements were recorded using a Wentworth grain size card with a 16X magnification hand lens. Bed thickness was measured using a standard measuring tape and

photographs of every bed were taken. These data were used to create correlation panels that captured the lateral and vertical distribution and transition of beds within the measured section.

In the field, matrix-rich sandstones are easily recognized by their distinctive blue-green hue, which is a reflection of elevated matrix content, specifically higher chlorite content. Hand samples were collected in the field and later cut into thin sections for microfacies analysis (i.e. grain size, grain sorting, texture, and mineralogy), and especially for estimating matrix content. With the use of a mechanical stage, thin sections were manually point counted using a standard systematic grid technique. Thin sections were point counted with a stepping interval of 1.1 mm, ensuring approximately 300 points were collected from each thin section. The following equation adapted from Popović (2016)was used to categorize the composition of each thin section:

Total = Framework Grains + Matrix + Altered Grains + Cement

$$\text{Total} = (Q_S + F_S + L_S + O_S) + (M_S + M_{RXC}) + (RXC_B + RXC_{SG}) + (C_{C+CM}),$$

where Q_S is quartz grains of sand size or coarser; F_S is feldspar grains of sand size or coarser; L_S are lithic sand grains or coarser; O_S are other minerals (typically pyrite); M_S is grains of silt and finer; M_{RXC} is recrystallized matrix (composed of muscovite and chlorite, regardless of crystal size). RXC_B is recrystallized medium sand-sized quartz grains or coarser with distinct grain-boundary migration. RXC_{SG} is recrystallized fine grained quartz subgrains with visible subgrain rotation or bulging recrystallization. C_{C+CM} is carbonate cement.

Due to low grade metamorphism primary clay matrix has been recrystallized to muscovite and chlorite. Therefore, in this study muscovite and chlorite, regardless of crystal size

or habit, is considered matrix. However, due to the alteration of primary detrital matrix, the contribution of authigenic matrix is difficult to discern. Still, relative to matrix-poor sandstones, matrix-rich sandstones are not depleted in feldspar, making the contribution of matrix from diagenetically altered feldspars negligible. Furthermore, the dramatic lateral changes in matrix content from within individual beds (see discussion in Chapter 4) occurs over significantly shorter distances compared to those associated with diagenetic processes (Wilson and Pittman 1977). The abrupt lateral change in matrix content from a single bed, is interpreted to be a consequence of transport processes rather than the diagenetic alteration of detrital framework grains.

Moreover, sand-rich rocks at Castle Creek have undergone dynamic quartz recrystallization. At lower greenschist facies conditions, specifically 250°C to 500°C with low strain rates, quartz grain boundaries may exhibit bulging recrystallization, and subgrain rotation recrystallization. Under these conditions, grain boundaries may separate from older grains, forming new sub-grains (Stipp et al. 2002). Therefore, for this study, all sub-grains, regardless of crystal size, are considered alerted framework grains. Sub-grains, specifically grains that underwent sub-grain rotation, were identified as having linear grain boundaries, straight extinction, and typically concentrate along grain boundaries (Stipp et al. 2002).

During (thin section) point counting porosity was not considered a component. Previous workers, for example Reedy et al. (1996), Aniekwena et al. (2003), and Amy et al. (2009), have reported primary intergranular porosity in mud-poor sandstones to be of the order of 0.3-0.35 but less than 0.05 in matrix-rich sandstones. Additionally, rocks in the study area have been metamorphosed to lower greenschist facies and tectonized (deformed and compacted). Accordingly, porosity in matrix–poor, but more profoundly matrix-rich sandstones, is expected

to be negligible. As a consequence, not including porosity in the point counting procedure most likely had little effect on the estimation of component abundance.

1.6 Previous Work

This study is one of several that have described matrix-rich sandstones in the Windermere Supergroup (Leclair and Arnott 2003, Arnott, R, W 2007, Davis 2011, Rocheleau 2012, Terlaky 2014, Angus 2016, Popović 2016). However, the first comprehensive study wasn't undertaken until Terlaky and Arnott (2014) described matrix-rich sandstones from the Upper and Middle Kaza groups. In that study, Terlaky and Arnott (2014) observed matrix-rich strata undergoing a lateral facies transition from matrix-poor (20 to 30% matrix) to matrix-rich sandstone (30 to 50%), and then to thin-bedded turbidites. Matrix-rich strata were also correlated laterally to scoured based sandstones and also shown to be commonly overlain by matrix-poor architectural elements (i.e. distributary channels and splays). Furthermore, Terlaky and Arnott (2014) reported that matrix-rich sandstone facies occur in a variety of paleogeographic settings, specifically the Isaac Formation (base of slope setting), Upper Kaza Group (proximal basin floor), and Middle Kaza Group (medial basin-floor setting). These authors interpreted these strata and their distinctive lateral changes in lithofacies to be a consequence of the voluminous introduction of fine-grained sediment into throughgoing sand-rich turbidity currents due to a local upflow avulsion. On the margins of the avulsed high-energy jet flow particle settling resulted in deposition of matrix-poor followed by matrix-rich sandstones and finally thin bedded turbidites (Figure 1-7). Moreover, the occurrence of matrix-rich sandstones in a variety of paleogeographic settings, including base-of-slope (Isaac Formation), proximal basin floor (Upper

Kaza Group) and medial basin floor (Middle Kaza Group) suggested that deposition of matrix-rich sandstones was not paleogegraphically-specific, but instead dictated by local sedimentological conditions, including the availability and incorporation of mud, which quite possibly was related to flow avulsion.

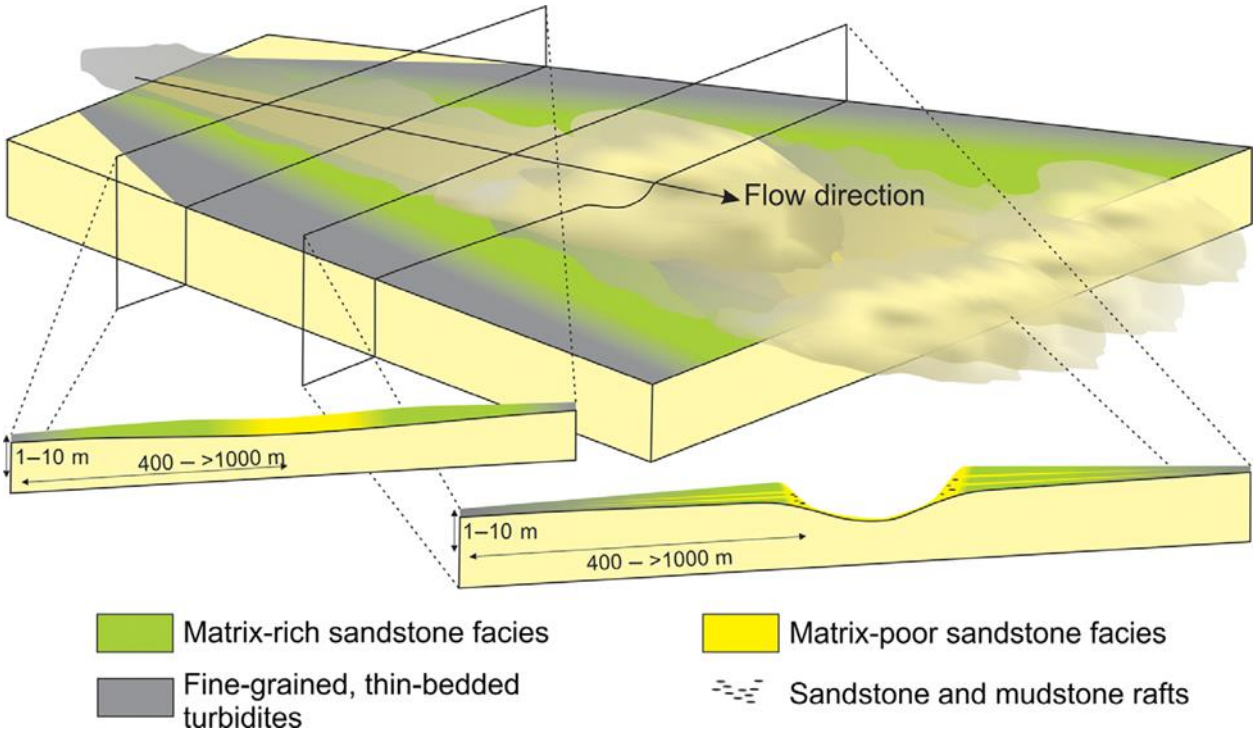

Figure 1-7 Origin of matrix-rich sandstones from Terlaky and Arnott (2014). Following avulsion, flows scour the mud-rich seafloor and charge the through-going turbidity currents with fine sediment. Beyond the avulsion node, and along the margins of the jet flow, matrix-poor sandstones are deposited, which further laterally transition to matrix-rich strata, and ultimately thin-bedded, fine grained turbidites.

Popović (2016) provided further insight into the lateral depositional continuum of matrix-rich sandstone deposits by conducting a detailed micro- and macro-facies analysis in the Upper Kaza Group. Popović (2016) observed a lateral succession of facies from matrix-poor sandstones (<14% matrix), to amalgamated sandstones to better stratified intermediate clayey sandstones

(25-40%), to sandy claystones (>50-70% matrix) and then, finally, to either fined grained banded couplets or thin-bedded upper division turbidites. This succession of facies and their systematic spatial distribution was interpreted to represent a depositional continuum downflow and lateral to an avulsion node. Locally avulsed flows would have deeply scoured the mud-rich seabed and charged flows with fine grained sediment, which then became partitioned towards the margins of the flow. The lateral facies change occurs towards the margins of the flow where clayey sandstone with intermediate matrix content changed into sandy claystone and then to either fine-grained banded couplets or thin-bedded, upper division turbidites.

Popović (2016) also conducted detailed petrographic analysis of matrix-rich sandstones and observed that the development of ductile deformational microstructures was an effective way to estimate the amount of primary detrital clay mineral matrix. Specifically, in matrix-poor sandstones (matrix content <15%) deformational microstructures, such as recrystallized quartz grains with prevalent bulging and sub grain rotation, were well developed; whereas in sandstones with moderate (15-20%) or greater matrix content these features were generally absent, suggesting that even moderate matrix content can effectively dissipate imposed tectonic strain (Figure 1-8).

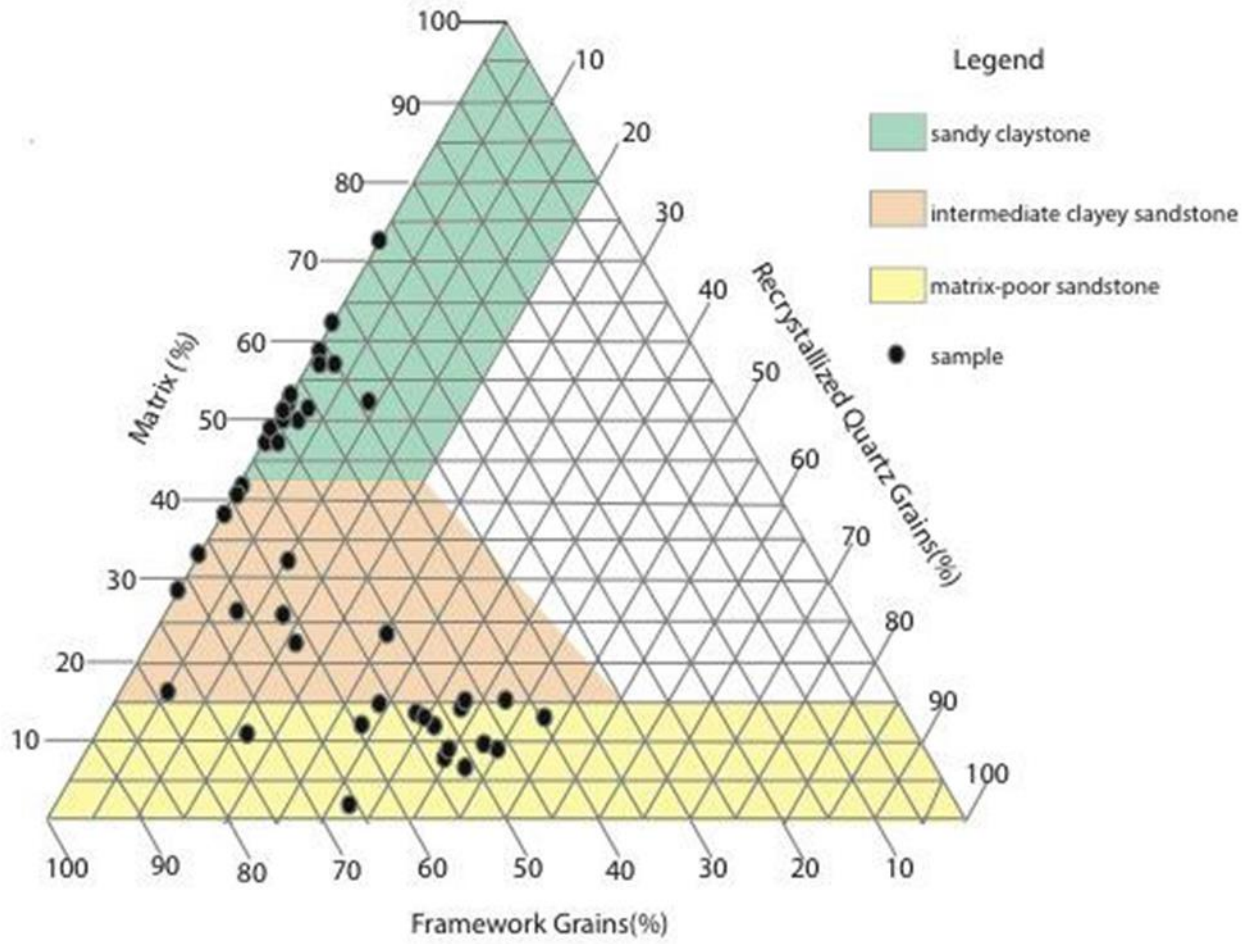

Figure 1-8 Composition of 42 petrographic samples collected from the Kaza Group. Coloured areas were based on the ratio of matrix to recrystallized grain. Importantly, the presence of detrital matrix favours mechanical grain rotation and dissolution-precipitation mechanisms in quartz grains resulting in an inverse relationship between matrix and recrystallized grains (white area) (from Popović, 2016).

Angus (2016) further described the lateral depositional continuum of matrix-rich sandstones in both the Upper Kaza Group and Isaac Formation. Along a single bed Angus (2016) identified a rapid lateral facies change from clayey sandstone (10-30% matrix) to a bed consisting of two parts, a basal clayey sandstone (10-45% matrix) separated by a sharp, planar interface and overlain by an upper sandy-claystone (20-65% matrix), collectively referred to as a

bipartite bed. Laterally, the basal sandy claystone part of the bed progressively thinned whereas the upper clayey sandstone part initially thickened and then remained of more or less constant thickness thereafter. Further laterally the basal unit pinched out and the bed consisted entirely of the sandy claystone, which continued to thin and then pinch out. Overall the entire transect is overlain by a matrix clean, thin-bedded turbidite that extends beyond the pinch out of the clayey-sandstone.

Angus (2016) interpreted the lateral continuum to be the result of a flow whose rapidly evolving structure was controlled by particle settling along the margins of an avulsed jet flow (Figure 1-9). Settling of coarse particles displaced fluid and finer particles (silt, clay and low density mud clasts) upward into the upper part of the suspension. Further down-current; the more sand-rich basal part of the flow thinned and eventually pinched out as the reservoir of settling sand grains became depleted and the upper, matrix-rich part eventually formed the entire suspension. Owing to the abundance of fine sediment and low rates of shear, particle-particle interaction caused the suspension to develop shear strength and rapidly evolve toward a plug flow condition with the resulting deposition of a sandy claystone. Finally, the entire detached plume of sediment was overlain by a low concentration plume that reworked the top of all previously deposited sediment and deposited a very thin- to thin bedded turbidite.

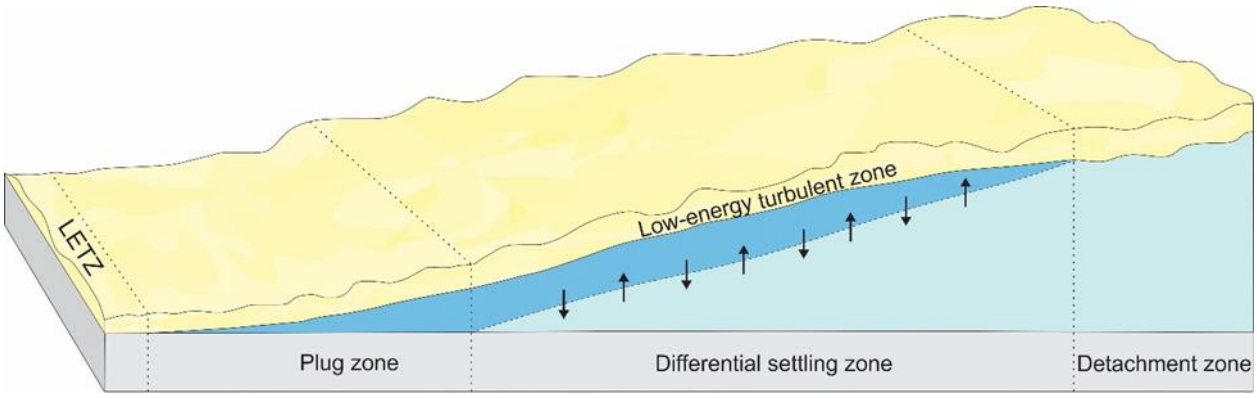

Figure 1-9 Schematic of the depositional continuum (from Angus, 2016), which from right (proximal) to left (distal), consists of clayey sandstone deposited in the detachment zone that then changes to bipartite beds within the differential settling zone, sandy claystone beds within the plug zone, and finally matrix-poor structured units in the low-energy turbulent zone **(LETZ)**. The dashed line in the differential settling zone separates a basal layer of mostly coarse grains **(light blue)** from an upper layer of mostly fine grains with dispersed coarse grains **(dark blue)**. Arrows indicate differential movement of particles within the suspension where finer grains are preferentially displaced upward as coarser grains settle (Angus 2016).

2 Deep-Water Sediment Transport Processes

Observations in lakes, fjords, and flumes as well as historical occurrences, such as the 1929 Grand Banks event (Heezen and Ewing 1952), have helped establish that sediment is primarily transported into the deep sea by sediment-gravity flows (Normark and Piper 1991). However, measuring in-situ flow behavior of sediment-gravity flows in nature has proven challenging, primarily due to their infrequent occurrence, inaccessibility, and destructive nature. Therefore, much of the current understanding of deep-water sediment transport processes has been inferred from observations of ancient deep-water gravity flow deposits that are exposed in outcrop. Yet, due to the various qualifications and terminology used by numerous authors, classification of gravity flows can be unclear and controversial (Mulder and Alexander 2001).

Since the publication of Mulder and Alexander (2001), there has been a steady increase in the recognition and study of sandstones rich in detrital mud. Novel experimental and outcrop work has been conducted to further investigate flows that are rich in mud and sand, as well as their resulting deposits, which are thought to be transitional in both nature of the flow and character of the deposit. Therefore, a general review of deep-water sedimentary processes, in addition to recent work related to transitional flows, are discussed next.

2.1 Density Flows

Density flows are a consequence of a density difference between two fluid media and gravity. In the deep sea the most common kind of density current involved in sediment transport and deposition are sediment-gravity flows. In these flows the denser medium, which constitutes the flow, is the result of a local dispersion of suspended sediment. Initiation of sediment-gravity flows can be the result of several factors such as slope failure caused by oversteepening, seismic loading, cyclic storm-wave loading, and others listed by Piper and Normark (2009). In the deep ocean density flows are generally sub-divided into two end member kinds, mass movements and sediment-gravity flows (Shanmugam 1996).

2.2 Mass Movements

Mass movements occur due to slope failure and move down a gravitational gradient. Detachment and downslope displacement of coherent to semi-coherent blocks of previously deposited sediment takes place along basal glide planes, with blocks commonly retaining much of their pre-movement internal stratigraphy (Shanmugam 2006). Slides and slumps are the two primary subsets of mass-movements and are generally differentiated by the shape of the glide planes and the nature of internal deformation. Slides generally have a planar glide plane and internal deformation is mostly brittle in nature. Slumps, on the other hand, typically have a concave-up glide plane and undergo rotational movements causing more ductile internal deformation (Shanmugam 2006, Arnott 2010).

2.3 Sediment-Gravity Flows

Sediment-gravity flows are produced when a sediment-laden suspension flows into and displaces a less dense ambient fluid. This thesis follows a simplified version of Mulder and Alexander's (2001) classification scheme (Figure 2-1), which differentiates sediment-gravity flows based primarily on flow rheology: cohesive flows and frictional flows, while further subdividing frictional flows on the basis of the dominant sediment support mechanism; namely, hyperconcentrated density flows, concentrated density flows and turbidity currents (Mulder and Alexander 2001).

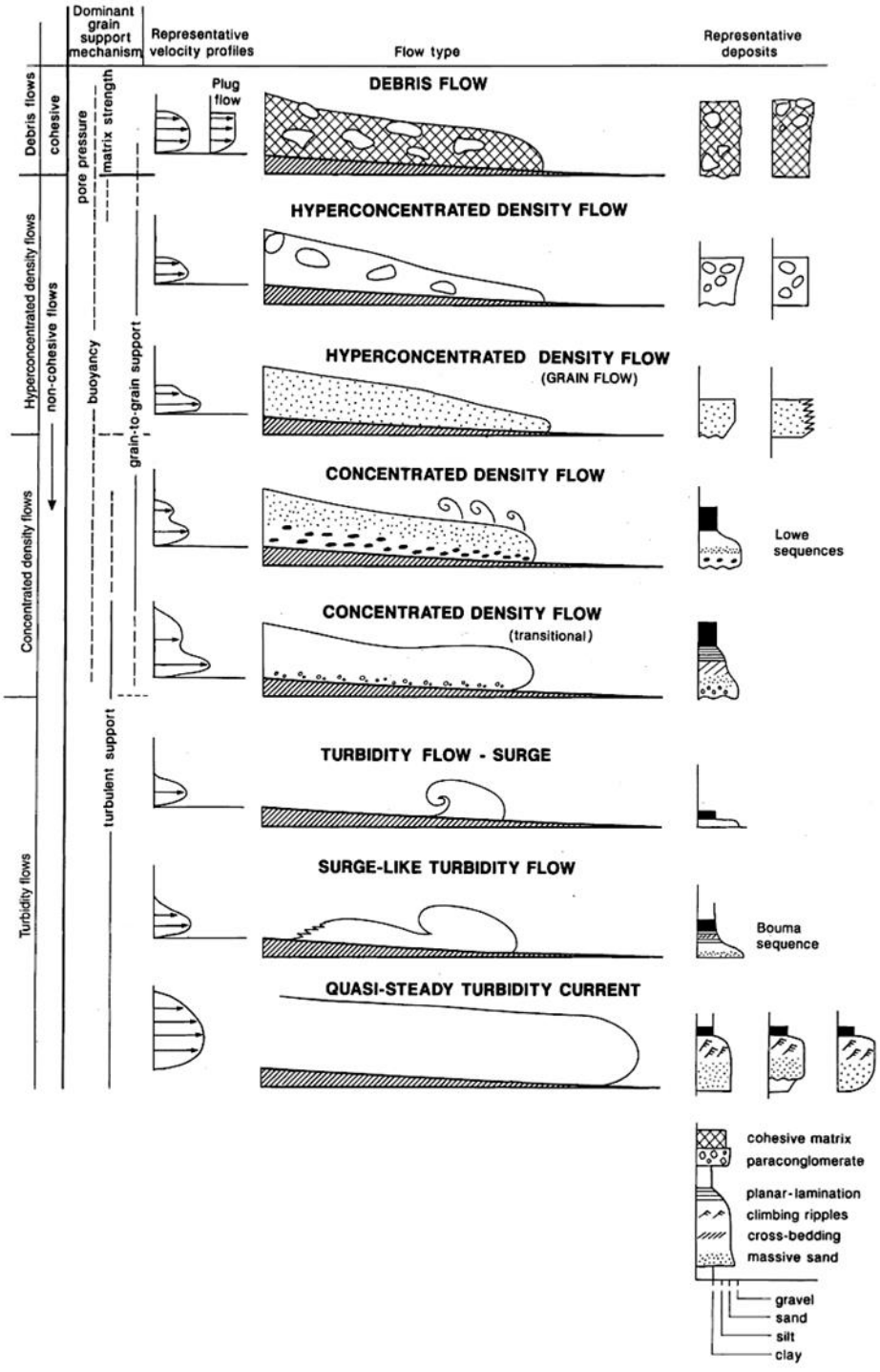

Figure 2-1 Classification of subaqueous density currents with dominate grain support mechanisms and idealized velocity profiles, current shape and stratigraphic logs (from Mulder and Alexander 2001)

2.3.1 Cohesive Flows

Cohesive flows are those that contain sufficient fine cohesive sediment as to impart a pseudoplastic rheology to the sediment-fluid mass. Mud, specifically clay size clay mineral particles, are the principal cohesive material in submarine environments, which due to weak Van der Waals forces between adjacent particles form a network structure that increases kinematic viscosity (Perret et al. 1995). Thus, cohesive particles impart matrix strength, the principal sediment support mechanism for cohesive flows, although, buoyancy, elevated pore pressure and dispersive pressure may also be important (Mulder and Alexander 2001). Deposition of cohesive flows occurs *en masse* from the top down, when internal shear resistance from cohesion equals or exceeds the force of gravity.

Debris flows are the principal type submarine cohesive flow (Mulder and Alexander 2001). Debris flows consist of poorly-sorted sediment (>5% gravel with variable sand proportion) and may transport boulder-sized clasts. Debris flow deposits, or debrites, commonly consist of a massive, structureless, poorly-sorted assortment of particles that even in the same bed can range from clay up to boulders (Mulder and Alexander 2001).

2.3.2 Frictional Flows

Unlike cohesive flows, frictional flows are made up of independently supported particles, and thus exhibit no yield strength. Therefore, once a shear stress is applied the fluid will immediately deform, therefore behaving like a Newtonian fluid (Shanmugam 2006). The proportion of cohesive and non-cohesive particles that define the threshold between cohesive and frictional flows in not well known and is thought to vary depending on flow conditions and

sediment concentration (Fisher 1971, Iverson 1997). Frictional flows are further divided into three categories: turbidity currents, concentrated density flows, and hyperconcentrated density flows (Mulder and Alexander 2001).

Turbidity currents are thought to have a sediment concentration below 9% sediment volume concentration, otherwise known as the Bagnold limit. Under these conditions particles are sufficiently spaced that particle-particle collisions are insufficiently frequent to provide full particle support, which instead is provided by the upward component of fluid turbulence (Mulder and Alexander 2001). Deposition occurs when competence is exceeded (the ability of the flow to transport a particular grain size), which principally is controlled by particle fall velocity. Deposits of turbidity currents, or turbidites, were first described in detail by Arnold Bouma (1962), who reported a consistent vertical assemblage of depositional characteristics that formed an overall upward-fining succession. Stratigraphically upward an ideal Bouma turbidite sequence consists of normally graded or massive sandstone (Ta), planar-stratified sandstone (Tb), ripple-cross stratified sandstone (Tc), diffusely laminated siltstone to mudstone (Td), and structureless mudstone (Te) (Figure 2-2).

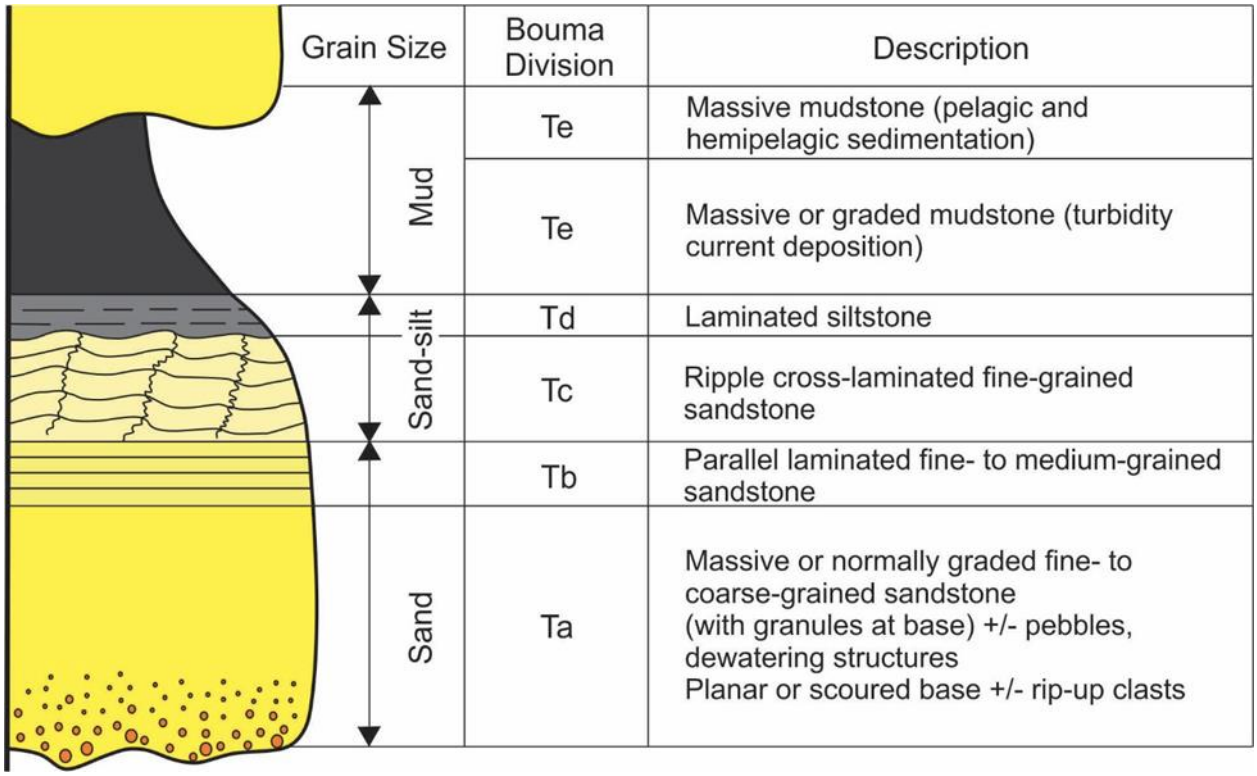

Figure 2-2 Idealized five division Bouma turbidite model showing a progressive upward change in grain size and sedimentary structures (after Bouma 1962, from Angus 2016).

Concentrated density flows contain 9-25% sediment by volume (Mulder and Alexander 2001). Under these conditions, dispersive pressure (grains suspended by particle-particle interactions), and hindered settling (grain settling inhibited by shear generated by the upward displaced fluid) are the dominant sediment support mechanisms. However, at sufficiently low sediment concentrations the upward component of fluid turbulence partly supports particles in suspension (Mulder and Alexander 2001). Concentrated density flow deposits consist of a crudely normally graded or massive sand (equivalent to a Bouma Ta or the S3/R3 division of Lowe (1982)), in addition to inversely graded (R2), massive and normally graded (R3) gravel deposits.

Hyperconcentrated density flows contain >25% sediment by volume, with <2% mud content, and have similar grain-to-fluid proportions as cohesive flows. Under these conditions, hyperconcentrated flows behave as a non-Newtonian fluid, but due to the lack of cohesive sediment do not exhibit matrix strength. Therefore, dispersive pressure (i.e. grain-grain interactions) is the predominant sediment support mechanism (Mulder and Alexander 2001). Deposition of hyperconcentrated density flows occurs due to frictional freezing and results in deposits that consist of massive sand with common dish structures, fluid escape structures and large clasts. However, subtle inverse grading may also develop locally (Mulder and Alexander 2001)

2.4 Transitional Flows

As sediment-gravity flows move they may progressively entrain fluid and/or erode sediment from the seafloor, resulting in variable concentrations of cohesive and non-cohesive material. As a result, a single current's flow behavior may evolve spatially and temporally depending on sediment concentration, flow speed, and concentration of cohesive particles (Mulder and Alexander 2001). Flows that exhibit intermediate and/or hybrid flow behaviour are termed transitional flows, and in the past decade have been increasingly interpreted to be responsible for the deposition of a variety of sand-rich strata containing abundant admixed mud.

2.4.1 Slurry Flows

Slurry flows, first described by Lowe and Guy (2000), consist of seven divisions (M1-7) (Figure 2-3). The M1 division is a current-structured and/or massive sandstone. The M2 division comprises distinctive alternating cm- to m-thick, light (mud-poor) and dark (mud-rich) bands, whereas mm to cm scale wavy laminations make up the M3 division. The M4 division is a mud poor sandstone unit that contains ubiquitous dewatering structures, while the M5 divisions are characterized by cyclic microbands and flat laminations. The M6 divisions is a foundered and mixed sandstone/mudstone, and the M7 division is a well-developed water escaped unit (Lowe and Guy 2000).

Slurry flows are interpreted to have initially been fully turbulent, mud-rich turbidity currents. The lowermost M1 layer would be analogous to the deposit of a high-density turbidity current (Lowe and Guy 2000). However as the turbidity current wanes, particles begin to settle and the flow begins to become stratified as sand and coarser particles, but more importantly, mud (silt and clay) begin to progressively accumulate in the near-bed region. Sand and coarser quartz and feldspar particles settle to the bed and form a light band in the M2 division. However mud concentration is steadily increasing, and eventually creates a sufficiently viscous near-bed mud layer that it cohesively freezes, producing the mud-rich dark bands and laminae in the M2 and M3 divisions, respectively (Lowe and Guy 2000). M4 divisions are interpreted to have formed in mud poor flows where high sediment fallout rates and direct suspension sedimentation formed dish-structured units. Eventual settling of the finest sand-sized particles resulted in the deposition of the M5 division, which may be analogous to the Tbde sequence in turbidites. Finally, M6 and

M7 divisions are inferred to have formed by post-depositional water escape, foundering and shearing (Lowe and Guy 2000).

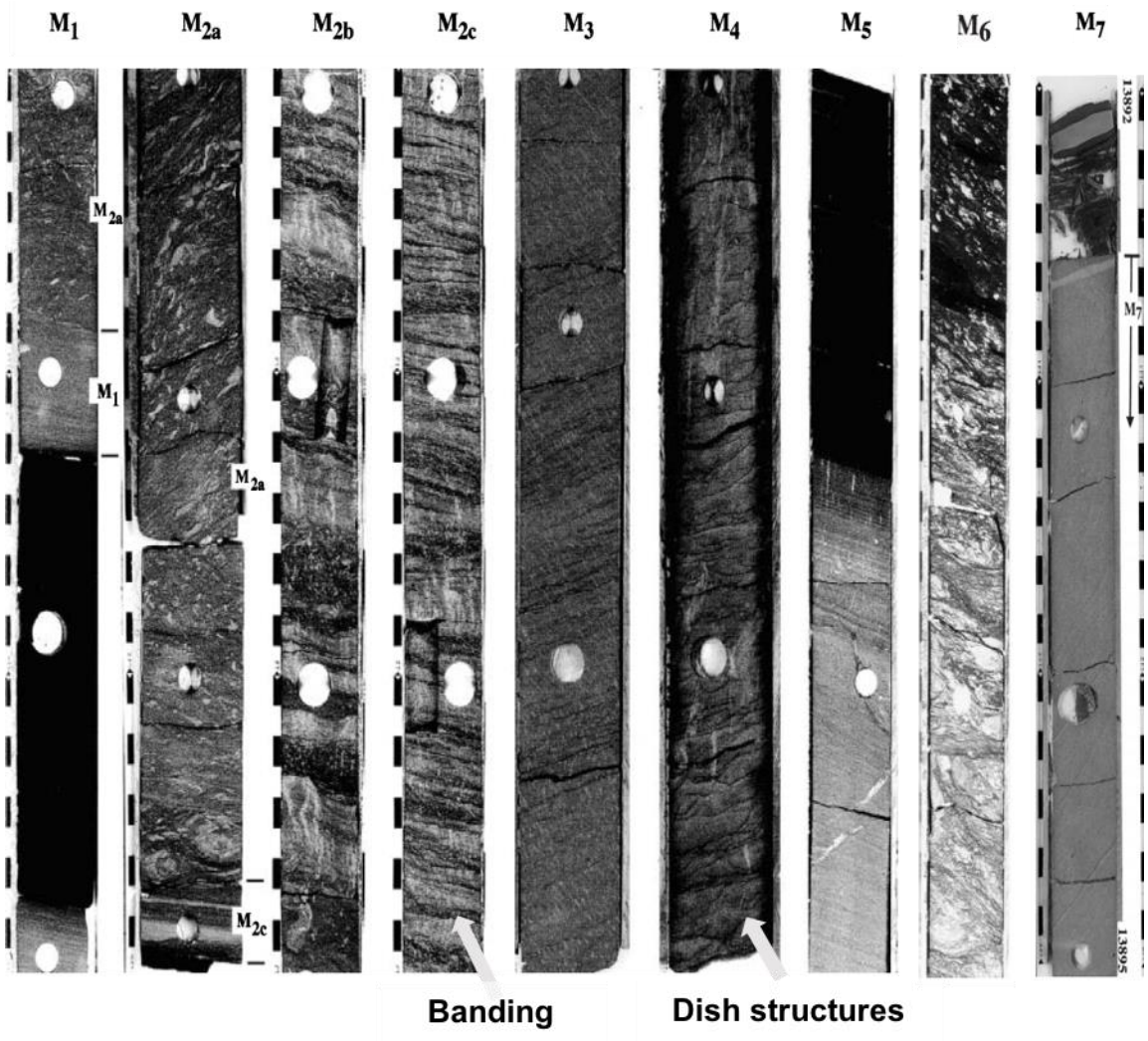

Figure 2-3 The M1- M7 divisions of slurry flow beds (modified after Lowe and Guy (2000); Lowe et al. (2003).

2.4.2 Hybrid Event Beds

Hybrid event beds as described by Haughton et al. (2003, 2009) and Talling et al. (2004), consist of five divisions (H1-5) (Figure 2-4). The basal most division (H1) consists of a sharp planar based, mud-poor, graded to ungraded, structureless, dewatered sand overlain by alternating bands of mud-poor and mud-rich sand (H2). This, is irregularly overlain by a muddy sand with mud clasts, sand patches, sand injections, outsized granules and shear fabrics (H3). The succession is capped by a thin, plane-parallel laminated and/or ripple cross-laminated sand (H4), which may contain pseudonodules, overlain by massive mud (H5) (Haughton et al. 2009).

Several mechanisms have been proposed for the development of hybrid event beds. Haughton et al. (2009) interpreted the vertical arrangement of divisions to be the result of a single flow that underwent a longitudinal transformation, where the basal clean sand layer (H1) was deposited by a turbidity current, followed by alternating laminar and turbulent flow behavior in the tail of the turbidity current (H2). The H3 division was inferred to be deposited by a genetically linked debris flow, and the H4 and H5 divisions being the result of reworking and deposition of a low density turbidity current (Haughton et al. 2009).

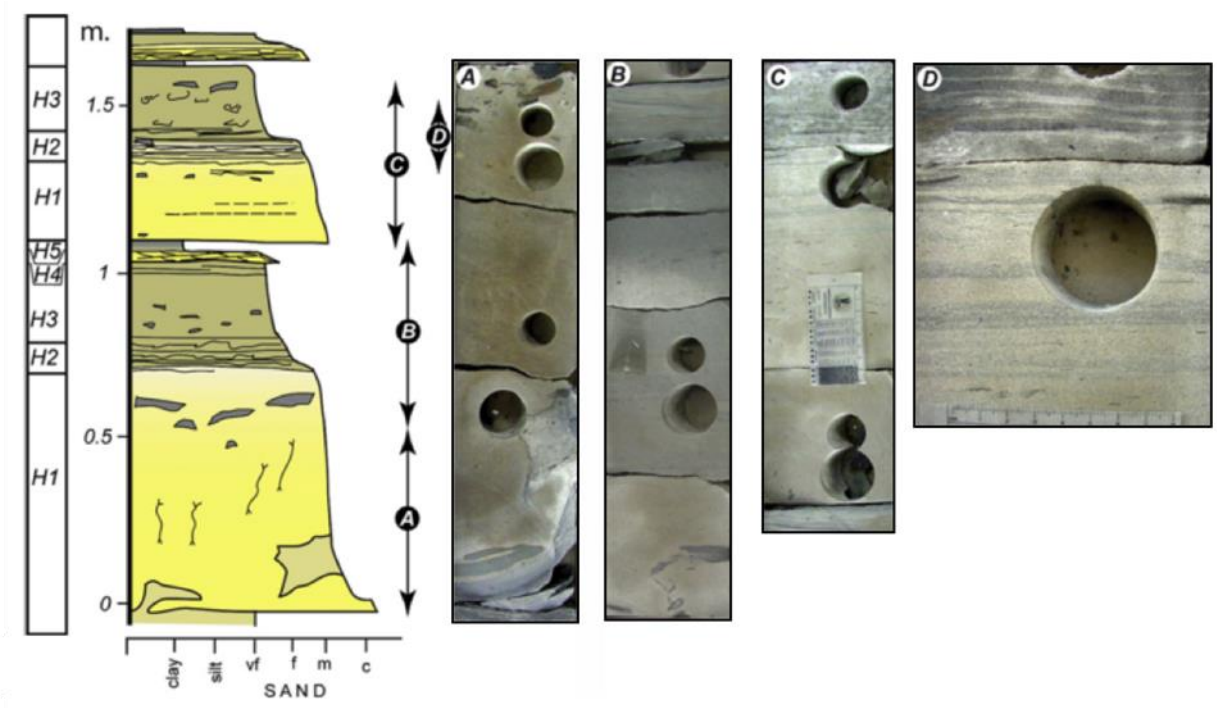

Figure 2-4 Schematic of two stacked hybrid event beds from the Forties Sandstone, Everest Field, central North Sea. Each labelled arrow refers to the corresponding photo on the right. Note the lower bed **(arrows A and B)** contains all five divisions (H1–H5) but H4 and H5 are absent in the upper bed. Both beds contain a banded H2 division sandwiched between H1 (clean sandstone) and H3 muddy sandstone (see **B**). Note the banding (see upper part of **D**) of crudely segregated cm-scale lighter and darker intervals (from Haughton et. al 2009).

2.4.3 Experimental Transitional Flows

Experimental work by Baas et. al (2002, 2009, 2011) investigated both exclusively clay-laden flows, as well as variable non-cohesive sediment-clay mixtures. These authors reported that flows with up to ~ 2% kaolinite were fully turbulent (TF) and exhibited a logarithmic velocity profile away from the bed. In addition, fluid turbulence was sufficiently strong and prevented clay particles from bonding and forming a particle network. However, with

progressively higher clay concentration, (2-4% kaolinite), three types of transitional flows were recognized: 1) turbulence-enhanced transitional flow (TETF); 2) lower transitional plug flow (LTPF); and 3) upper transitional plug flow (UTPF). Turbulence-enhanced flows were characterized by enhanced turbulence intensity, inferred to be sourced from an internal shear layer located at the near-bed region (Baas and Best 2002, Baas et al. 2011). In lower transitional plug flows, a turbulent basal region with a saw-tooth velocity profile was overlain by a laminar plug-like region where turbulence was absent and shear minimal. As clay concentration increased further flows transformed into upper transitional plug flows with a much thinned upper plug-flow region and reduced near-bed turbulence intensity. As clay concentrations surpassed 4%, the overlying laminar plug like flow expanded even further until it became the full thickness of the flow. Under these conditions, the clay particles formed a pervasive gel that suppressed turbulence. This quasi-laminar plug flow (QLPF) is characterized by a viscous rigid plug, in which turbulence and internal deformation were absent (Baas and Best 2002, Baas et al. 2011).

Sumner et al. (2009) extended the work of Bass and Best (2002), with the objective of studying the resulting deposits of transitional flows (Figure 2-5). Using a fixed sand concentration (10%) with varying amounts of mud, Sumner et al. (2009) identified four deposit types. Flows that had the lowest clay concentration (<6%) exhibited a traction-structured sand overlain by mud cap (deposit type I) or a structureless sand overlain by a mud cap (deposit type II). With intermediate mud content (11.25%-14.25%) a structureless sand overlain by an ungraded muddy sand with a mud cap (deposit type III) was deposited. At the highest mud concentrations (>14.25%) an ungraded muddy sand deposit with a mud cap formed (deposit type IV).

Sumner et al. (2009) correlated these deposits with the experimental flow types of Bass and Best (2002) (Figure 2-5). Specifically, Sumner et al. (2009) correlated deposit types I and II to the turbulent or either turbulence enhanced regimes. Under these conditions sand gradually settled from the turbulent flow as it waned, which if more rapidly decelerated, deposited a structureless bed. Type III deposits correlate with flows that are in the transitional plug regimes. Under these conditions, sand particles in the lower turbulent region settle as the flow wanes and turbulence decreases. However, as the flow slows the overlying laminar plug thickens, trapping sand. Finally, type IV deposits correlate with quasi-laminar plug flows when the laminar plug extends to the base of the flow and has sufficient yield strength to prevent particle settling (Sumner et al. 2009).

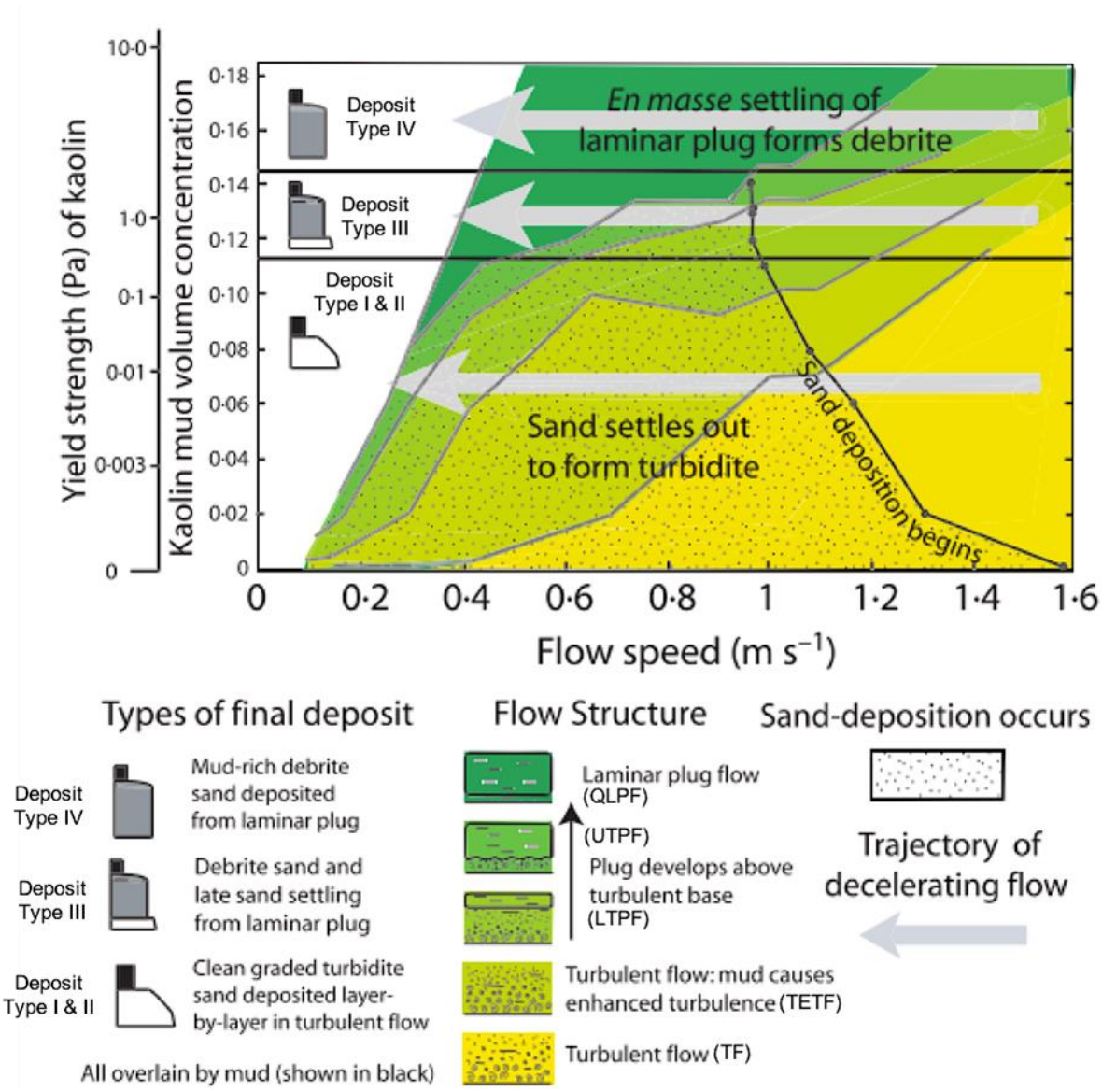

Figure 2-5 Phase diagram showing the relationship between flow speed, volume concentration of mud, vertical flow structure and resultant deposit (modified from Talling et al. (2012), after Sumner et al. (2009)).

2.5 Comparison of Transitional Flow Deposits and Matrix-Rich Sandstones

Matrix-rich sandstones in the Windermere Supergroup share comparable, yet disparate features with the previously discussed transitional flows. Like linked debrites, hybrid event beds, and transitional flow deposits, matrix-rich sandstones may also comprise two parts that form a single bed (e.g, sub-facies 4 of Terlaky and Arnott (2014), bipartite beds of Angus (2016), and bipartite beds of this study). In these beds the basal sandstone may contain up to 50% matrix, which then is sharply overlain by a planar based matrix-rich sandstone with 50-70% matrix. This two-part bed motif is similar to other transitional flow deposits, but lacks pervasive dewatering structures in the basal sandstone, and an undulatory or irregular surface separating the two parts of the bed. Moreover, matrix content in the basal sand-rich part is much greater than that in the basal part of transitional flow deposits (i.e. generally less than about 20% matrix) (Terlaky and Arnott 2014). Furthermore, matrix sandstones are generally thinner (cm-dm thick) and can contain up to 70% matrix (Terlaky and Arnott 2014, Popović 2016, Angus 2016), whereas transitional flow deposits are typically metres thick. Additionally, several (5-20) matrix-rich sandstones, will commonly stack to form meter thick assemblages that lack matrix-poor sandstone interbeds. These differences may suggest that matrix-rich sandstones in the Windermere Supergroup are potentially deposited from a quite different category of mixed sand and mud-rich turbidity currents, and thus warrant additional research.

3 Facies Descriptions

Using detailed field observations and thin section analysis, four facies and two sub-facies have been identified. A summary of their descriptions and interpreted depositional mechanisms are listed in Table 3-1.

Facies #	Description	Interpreted Depositional Mechanism(s)
1.A)	Matrix-poor, normally graded to massive, structureless sandstone	Rapid sediment fallout from mixed mud-/sand-rich turbidity current.
1.B)	Matrix-intermediate, massive to normally graded, structureless, clayey sandstone	
2	Matrix-rich, massive, structureless, sandy claystone	Deposition from a plug flow with developing cohesive strength undergoing en masse deposition from a cohesive gel.
3.A)	Thin-bedded, traction-structured sandstone	Low-density turbidity current with competence-driven deposition. Equivalent to Bouma Tc-d turbidites.
3.B)	Thick- and thin-bedded, traction-structured sandstone and siltstone	Low-density turbidity current undergoing competence-driven deposition. Equivalent to Bouma Tb-d turbidites.
4	Massive to graded mudstone	En masse deposition of a fluid mud layer or suspension settling; equivalent to a Bouma Te turbidite.

Table 3-1 Summary of Facies

The interpreted depositional mechanisms of Facies 1 and 2 are principally supported by their lateral facies association. Therefore, to provide better context for the interpretation of these strata, their interpreted depositional mechanisms will be discussed following the description of their lateral facies associations in Chapter 4.2 (Lateral Facies Association Interpretation). Facies 3 and 4, on the other hand, are described and interpreted below.

3.1 Terminology

Based on thin section and field observations three categories of matrix content are recognized: matrix-poor (<20% matrix), matrix-intermediate (20-50% matrix), and matrix-rich (50-90% matrix). Following these matrix divisions, this study follows a modified Folk's classification scheme (1964) (Figure 3-1) where matrix-rich strata are equivalent to sandy-claystone; matrix-intermediate strata are clayey-sandstone, and matrix-poor sandstones are sandstone.

In thin section, matrix is composed predominantly of recrystallized clay and minor silt grains. Additionally, increasing chlorite content in matrix-intermediate to matrix-rich sandstones correlates well with their progressively darker green/blue hue in the field (Figure 3-2). Therefore, matrix content can be visually estimated based simply on colour.

In thin section, matrix-poor sandstones have abundant recrystallized quartz grains (26% average content) compared with 12% and 3% in matrix-intermediate and matrix-rich types, respectively. This difference reflects differences in tectonic strain relaxation, principally by grain-margin bulging and growth of recrystallized grains in matrix-poor sandstones compared with ductile slip in the other kinds (Popović 2016). Additionally, matrix-poor sandstones contain

abundant diagenetic carbonate cement (up to 14%, with an average of 4%), compared with 1% and 0%, in matrix-intermediate and matrix-rich sandstones, respectively.

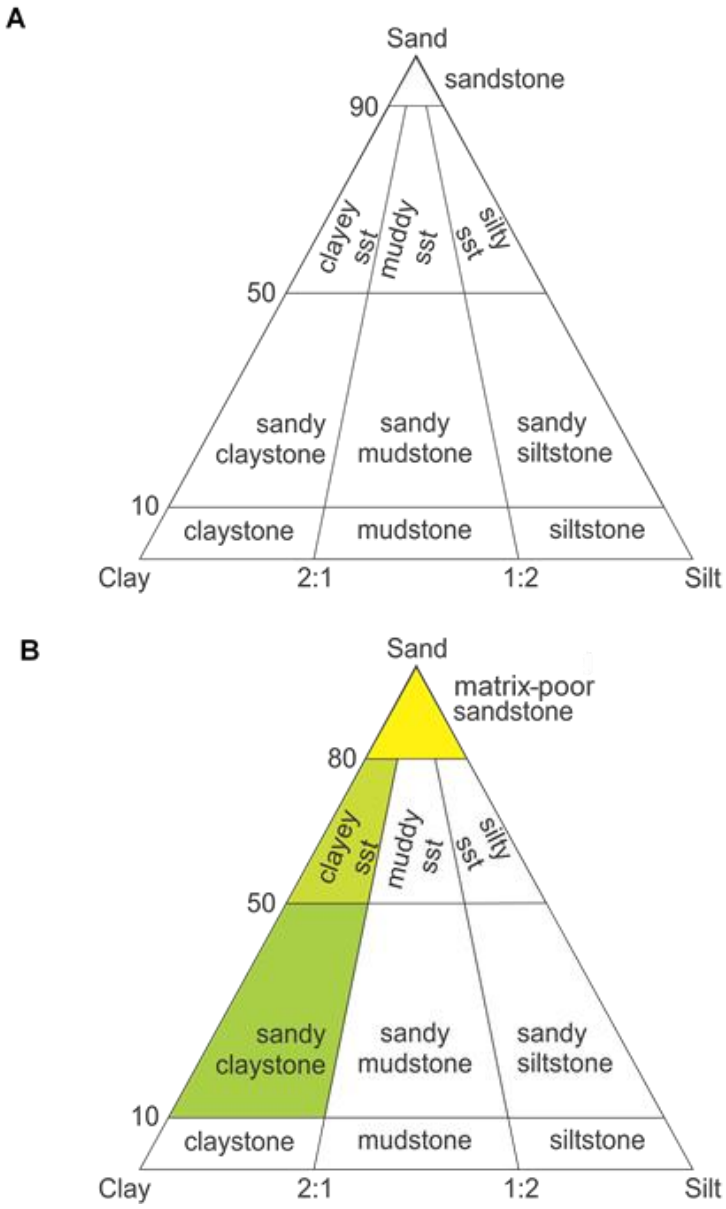

Figure 3-1 **A)** Folk's classification (1964) for siliciclastic sedimentary rocks. **B)** Modified Folk classification used in this study. Coloured divisions correspond to descriptions used in this study (modified from Tucker 1981).

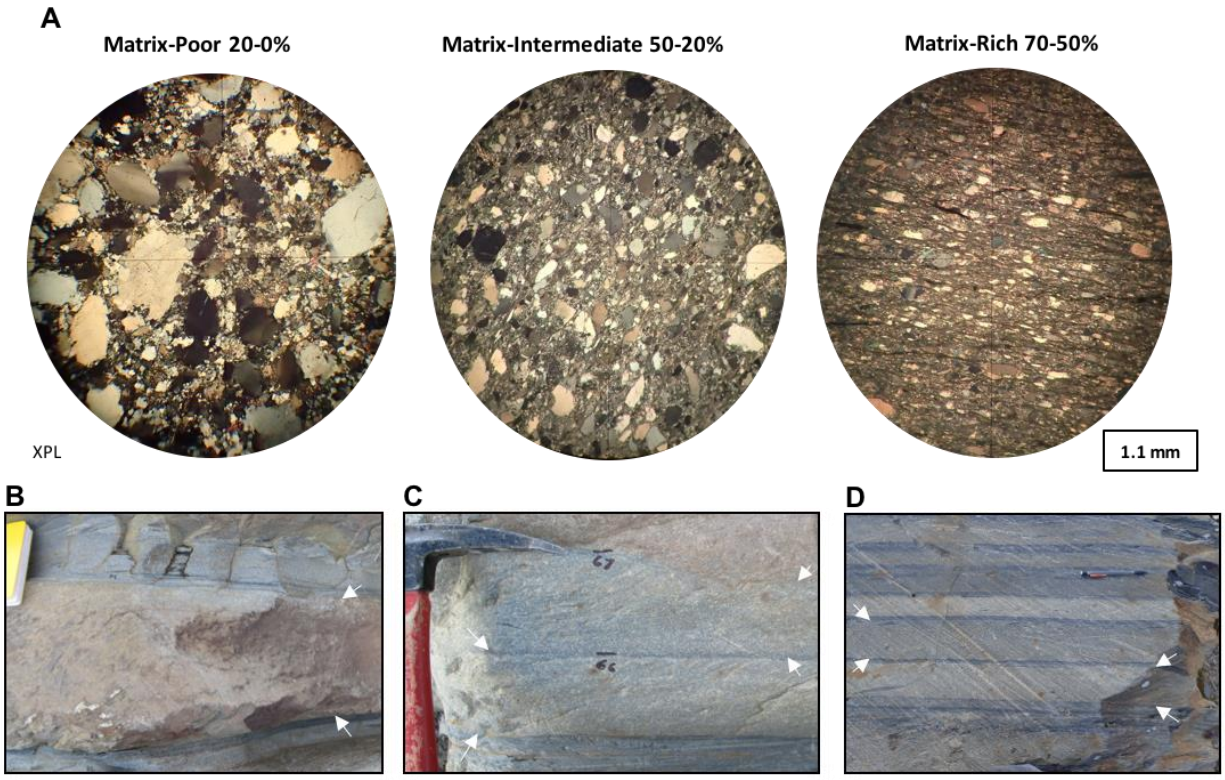

Figure 3-2 **A)** From left to right photomicrographs of matrix-poor, -intermediate, and –rich divisions. Photographs of a matrix-poor sandstone **(B)**, clayey sandstone **(C)**, and sandy claystone **(D)**. Note the correlation between matrix and stratal colour (**white arrows** indicate bed base and tops).

3.2 Facies 1.A: Matrix-Poor, Normally Graded to Massive, Structureless Sandstone

Facies 1.A (F1.A) consists of tan, structureless, normally graded to massive sandstone with less than 20% matrix (Figure 3-3). Based on 341 occurrences beds range from 8-136 cm thick, but on average are 27 cm thick. Basal contacts are commonly sharp and planar (43% of beds), but can also be wavy (36%), undulatory (11%) or scoured (10%) – scours are typically less than 10 cm deep. Flame structures occur in 33% of beds and average 3 cm in length and 5 cm in width, but range up to 10 cm long and over 30 cm wide. Strata are most commonly normally graded (48%) but also massive (36%), and coarse-tail graded (16%).

At the base of beds, grain size is typically lower-coarse to lower-medium sand, with dispersed very-coarse sand grains to granules. However, very near the base of the bed can be as coarse as upper very coarse to upper coarse. At the top of beds, grain size is typically lower-medium to lower-fine sand with dispersed upper-coarse to lower-very-coarse sand. Beds are structureless and lack dewatering structures. Clasts, typically mudstone or less commonly interlaminated siltstone-mudstone, occur in 54% of beds and have an average thickness of 1 cm by 9 cm in length but range up to 9 cm and 60 cm in thickness and length, respectively. Clasts are sub-angular and typically oriented subparallel to bedding. Where present clasts are dispersed throughout the bed and make up ~ 5-15% of the bed volume.

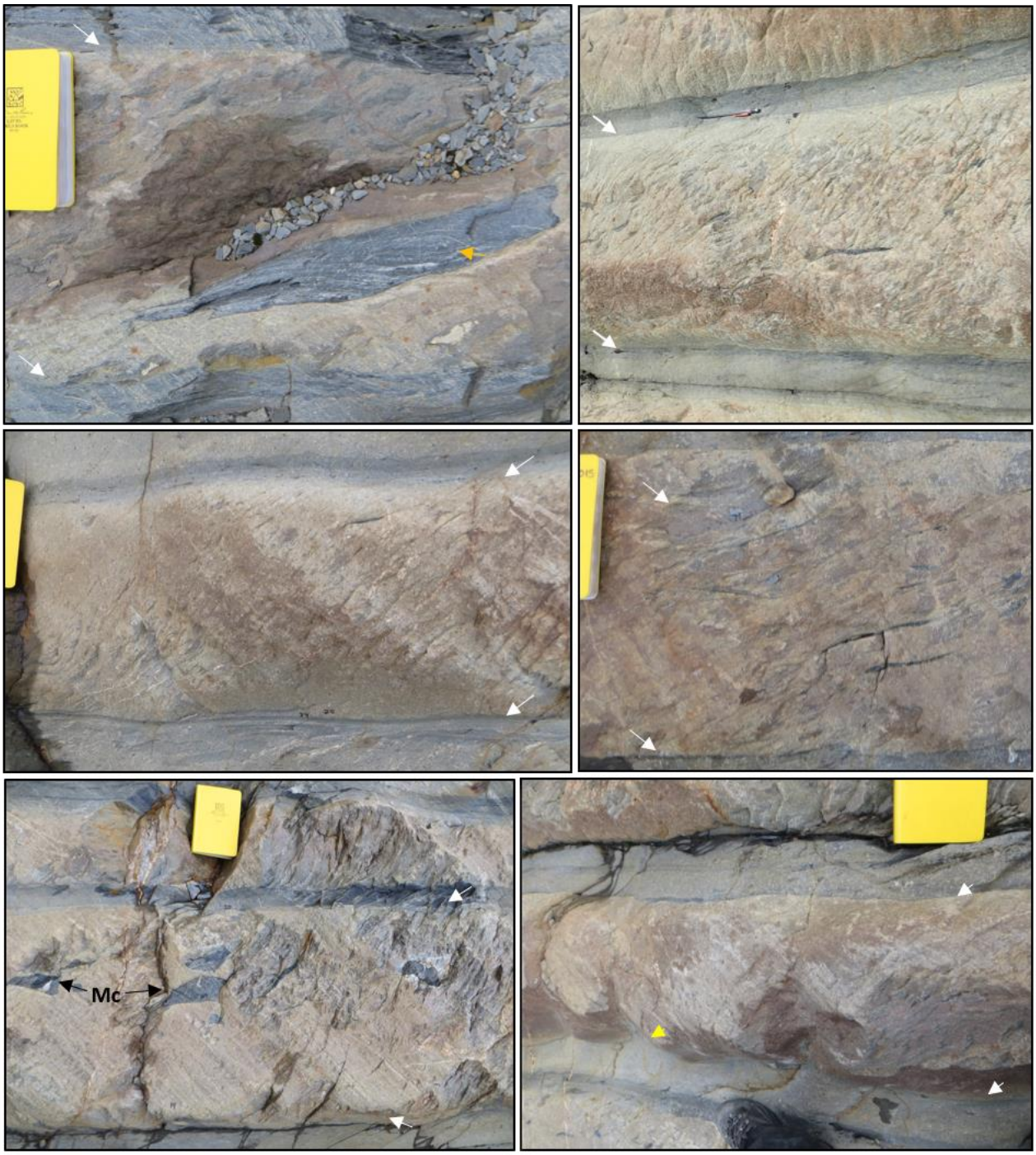

Figure 3-3 Field photographs of Facies 1.A sandstone. **White arrows** indicate bottom and top contact of bed. Note the interlaminated mud clast **(orange arrow)** and the common undulatory to wavy basal contact with local flame structures **(yellow arrow)**. Black arrows indicate mudstone clasts **(Mc)**.

3.2.1 Petrography (Facies 1.A)

Based on the analysis and point counting of 16 thin sections, Facies 1.A) is poorly sorted, to very poorly sorted with sub-rounded to sub-angular, equant to elongate framework grains. Framework grains are mostly monocrystalline quartz (35-72%, average 53%) with minor feldspar (0-3%, average 1%). Recrystallized quartz grains are common and makeup 12-42% of the volume (average 26%) (Figure 3-4). Matrix ranges between 8-20% (average 16%) and is composed mostly of silt or finer-grained muscovite and chlorite. Carbonate cement ranges between 0-14% (4% average) and is made up of calcite or rhombohedral dolomite. Euhedral pyrite crystals, although observed, represent < 1% of all points counted.

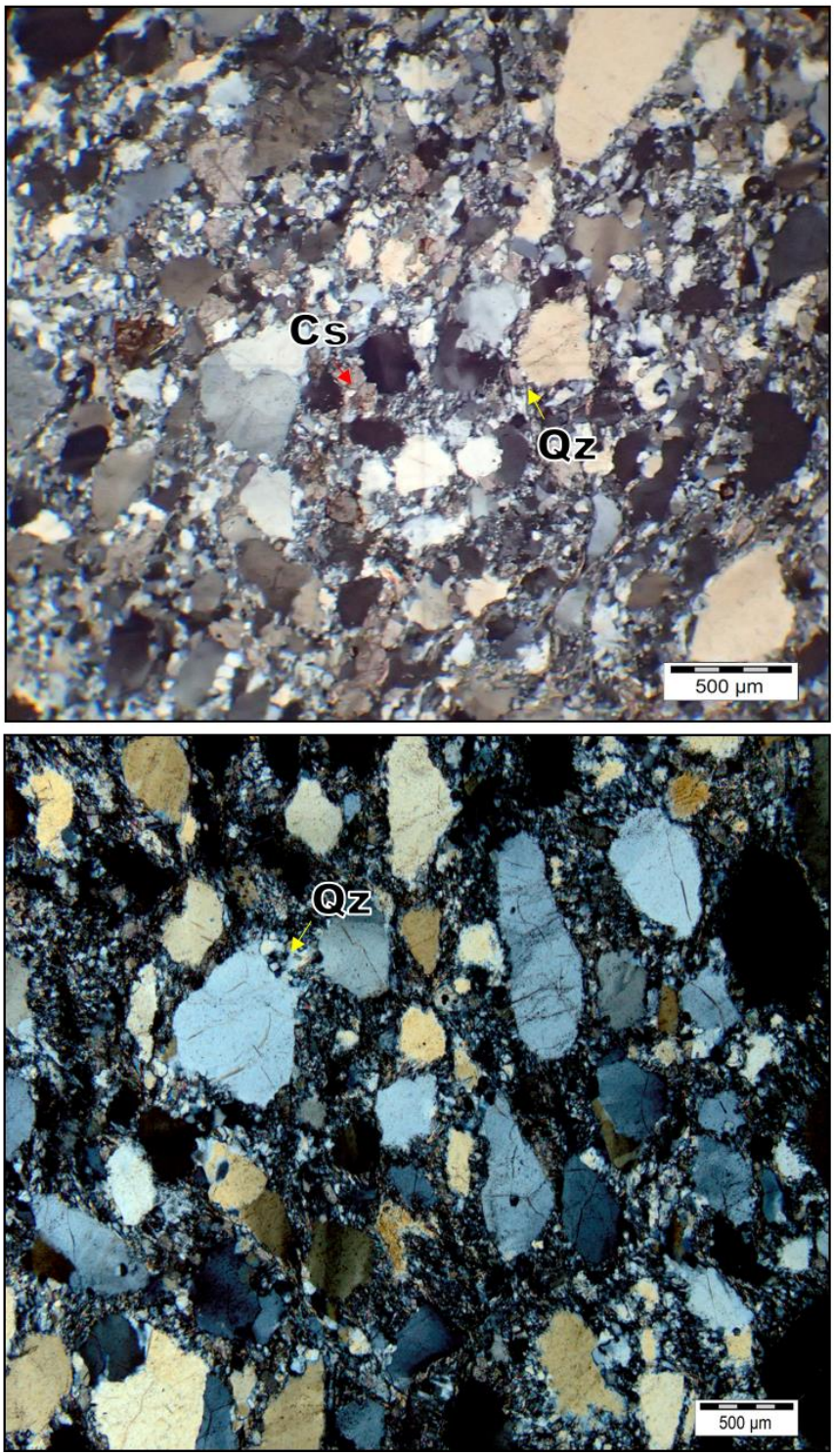

Figure 3-4 Photomicrographs of matrix-poor sandstone (top photomicrograph 0% matrix, bottom 12% matrix). Red arrow **(Cs)** denotes recrystallized calcite cement. Yellow arrow **(Qz)** points to recrystallized quartz grain boundaries

3.3 Facies 1.B: Massive to Normally Graded, Structureless, Clayey Sandstone

Facies 1.B (F1.B) comprises light grey coloured, structureless, massive to normally graded sandstone (Figure 3-5). Based on the description of 133 beds, Facies 1.B ranges from 3-58 cm thick and averages about 10 cm thick. Basal contacts are typically sharp and planar (62% of beds), although wavy (23%), undulatory (9%) and scoured (6%) contacts are observed. Flame structures are uncommon (13% of beds) but where present are 3 cm long and ~1 cm wide .

Based on the distribution of grains, beds are typically massive (53% of beds), although 30% of beds are crudely normally graded or coarse-tail graded (17%). At the base of beds grain size is commonly upper-medium to lower-fine sand with dispersed lower-coarse sand grains, which grades to lower-medium to upper-fine sand with dispersed grains of upper-medium sand at the top of beds. Traction sedimentary structures, including dewatering structures, are absent. Clasts, which are elongate, sub-angular to sub-rounded and typically oriented subparallel to bedding, consist of massive mudstone and much less common interlaminated siltstone-mudstone. They occur in 52% of beds and range from 0.2-12 cm thick to 1-25 cm long, but are generally ~1 cm thick and 6 cm long. Where present, clasts are usually dispersed throughout the bed and can make up ~5-15% of the bed volume.

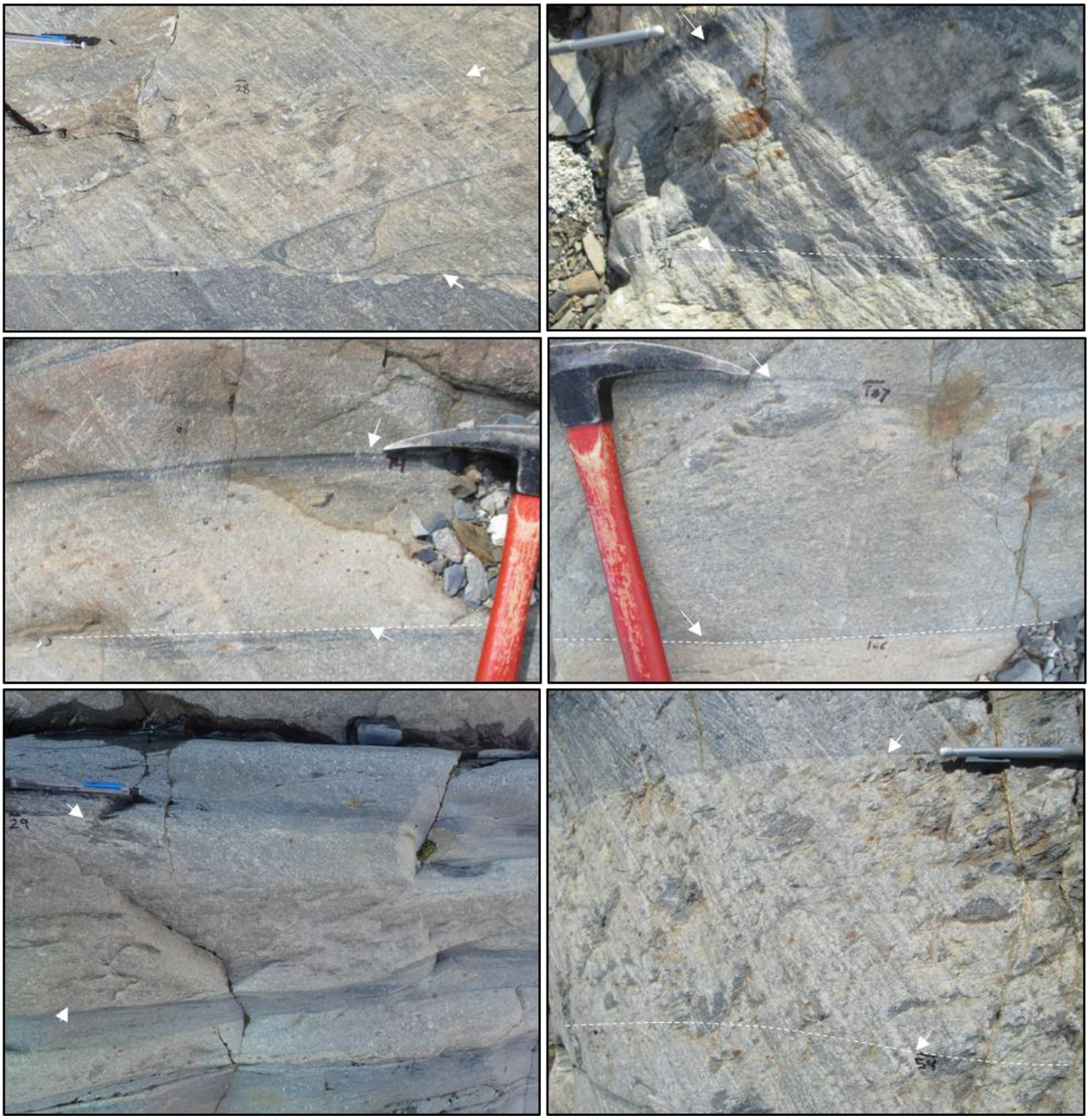

Figure 3-5 Field photographs of Facies 1.B) clayey sandstone. **White arrows** indicate bed base and top. **White dashed line** indicates an amalgamated bed contact. Hammer or pencil for scale.

3.3.1 Petrography (Facies 1.B)

Based on the analysis of 24 thin sections, the volume of Facies 1.B strata consists of 38-65% (50% average) framework grains dominated by monocrystalline quartz (99%) and rare (1%) feldspar, which most likely is plagioclase. Grains are typically sub-angular to sub-rounded and equate to elongate. Matrix ranges from 23-49% (35% average) of total stratal volume (Figure 3-6). Rare chlorite grains up to almost 0.25 mm are observed. Recrystallized quartz grains make up 3-26% (average 12%) of the stratal volume and typically occur adjacent to detrital quartz sand grains. Carbonate cement, although present, typically accounts for only 1% of stratal volume, but rarely ranges up to 8%.

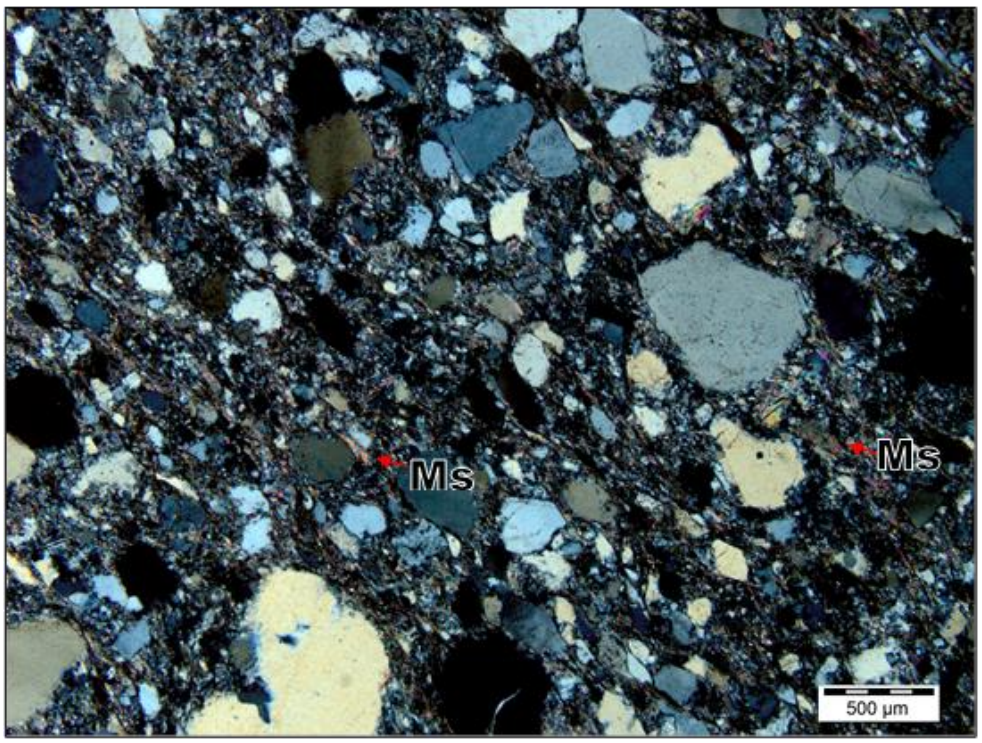

Figure 3-6 Photomicrographs of clayey sandstone (32% recrystallized matrix). **Red arrows** indicate elongate crystals of muscovite **(Ms).**

3.4 Facies 2: Massive, Structureless Sandy-Claystone

Facies 2 (F2) is a dark grey to green/blue, structureless claystone consisting of 50-90% matrix with dispersed sand grains (Figure 3-7). Based on 341 observations, beds range from 1 – 66 cm in thickness, and average 7 cm. Basal contacts are most commonly sharp and planar (79% of beds) or uncommonly wavy. Basal flame structures are rare (6% of beds) and typically less than 2 cm long and 3 cm wide. Based on the distribution of grains, beds are most commonly massive (68% of beds) to coarse-tail (18%) or subtly normally graded (14%). Near the base of beds grain size is most commonly lower-medium to upper-fine sand with dispersed upper-medium sand. Rare coarse and very-coarse sand grains are observed in thin section. Grain size at the top of beds ranges from upper-fine to lower-fine sand. Dewatering or tractional sedimentary structures are absent. Clasts occur in 56% of beds and range from 0.1-7.5 cm thick by 0.5-97 cm wide, but on average are 1 cm thick and 10 cm long. Typically they are composed of massive mudstone, lesser interlaminated siltstone-mudstone, and rarely lower-fine to upper-medium sand. Moreover, clasts are typically elongate, sub-angular to sub-rounded, oriented subparallel to bedding; and, where present, dispersed throughout the bed.

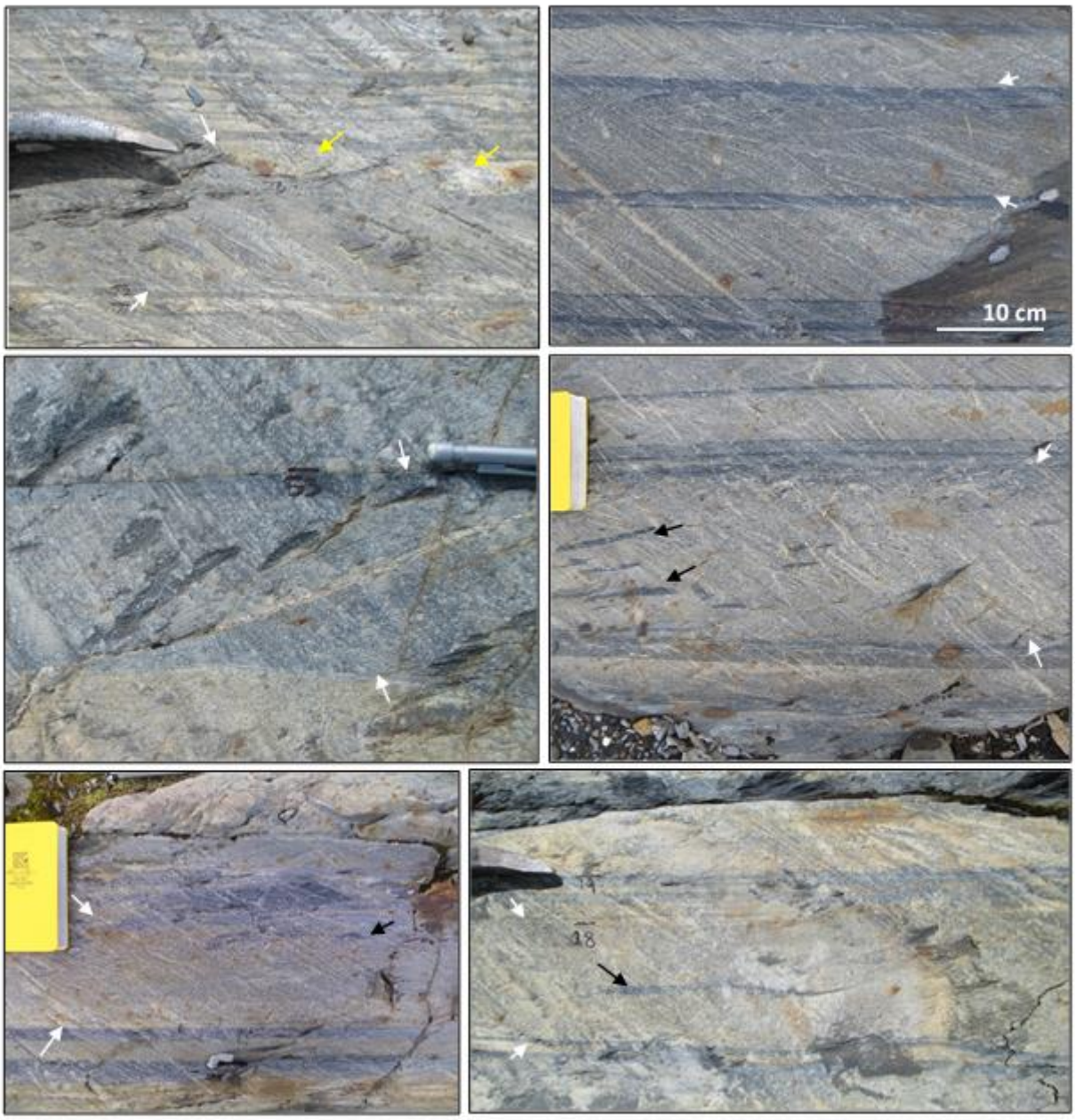

Figure 3-7 Field photos of sandy claystone Facies 2. Note that each bed is capped by a 0.5-2 cm mudstone (Facies 4). **White arrows** denote bed base and top. **Black arrows** point to mud clasts. **Yellow arrows** indicate very-fine, ripple-cross-stratified sandstone that commonly founder (i.e. load) into the top of underlying facies 4 strata. Field book, pencil or tip of hammer for scale.

3.4.1 Petrography (Facies 2)

Based on the analysis of 14 thin sections, Facies 2 consists of 54-87% matrix, with an average of 63%. Matrix is composed mostly of muscovite and chlorite crystals, and lesser silt grains (Figure 3-8). Grains make up 12-42% of Facies 2 and are composed of quartz (99%) and minor feldspar (~1%) that are sub-rounded to sub-angular and equant to elongate. Furthermore, grains, including those up to very-coarse sand, are dispersed (i.e. “floating”) in matrix. Recrystallized quartz grains range between 0-8% with an average content of 3%. Carbonate cement was also rare (>1%).

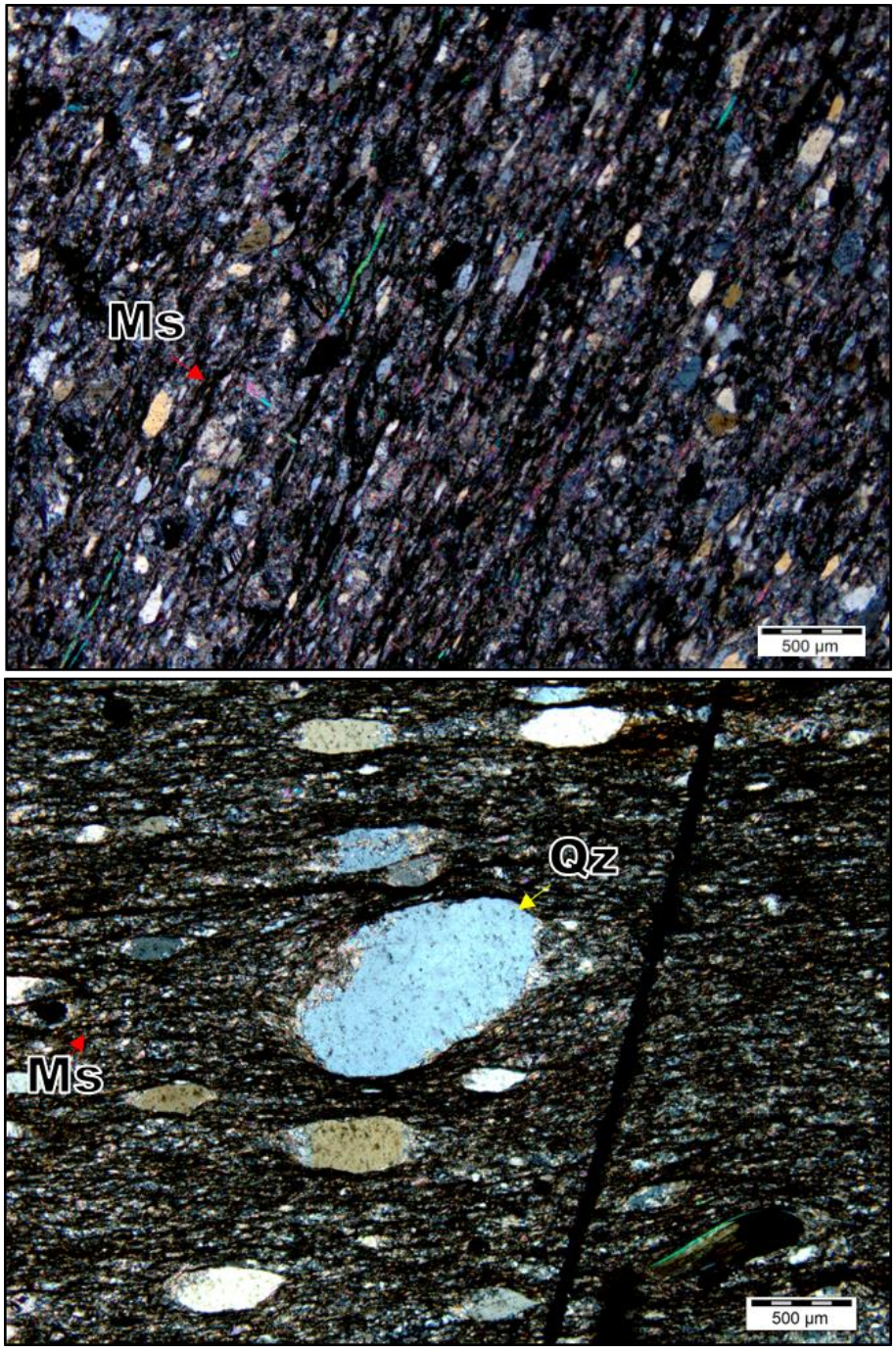

Figure 3-8 Photomicrographs of sandy claystone. Yellow arrow **(Qz)** indicates very coarse sand grain suspended in a recrystallized matrix composed mostly of muscovite **(Ms).** The well-developed fabric (i.e. grain alignment) is a consequence of a pervasive tectonic cleavage.

3.5 Facies 3.A: Thin-Bedded, Traction-Structured Sandstone and Siltstone

Facies 3.A (F3.A) consists of pink to yellow-tan, thin-bedded, traction-structured sandstone overlain by diffusely laminated siltstone (Figure 3-9). Basal contacts are sharp and planar and beds range from 1-5 cm thick (most commonly <2 cm). Grain size ranges from fine sand to silt. Sandstone in the lower part of beds is commonly small-scale cross-stratified (< 4 cm thick) with no visible angle of climb. Cross-stratification typically occurs as a single set. These strata are usually overlain by diffusely laminated, plane-parallel to wavy-parallel, mud-rich and mud-poor laminae (<2 mm) composed of very-fine sand to silt (Td). Occasionally, laminations increase in thickness and abundance vertically. Uncommonly, cross-stratified sandstone will founder into the underlying basal bed.

Figure 3-9 **A)** Single ripple cross-stratified form set **(yellow arrow).** Mud preferentially fills the ripple troughs **(orange arrow). B)** Outcrop photograph of an ~1 cm-thick, planar stratified, fine-grained sandstone. Vertical to sub-vertical striations are a product of rock saw cutting.

3.6 Facies 3B: Thin- to Thick-Bedded, Traction Structured Sandstone

Facies 3.B) comprises thin- to thick-bedded, pink to yellow-tan, traction-structured sandstone (Figure 3-10). Bed bases are commonly sharp and planar and bed thickness ranges between 10-150 cm (average of 28 cm). At the base of the bed, strata consist of medium-grained, planar-stratified (Tb) sandstone with dispersed coarse sand grains, and constitutes ~70% of the bed thickness. This, is commonly, but not always, overlain by fine- or very fine-grained sandstone consisting of single, or less commonly multiple (up to 3) small-scale (<4 cm thick) cross-stratified sets (Tc) with no visible angle of climb. These are capped by 1-3 cm of diffusely laminated silt to very find sand (Td). Commonly, traction-structured sandstones are composed of medium to fine sand, multi-set ripple cross-stratified sandstone (Tc) overlain by 1-5 cm diffusely laminated silt to very fine sand (Td). Multi-set-ripple cross-stratification (Tc) is composed of well-sorted, medium to very-fine sand and ranges from 1-30 cm thick with 2-7 ripple sets, although up to ~15 ripple sets are observed.

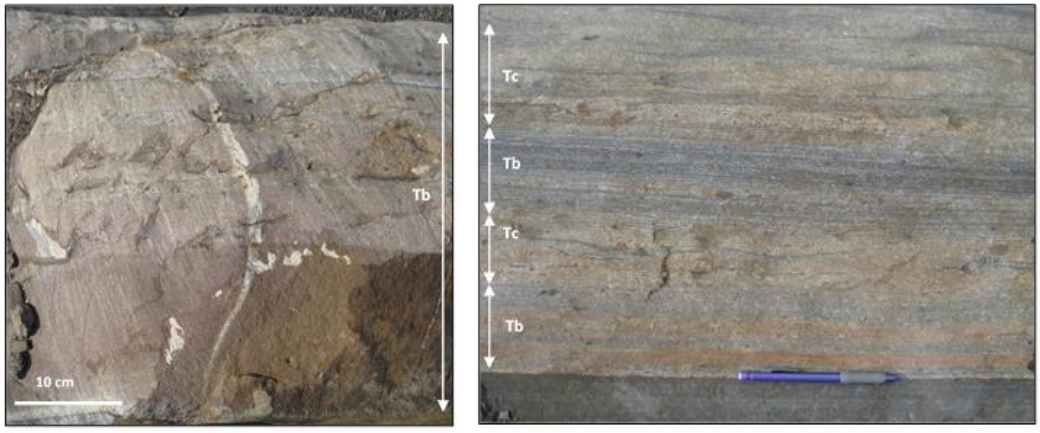

Figure 3-10 Field photographs of traction-structured sandstone. **Left** - Medium-bedded, planar-stratified medium- to fine-grained sandstone. **Right** - Thin-bedded, planar- to ripple cross-stratified, fine-grained sandstone.

3.6.1 Petrography (Facies 3.A and 3.B)

Cross-stratified and diffusely planar-laminated divisions in Facies 3.A are composed predominately of well-sorted framework grains (See Figure 3-11, A). Lamination observed in outcrop is produced by alternating mud-poor and mud-rich lamina, in which mud-poor laminae are composed of well-sorted, fine sand to silt quartz grains.

The basal planar-stratified part of facies 3.B is dominated by well-sorted, quartz (62-88%) and lesser feldspar (0-2%) grains (most likely plagioclase) (see Figure 3-11, B). Quartz grains are typically monocrystalline with moderate to strong undulose extinction. Framework grains show prominent sutured grain contacts. Recrystallized quartz grains comprise 34-65% of framework grains and matrix represents 0-12% for the stratal volume. Local carbonate cement ranges between 9-25% and euhedral pyrite crystals (<1%).

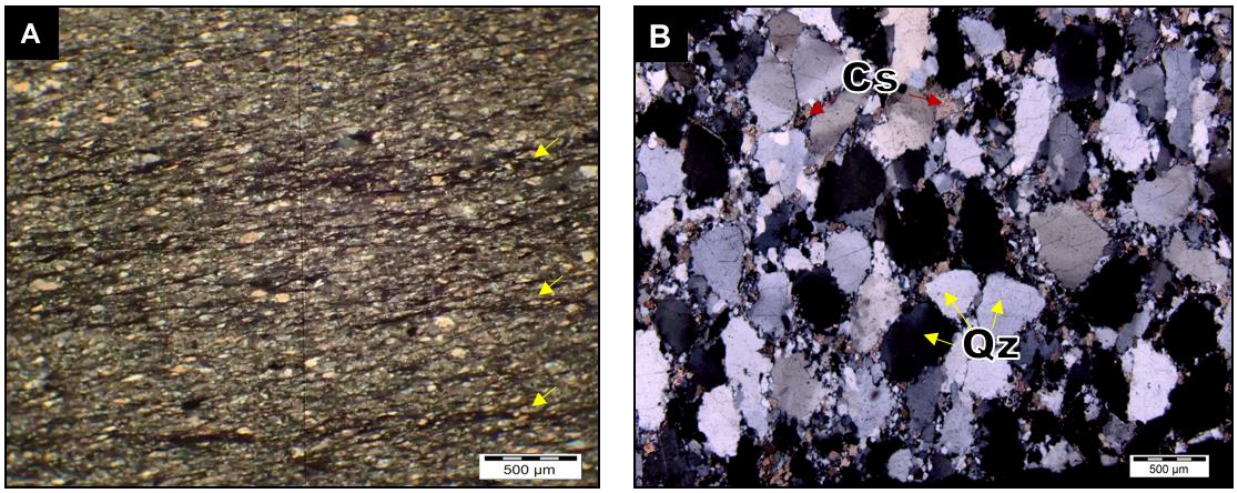

Figure 3-11 **A)** Photomicrograph of a thin-bedded, well-sorted, planar-stratified, fine-grained sandstone (Tb). Yellow arrows indicate mud-rich laminae that sub-parallel tectonic cleavage. **B)** Photomicrograph of a thick-bedded, planar-stratified, medium-grained sandstone (Tb). **Qz** signifies quartz grain. Note the lobate and interfingered grain boundaries indicating extensive tectonically-induced recrystallization. **Cs** denotes carbonate cement.

3.6.2 Interpretation

The well-sorted, normally-graded nature of the deposits, in conjunction with planar overlain by small-scale cross-stratification, or simply cross-stratification, are interpreted to represent incomplete classical turbidites (Tbcd, Tbd, and Tcd) (Bouma 1962). These strata indicate deposition by low concentration, fully turbulent, turbidity currents in which sediment fallout rates were low, and sediment was transported and deposited predominantly from the bed load fraction. Under these conditions sediment is sorted on the bed principally by its grain size, which in turn develops textural variations, specifically planar stratification of the Bouma Tb division (Sumner et al. 2008). In the presence of a bed defect ,flow separation becomes initiated and, due to high near-bed shear stresses at the point of flow reattachment, causes the initiation of an evergrowing expanse of new defects (Best 1992). With sustained flow, defects become amplified and evolve into angular bed forms like ripples, and apparently, rarely dunes (e.g. Arnott 2012)). Avalanching on the lee side of ripples forms the well-sorted, small-scale cross-stratified Tc division in the Bouma sequence. As flow speed continues to wane, sediment in suspension is intermittently able to fall directly from suspension; although minor bed load transport may still be persistent, producing the discontinuously and/or diffusely laminated Td division.

3.7 Facies 4: Massive to Graded Mudstone

Facies 4 consists of a massive to graded silty mudstone. Basal contacts are sharp and planar. Flame structures, which are less than 0.5 cm long and 0.5 cm wide, were observed, but are rare. Mud caps are usually < 1 cm and rarely up to 2 cm thick, and drape the topography along the top of the underlying bed; for example, thickening and thinning in the troughs and over the crests, respectively, of underlying ripple formsets. The rhythmic intercalation of plane- or wavy-parallel mud-rich and mud-poor laminations (<2 mm) is common (see Figure 3-12, A). In some beds, mud-rich laminae become thicker and more abundant upward. Dewatering structures and mud clasts are absent.

3.7.1 Petrography (Facies 4)

Commonly at the base of Facies 4 is a thin (<0.1 mm) veneer of silt that separates the base of the mudstone cap from the top of an underlying bed (see Figure 3-12 B and C). Laminations observed in outcrop are produced by the intercalation of mud-poor and mud-rich lamina, in which mud-poor lamina is composed of well-sorted silt. Additionally, thin (<0.3 mm) mud-rich lamina are better sorted (i.e. less abundant silt) and have sharper contacts than thicker (>0.3 mm) mud-rich lamina, which are poorly sorted and show diffuse gradational contacts. Diffusely laminated mudstone is typically overlain by a normally graded interval, which grades from silt to mudstone, or muddy-siltstone to mudstone. However, some mudstone caps may be massive and poorly sorted, with dispersed silt grains.

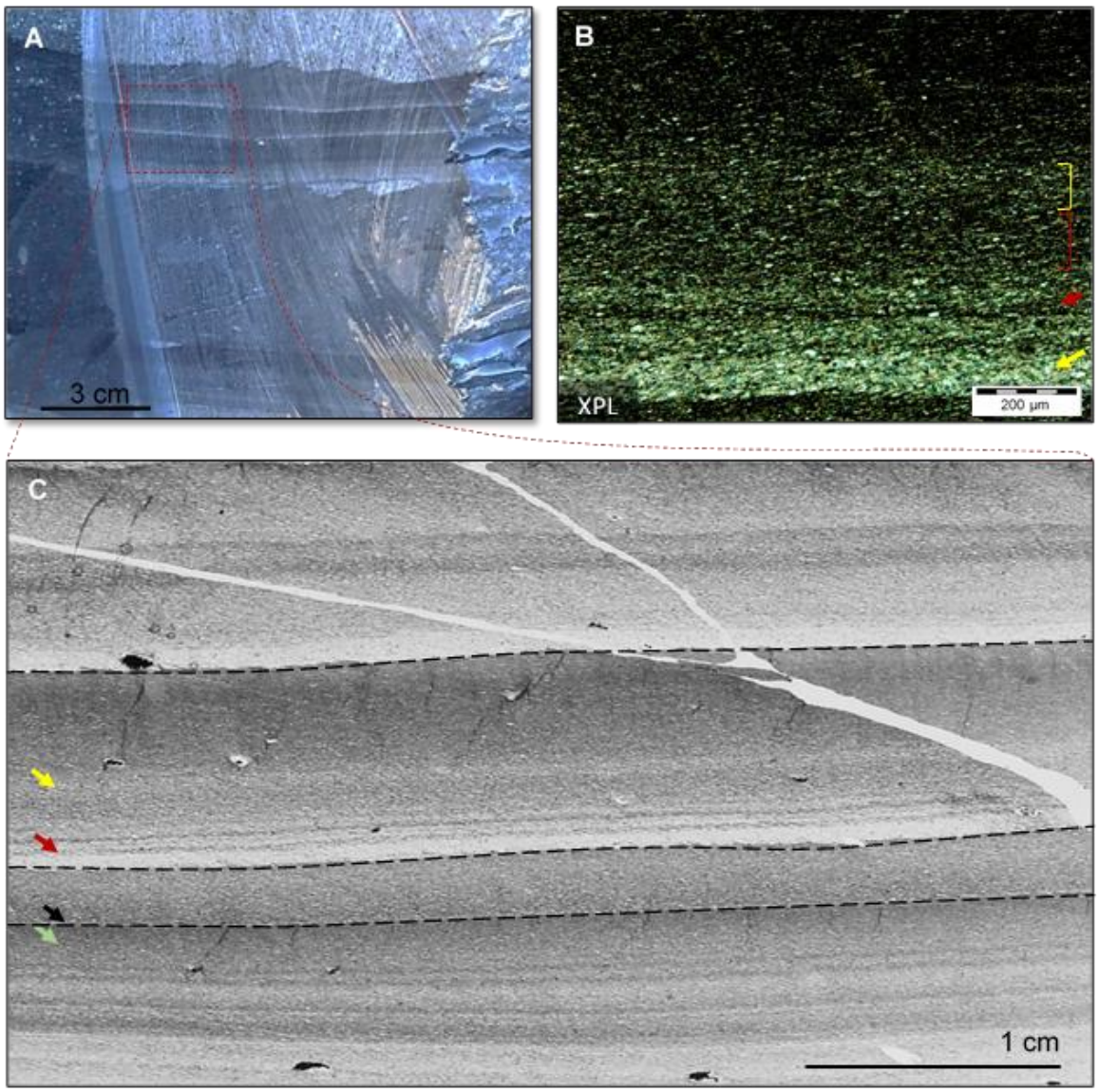

Figure 3-12 **A)** Outcrop photograph showing several well-developed mudstone caps overlying a clayey sandstone (Facies 2). **Red dashed rectangle** denotes the location of photo **C)**. **B)** Photomicrograph of a mudstone cap. **Yellow arrow** indicates a mud-poor lamina. **Red arrow** designates a mud-rich lamina. **Red bracket** denotes a gradational, poorly-sorted, mud-rich lamina. **Yellow bracket** marks mud-poor diffuse lamina. **C)** Thin section scan of four mudstone to silty mudstone caps (Facies 4) (**black dashed line** designates bed boundaries). **Green arrow** designates a gradational silty mudstone to mudstone interval. Also, a sharp and planar silt veneer typically separates the basal mudstone, from the overlying poorly sorted mudstone (**black arrow**). The **red arrow** designates a sharp, mud-rich, planar lamina, while the **yellow arrow** marks a diffuse mud-poor band. Note that laminations observed in outcrop are produced by the alternation of mud-poor and mud-rich lamina.

3.7.2 Interpretation

The origin of mud-rich and mud-poor banding of muddy-siltstones to silty-mudstones might result from the breakup of particle floccules containing both mud and silt in a turbulent boundary layer beneath a dilute suspension. The breakup of flocs initially causes the deposition of silt, which is then followed gradually by the reflocculation of the mud that eventually suppresses turbulence and leads to rapid mud deposition (Stow and Bowen 1978). This process then repeats, producing the alternating mud-rich and mud-poor layer. Massive, poorly-sorted, silty-mud caps, where silt grains are dispersed in a finer-grained matrix suggest that deposition possibly occurred by the en-masse deposition of fluid mud layer, in which high near-bed mud concentration created a gel-like rheology that prevented the settling of silt particles (McAnally et al. 2007). Where caps grade upward from silt to silty-mud, particles may have segregated by their different settling velocities as suspension settling or could be the result of post-depositional settling of particles in a fluid mud (Talling et al. 2012).

4 Lateral and Vertical Facies Associations

Detailed correlation of strata over a lateral distance of 350 m suggests a systematic change from sandstone (F1.A) to sandy claystone (F2). However, due to the limited lateral continuity of the exposure, the full transition was not observed in any single transect. Instead, an idealized succession was constructed by piecing together individual parts of the succession (Figure 4-1). The lateral trends reported in this study are consistent with those reported by Terlaky and Arnott (2014), Popović (2016) and Angus (2016) in areas where lateral exposure commonly exceeded 350 m.

Detailed descriptions of 11 stratigraphic logs, each containing between 63-137 individual beds for a total thickness of ~30 m, in addition to Markov chain analysis, was used to identify three vertical facies associations. Vertically, matrix-rich strata, including sandy claystones, bipartite beds, and clayey sandstones, were observed to stack on one another forming bed-sets. Additionally, a bed of matrix-poor sandstone was commonly observed to be overlain by one to three matrix-rich beds, forming a single bed-set. Multiple bed-sets then stack to form intercalated matrix-poor and matrix-rich assemblages. Lastly, traction-structured turbidites were observed to form assemblages.

4.1 Lateral Facies Succession

In general, sandstone (F1.A) grades laterally into clayey sandstone (F1.B). Further laterally, the clayey sandstone becomes sharply overlain by a sandy claystone (F2). Collectively, these two parts, which are separated by a sharp planar surface, form a single bipartite bed (see Figure 4-2, Figure 4-3 and Figure 4- 4). Further laterally, the lower clayey sandstone thins and then pinches out, at which point the upper sandy claystone (F2) comprises the entire bed. Nevertheless, further laterally it too thins and pinches out. Finally, the entire transect is draped by a traction-structured sandstone (F3. A) capped by claystone (F4). Due to the two-dimensionality of the outcrop and lack of paleocurrent control, the dimensions of the observed lateral changes most likely overestimate the true dimensions.

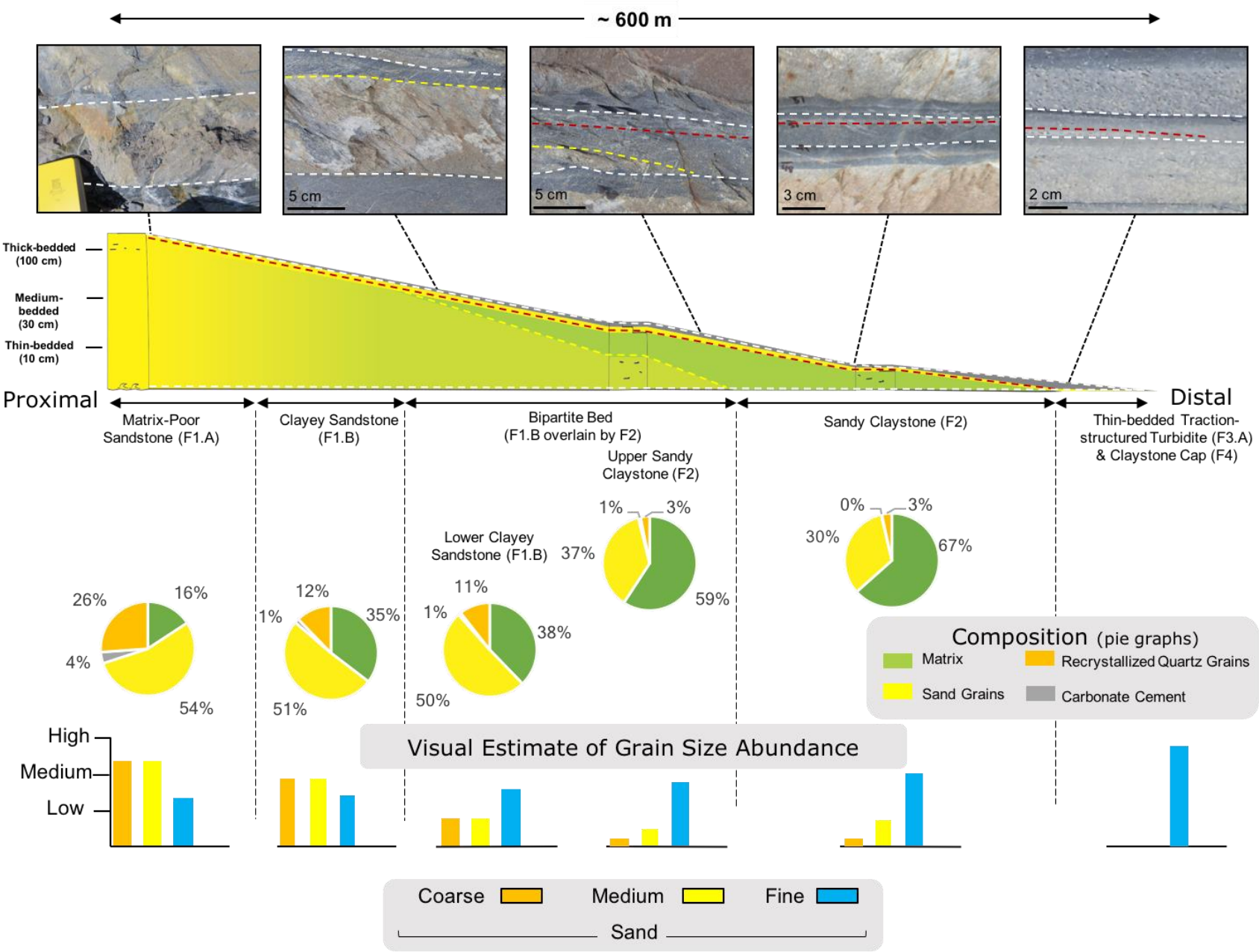

Figure 4-1. Caption on next page.

Figure 4-1 Schematic of the idealized lateral facies association from matrix-poor sandstone to clayey sandstone to bipartite to sandy claystone. A matrix-poor, thin-bedded, traction-structured cap and mudstone cap drape the entire transect. Note that the idealized transect is a compilation of several laterally extensive beds that individually show a part of the full transect. Along the transect beds change from thick- to medium-bedded to thin- to very thin-bedded, suggesting a proximal to distal trend. Additionally, modal grain size decreases to progressively more distal facies, however, the range of grain sizes changes little. **Pie-graphs** of point-count data showing composition of constituent components. Note the increase in matrix content from proximal to distal (right to left), while the abundance of sand grains, carbonate cement, and recrystallized quartz grains decreases. Visual estimates of grain size abundance were based on field observations and thin section analysis. Note that outcrop photographs are for illustration purposes only and are not along a single transect.

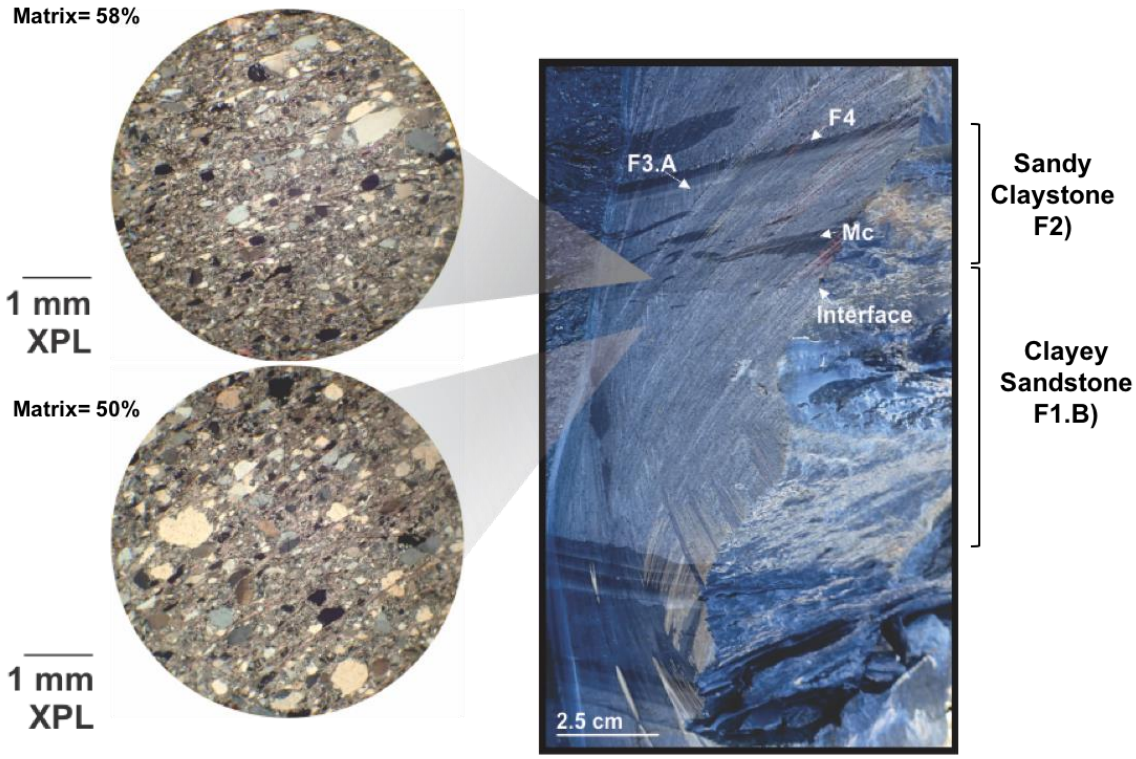

Figure 4-2 Outcrop photograph with accompanying photomicrographs of a bipartite bed. **Grey cones** indicate location of photomicrographs in outcrop. The lower photomicrograph was taken just below the interface (**black arrow**) in the basal clayey sandstone (F1.A), while the upper photomicrograph was taken just above the interface in the sandy claystone (F2). In outcrop, the interface between the underlying clayey sandstone and overlying sandy claystone is the product of a sharp increase in matrix content between the basal clayey sandstone (50%) and overlying sandy claystone (58%). Note also the dramatic decrease in medium and coarse sand grains and abundance of mudstone clasts (**Mc**) in the upper sandy claystone. Furthermore, the entire bed is capped by a thin-bedded upper division turbidite (Td) **(F3.A)** and claystone **(F4)**.

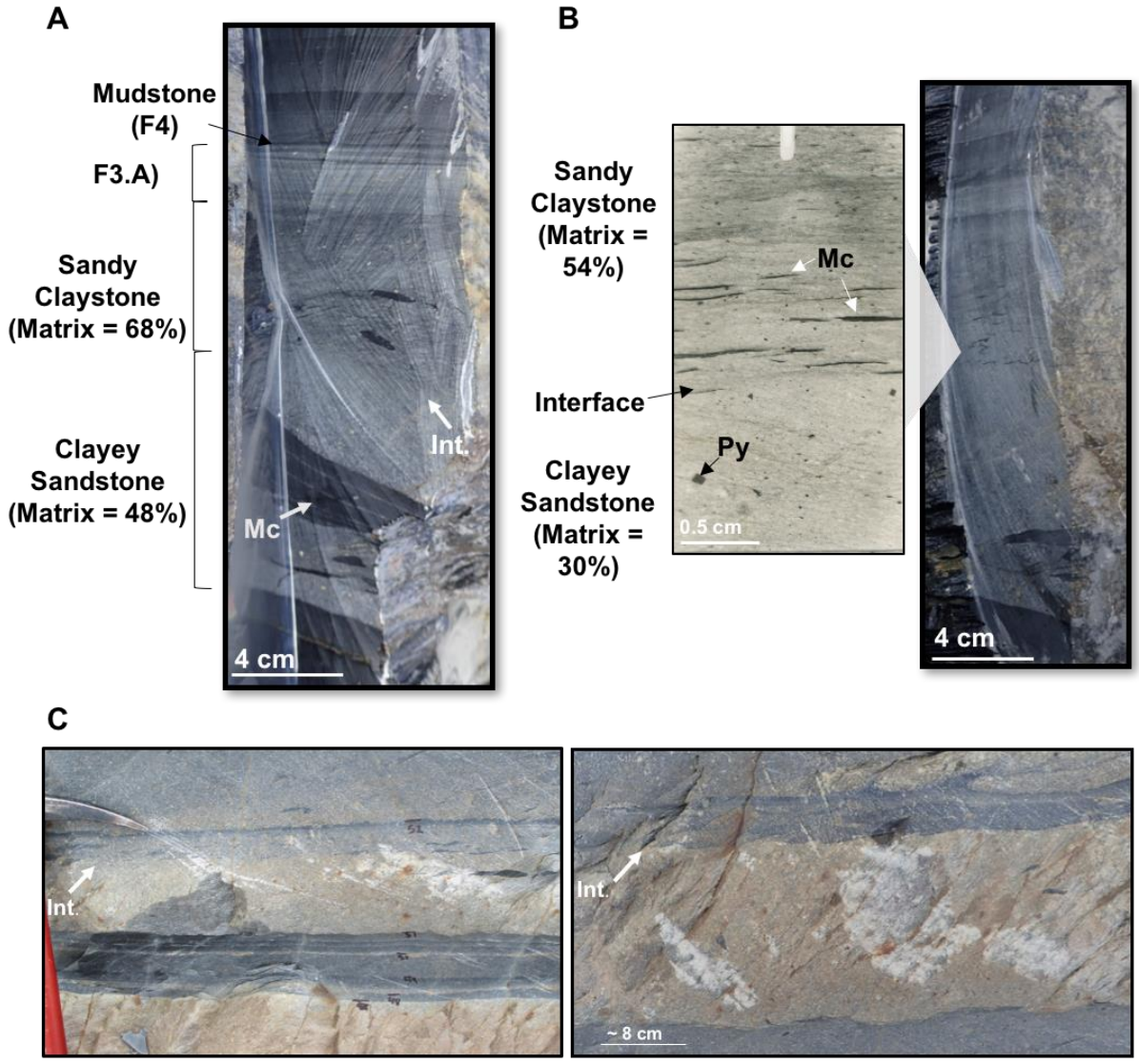

Figure 4-3 **A)** Photograph of cut (sawed) outcrop surface showing a bipartite bed with abundant mud clasts **(Mc)** in both the upper sandy claystone lower clayey sandstone parts of the bed. Note the large interlaminated mudstone clast (Mc), and also the ~ 2cm thick traction-structured (planar-stratified) Td (F3.A) overlain by claystone (F4) cap. **B)** Outcrop photograph (cut for sample collection) and accompanying thin section. Note the interface captured in thin section and the abundant (Mc) mud chips in the upper sandy claystone. The obliquely-dipping fabric in the lower more sand-rich part is tectonic cleavage, which notably becomes much more poorly developed in the upper, more mud-rich part. **Py** denotes digenetic, euhedral, pyrite crystals. **C)** Outcrop photographs of bipartite beds. **Int.** denotes the interface separating the basal clayey sandstone and overlying sandy claystone.

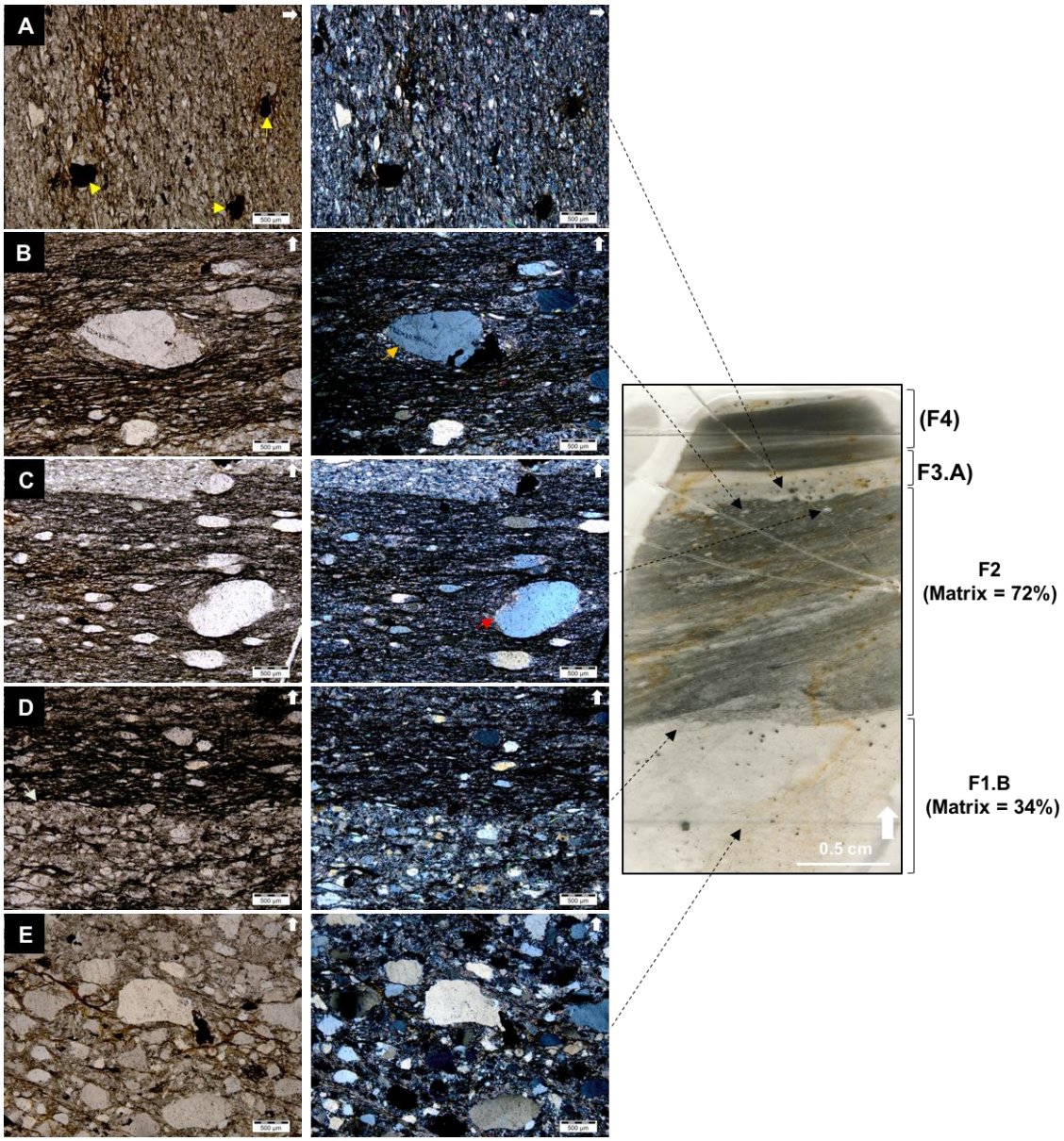

Figure 4-4 Photomicrographs taken from a bipartite bed. **Black arrows** designate location of photomicrographs from the scanned thin section (right). Plane polarized thin section photos in the left column. Cross-polarised thin section photos in the right column. Scale bars are 500 μm. **A)** photomicrograph of the well sorted, thin bedded traction structured sandstone. **Py** denotes digenetic pyrite. **B)** and **C)** Photomicrographs from the upper sandy claystone. Note the presence of suspended course to very course sand grains in matrix. **D)** photomicrograph of the interface separating the basal clayey sandstone and overlying clayey sandstone. Note the sharp planar contact and the dramatic decrease in sand grains across the interface. **E)** photomicrograph taken from the clayey sandstone. Note the presence of very course to coarse sand grains, indicating the range of grain sizes across the interface doesn't change.

4.1.1 Matrix Percentage

Based on point counting analysis of 22 thin sections from four beds, the following lateral matrix percentage trends were observed. In the most proximal, sand rich portion of the transect matrix poor sandstone (F1.A) contains ≤17% matrix. Laterally, matrix gradually increases to 23-30% as strata transition to clayey sandstone (F1.B). Further laterally, the matrix in clayey-sandstone remains unchanged or increases slightly to ~28-35%. At this point, an upper sandy claystone (F2) develops with an initial matrix content of 30-50%. After the pinch-out of the basal clayey sandstone, the upper sandy claystone progressively increases in matrix up to 54-70%, before it too pinches out. The overlying traction structured unit typically contains <10% matrix that changes negligibly over the length of the transect.

4.1.2 Grain size

Modal grain size progressively decreases from the sand-rich to the mud-rich part of the transect (Figure 4-5). Notably, however, the range of grain sizes changes little, an exception being granules, which are absent in the most mud-rich parts of the transect. Additionally, slight local increases and decreases in grain size were noted.

In the most sand rich part of the transect (F1.A), grain size at the base of beds ranges from very-coarse to fine sand, with dispersed granules. The top of the bed is better sorted, with grain size ranging from medium to fine sand with dispersed coarse grains. Changing laterally from sandstone to clayey-sandstone the modal grain size at the base of beds fines slightly to mostly fine to coarse sand with dispersed very coarse grains and rare granules. Grain size near the top of beds remains largely unchanged or fines slightly to medium to fine sand with dispersed

coarse grains to very coarse grains and rare granules. Laterally, the modal grain size at the bed base and top of the clayey sandstone fines to medium to fine sand with rare coarse sand grains. It is here that the upper sandy claystone layer begins to develop, and consists of a similar grain size distribution as the underlying sandy claystone or is slightly finer. Most commonly, the upper sandy claystone is massive with fine sand and dispersed lower-medium sand grains and rare coarse to very coarse grains. As the basal clayey sandstone (F1.B) thins and then pinches out, the sandy claystone (F2) consist of a uniform distribution of lower-fine to upper-fine sand with dispersed medium and rare coarse and very-coarse sand grains. The grain size of the overlying traction-structured cap (F3.A) is generally fine to very fine sand and changes negligibly over the width of the transect. The claystone (F4) that drapes the entire transect shows no change in grain size over the length of the transect.

Bed Thickness

Grain Size

Bed 1

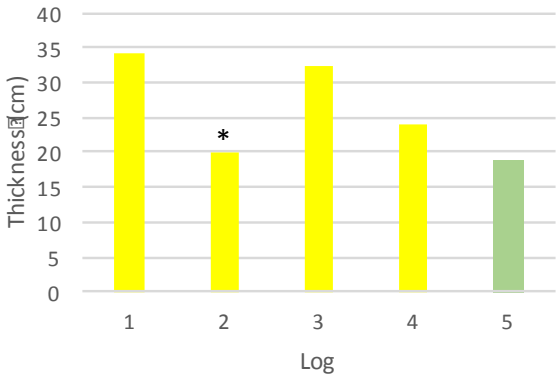

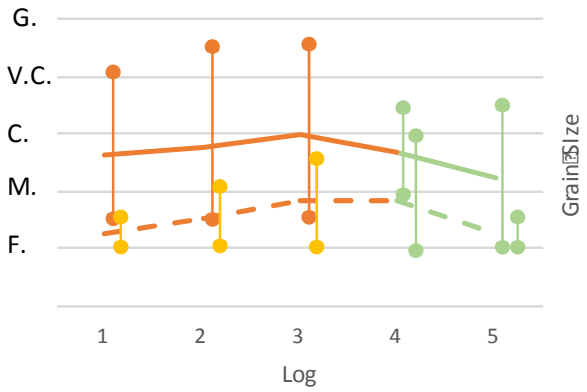

Bed 2

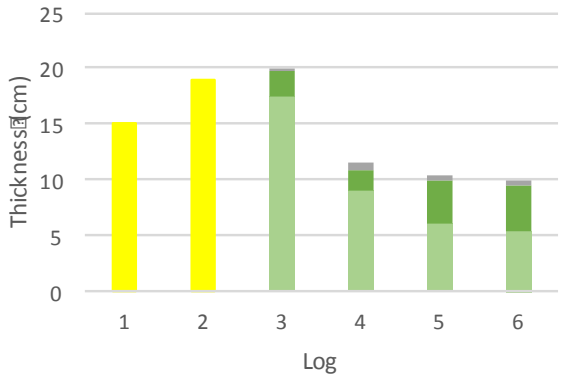

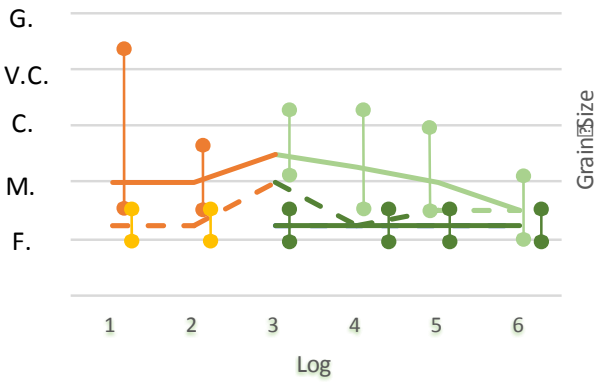

Bed 3

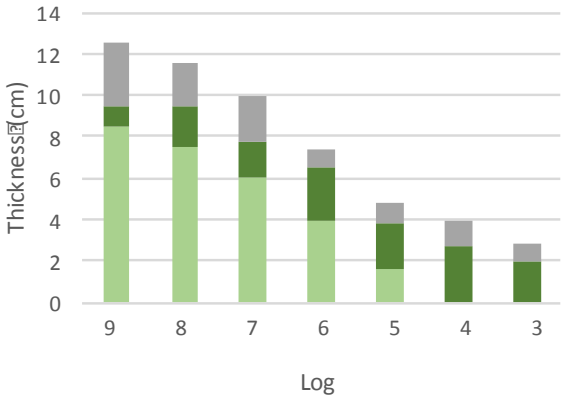

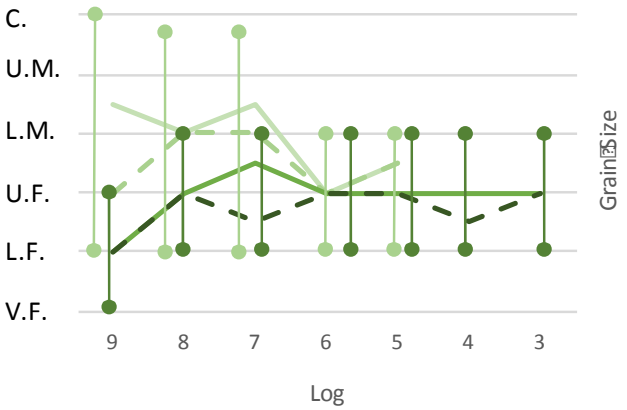

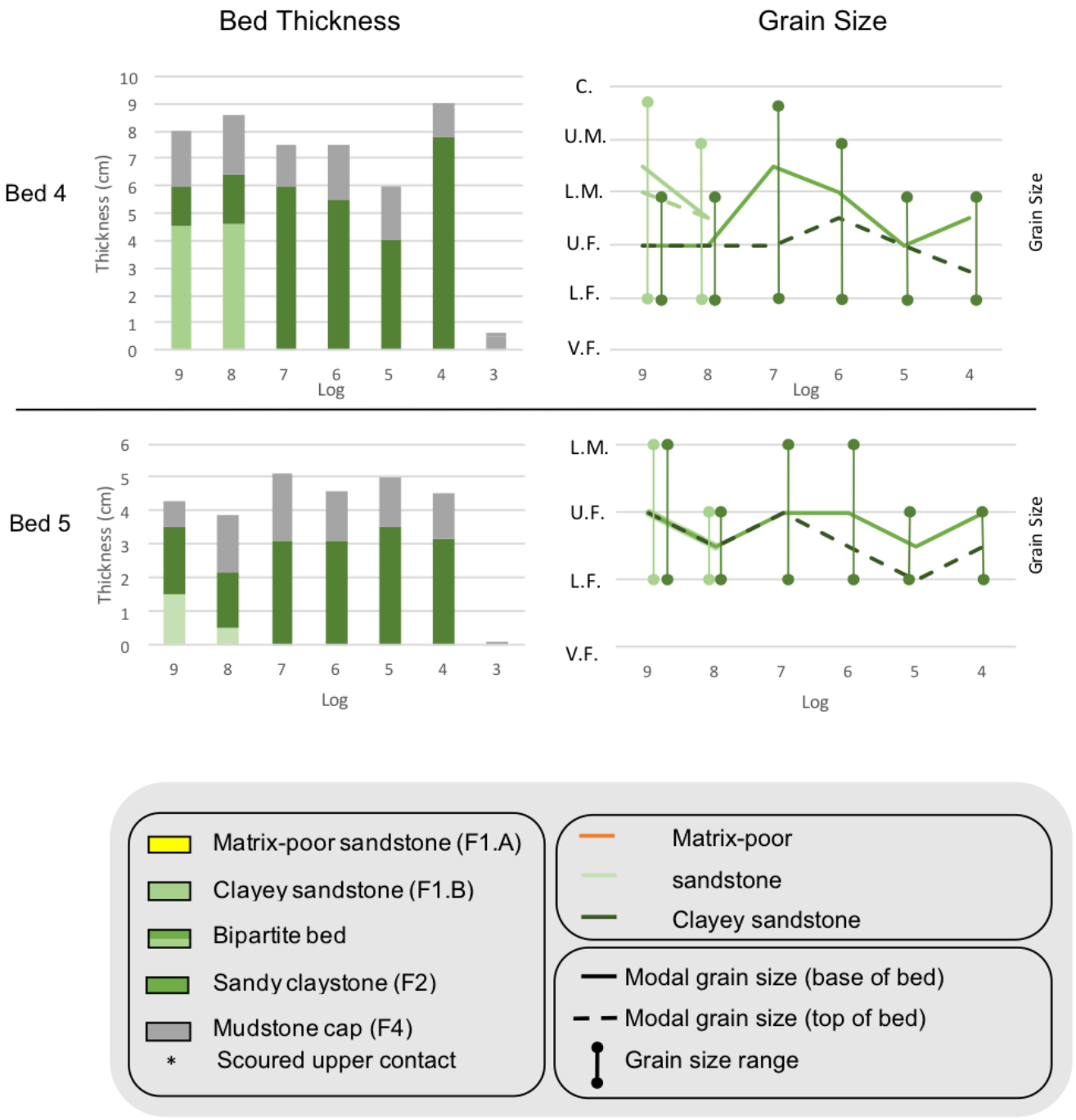

Figure 4-5. Caption on next page.

Figure 4-5 Graphs showing bed thickness and modal grain size from five different beds. Grain size measurements used in graphs were collected from outcrop descriptions using a 16X hand-held magnifying lens. Note the progressive lateral decrease in modal grain size from the sand-rich to mud-rich part of the transect. However, the range of grain sizes changes little, an exception being granules, which are absent in the most mud-rich (distal) parts of the transect. Although not observed in the field, and therefore absent from the graphs, are dispersed coarse to very coarse grains in sandy claystone – observed only in thin section (V.F. = very fine sand, L.F.= lower fine sand, U.F.= upper fine sand, L.M= lower medium sand, U.M. = upper medium sand, C.= coarse sand, V.C. = very coarse sand, G. = granules).

4.1.3 Thickness

Overall, there is a general lateral thinning from the sand-rich proximal part of the transect toward the mud-rich distal part (Figure 4-5). Beds of F1.A are typically medium- to thick-bedded (~20 cm - 1 m). Laterally, bed thickness decreases to thin- to thick-bedded (~10 - 40 cm) clayey sandstones that then progressively thin in the basal part of a now-developed bipartite bed (~5-20 cm). Further laterally the basal clayey sandstone continues to thin whereas the upper sandy claystone gradually thickens. Also, the bipartite bed will either gradually thin or change little until the basal clayey sandstone pinches out. From here the now exclusively sandy claystone is typically thin- to medium-bedded (~3-15 cm) and changes little in thickness laterally, but then eventually thins and pinches out. Finally, the overlying traction-structured sandstone and mud cap drapes the entire lateral facies association. Collectively the traction-structured sandstone and claystone cap are typically <2 cm in thickness and change negligibly over the length of the transect.

4.1.4 Lateral Dimensions

As previously mentioned, the outcrop is most probably oriented somewhat oblique to the true flow-parallel facies trend. Here, the lateral dimensions of the facies transitions are reported with the shortest lateral dimension for each of the various observed facies changes, and therefore the most flow–parallel orientation.

Due to cover, the lateral extent of the sandstone (F1.A) part of the transect was never observed. The clayey sandstone (F1.B) taken from its initial transition from a sandstone (F1.A) to its occurrence at the base of a bipartite bed, ranges between ~90-120 m. The bipartite part of the lateral transect, which extends from where the bed develops an upper sandy claystone (F2) to where the basal clayey sandstone (F1.B) pinches out ranges between ~60-120 m in the horizontal dimension. The sandy claystone (F2) part of the transect, which occurs between the termination of the basal clayey sandstone of the bipartite bed to the pinch out of the exclusively sandy claystone, ranges between ~60-180 m in the horizontal dimension. Overlying the entire transect is a traction-structured sandstone (F3.B) and claystone cap (F4) that extend beyond the pinch out point of the underlying sandy claystone sandstone, but was not measured in this study. Collectively, therefore, the entire hypothetical transition would occur over a lateral distance of a few hundreds of metres.

4.1.5 Basal Contacts

Basal contacts over the entire transect show a systematic change from scoured and loaded basal contacts in the sandy part of the transect to distinctively sharper, more planar based contacts laterally. The sandstone and clayey sandstones have scour to wavy bases, although the depth of incision is shallower in the latter. Bipartite beds generally have sharp, planar contacts, as do sandy claystones.

4.2 Lateral Facies Association Interpretation

Deposition of the previously discussed lateral succession of lithofacies is interpreted to result from particle settling in a mud-sand suspension undergoing negligible shear. In order to provide some theoretical background, a short discussion of particle settling from non-cohesive and cohesive particle suspensions will first be discussed.

4.2.1 Settling Behaviour of Non-Cohesive Particles

4.2.1.1 Sedimentation Behaviour of a Single Non-Cohesive Particle

In a low Reynolds number viscous fluid (Re<0.4), a non-cohesive particle's sedimentation behaviour is described by Stokes settling law, where the terminal velocity of a single rigid sphere can be determined by equating the viscous drag force to the submerged weight of the particle:

$$u = \frac{d^2(\rho_s - \rho)g}{18\mu}$$

where u is the terminal settling velocity of the sphere, d is radius, ρ_s is density, ρ is the fluid density, μ the fluid viscosity, and g is the acceleration due to gravity. At low Reynolds numbers (Re<0.4) flow remains attached to the surface of the particle and viscous forces are dominant. However, as Reynolds number increases, inertial forces become increasingly important as the flow tends to become detached from the solid surface, causing flow separation and a wake to develop on the downflow side of the particle (Figure 4-6). Flow separation thereby reduces skin friction and increases the importance of pressure drag, which changes with increasing Reynolds number (Chien and Wan 1999). Stokes law, however, neglects the importance of fluid inertia. Therefore, for Stokes law to apply in a natural setting particles will have a limiting diameter of 0.14 mm (Rubey 1933). Larger grains, therefore, will settle faster as inertial forces become progressively more significant. Hence, Stokes law is not appropriate for estimating the settling velocity of sand and coarser grains in natural systems (Rubey 1933).

For Reynolds numbers between 0.4 and 10^3, both fluid inertial and viscous forces are important. Under these conditions, large oscillating Kármán vortices are produced on the downflow side of the particle, which reduces skin friction, but produces significant pressure drag (Smits 2000). Between a Reynolds number of 10^3 and 2×10^5 viscous forces are negligible and the fall velocity of a sphere depends largely on pressure drag. In this range of Reynolds number, turbulent eddies separate continuously on the downflow side of the particle, thereby decreasing the particle's coefficient of drag (Chien and Wan 1999). As Reynolds number exceeds 2×10^5, the boundary layer changes from laminar to turbulent. Because turbulence is a more effective process for mixing compared to laminar flow, momentum exchange near the particle's surface is increased, which then decreases the adverse pressure gradient and moves the separation point

(point where flow separates from the particle surface) further downstream, and in turn, reduces the size of the wake and the overall drag force on the particle (Smits 2000). Moreover, if the particle's surface is sufficiently rough, flow near the surface of the particle will more readily develop a turbulent boundary layer, which for reasons previously discussed will decrease the particles drag force (Chien and Wan 1999).

Shape and orientation of a settling particle will also modify a particle's sedimentation behaviour. Specifically, changing the orientation of the particle will affect the area that is normal to the direction of fall (Chien and Wan 1999). Furthermore, if flow separates from a particle, the location of the point of separation and the size of the wake also depends on the particle shape. That is, for bluff shaped particles the coefficient of drag is greater compared to streamlined particles (Chien and Wan 1999).

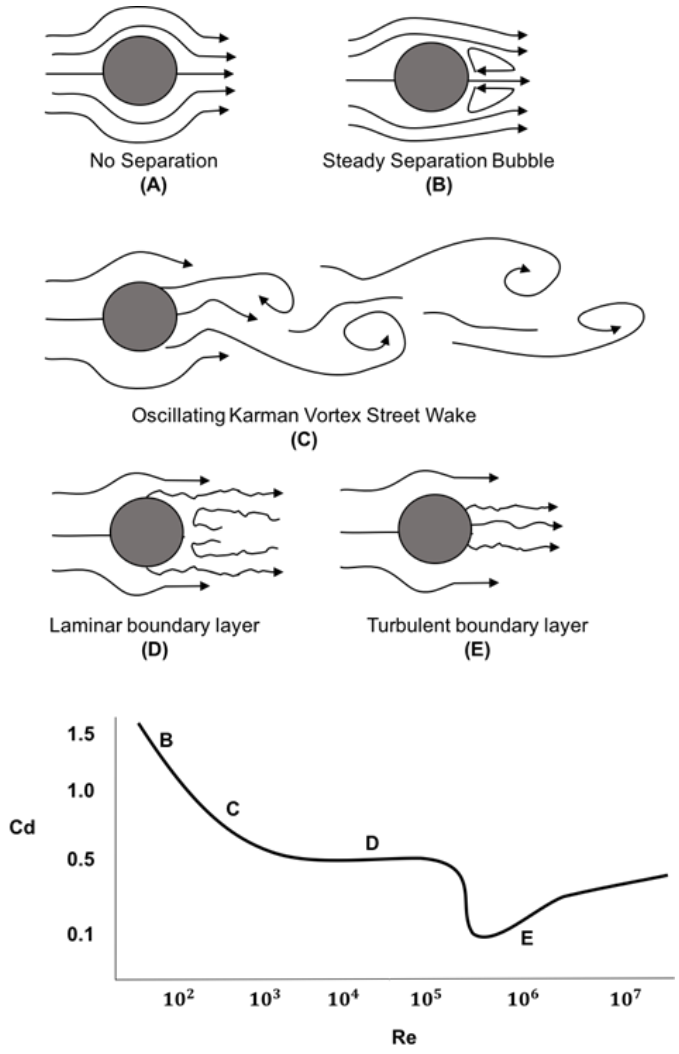

Figure 4-6 Characteristics of flow past a smooth blunt body (modified from Spurk and Aksel, 2008). **Top** – schematic of flow patterns around a spherical particle, and plotted as a function of fluid drag (Cd) and Reynolds number (Re). At low Reynolds number Re<0.4, **(A)** there is no flow separation and therefore no viscous wake downstream of the particle occurs. Note A) corresponds to Reynolds of about <0.4 with a fluid drag of drag of >10 and therefore is absent from the accompany graph. With increasing Reynolds number **(B)** a steady separation bubble forms with a pair of stable vortices. Flow has now separated and the vortices generated impart a high drag on the particle. At Reynolds number of $\sim 10^4$ **(C)** Oscillating Karman Vortex Street Wakes form. Downstream vortices progress and begin to separate on alternating sides of the body. The wake is wide and therefore the drag high. **D)** Laminar boundary layer with a chaotic wake downstream of the particle. **E)** boundary layer becomes turbulent with vortices of many different scales being shed from the body. In addition, the separation point moves further away, thereby reducing the size of the separation bubble and therefore drag on the particle.

4.2.1.2 Sedimentation Behaviour of a Non-Cohesive Particle Suspension

At low concentrations, typically a few percent or less by volume, grains are so widely spaced that grain-to-grain interactions are negligible and particles settle independently of each other and according to their size, density, and shape. Therefore, under these conditions, a polydispersed suspension containing n discrete particle sizes, with the same density and shape, will develop n layers during sedimentation. Each region is segregated by their relative fall velocities, where the fastest settling particles accumulate first, followed by the second fastest region of and so on until the slowest settling particle region settles last (Davies, 1988). As a result of their relative settling velocities, deposits of polydispersive suspensions are graded and well sorted (Amy et al. 2006).

As particle concentration increases up to a critical concentration of about 30-60% by volume, settling behaviour becomes altered by hindered settling effects (Davies 1968, Druitt 1995). Under these conditions, settling particles create an upward return flow of ambient fluid due to volume conservation (Davies 1968). The return flow then imparts an upward drag force on the (settling) particle and as a consequence 'hinders' its settling. At the same time sufficiently small particles may be transported upward with the return flow thereby increasing the density and hence buoyancy effects of the fluid, and further decreasing settling velocity (Davies 1968, Amy et al. 2006). Furthermore, hindered settling is greatest where particle size and/or density contrast is large and concentration is high (Davies 1968).

Richardson and Zaki (1954) formulated an empirical settling equation that accommodated for the effects of hindered settling effects:

$$u^o = u(1-c)^{n-1}$$

where u^o is the observed or hindered settling velocity, c is the concentration of the suspension, and n is the model exponent, which under turbulent conditions (Reynolds number >500) was reported to be 2.39. Moreover, Richardson and Zaki (1954) showed that particle concentration and sedimentation rate were inversely related; specifically, sand particles in highly concentrated suspensions will settle more slowly compared to the same grains in a lower concentrated suspension.

Beyond a critical concentration of about 30-60% by volume, particle segregation is progressively hindered and eventually suppressed as grains interlock, or by hydrodynamic effects, resulting in an unsorted massive deposit (Davies 1968, Lockett and Al-Habbooby 1974, Amy et al. 2006). In the case of grain interlocking, Davies (1968) suggested that at the critical concentration, the space between particles becomes smaller than the diameter of the particles causing grains to become geometrically trapped in a network of grains. Alternatively, Richardson and Zaki's (1954) hindered settling equation demonstrates that beyond a critical concentration, hydrodynamic effects, like the return flow of ambient fluid, may suppress complete grain segregation. Later experimental work by Lockett and Al-Habbooby (1974) showed that beyond a concentration of 40% by volume, a bimodal suspension containing particles of the same size and shape, but different densities, will settle together, or what is termed batch settling. Because the bimodal suspension consisted of particles with the same size and shape, hindered settling effects related to grain size differences, such as grain interlocking, can be excluded and attributed to hydrodynamic effects (Lockett and Al-Habbooby 1974). Moreover, Lockett and Al-Habbooby (1974) demonstrated that the critical concentration for batch settling was dependent on the proportion of grain sizes in a bimodal suspension; particularly, an increase in the proportion of fines increases the critical concentration for batch settling. Nevertheless, both models, that being

geometric grain interlocking and hydrodynamic principles, may influence batch settling (Lockett and Al-Habbooby 1974).

More recently, Dorrell and Hogg (2010) and Dorrell et al. (2011) proposed a theoretical depositional model based on non-cohesive bi-dispersed and polydispersed suspensions. This work was then extended to explain the experimental settling results of Amy et al. (2006), in which a basal massive deposit overlain by a well sorted, graded deposit. Dorrel et al. (2011) showed quantitatively that the ungraded basal part of the deposit was the result of a constant mass flux of particles from a polydispersed suspension. Here, despite different size particles settling at different velocities, the mass flux of sediment into the deposit remained constant and made up of the same grain size distribution as in the initial suspension (i.e. “n” particles) (Figure 4-7). However, with time the largest grains become depleted and the deposit becomes populated by n-1 particles, and so on until only the finer particles remain in suspension, and therefore deposited at the top of the deposit.

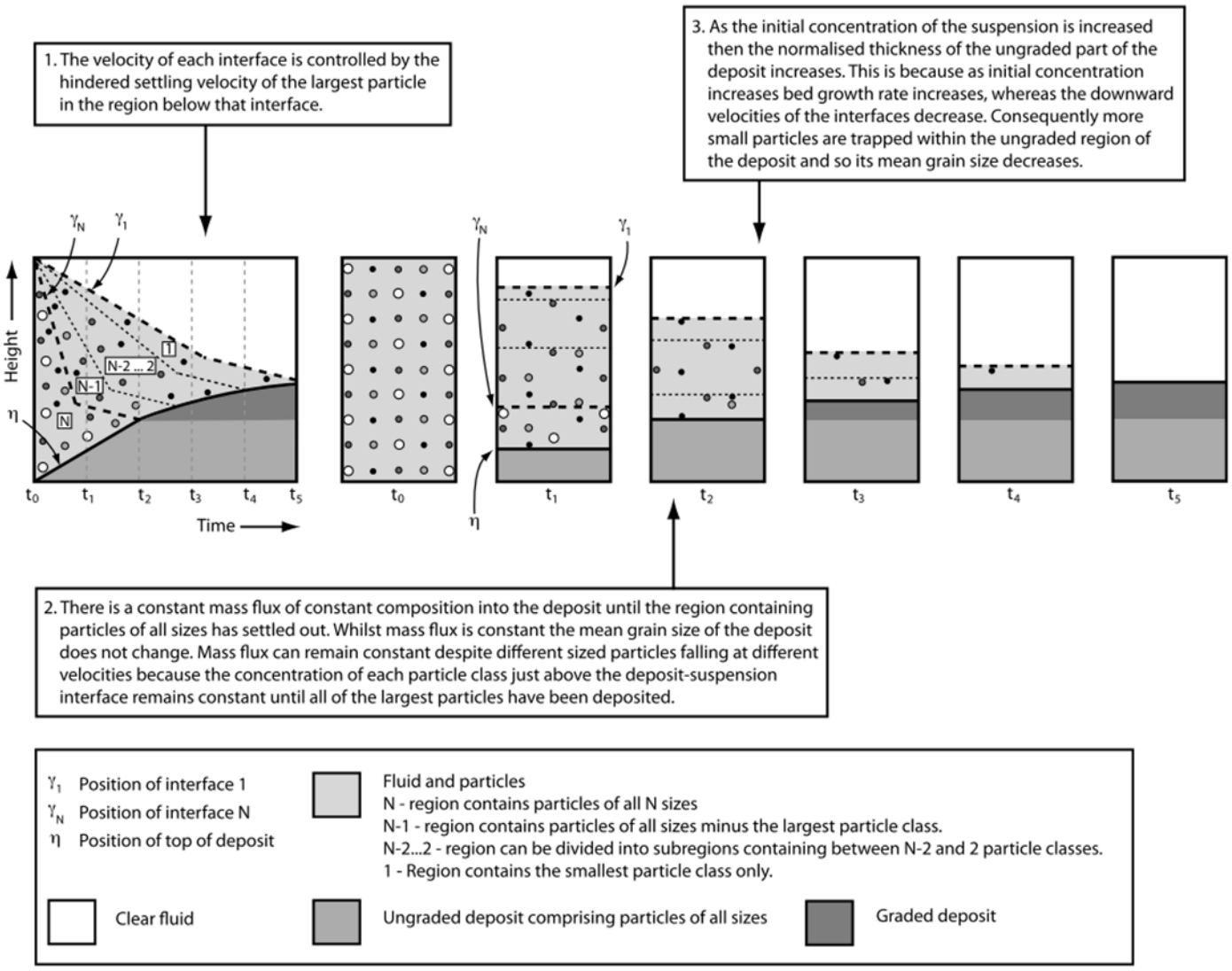

Figure 4-7 Temporal settling behaviour and depositional patterns from a polydisperse (particle) suspension (from Dorrell et al. 2011). The initially well-mixed suspension beings to develop into N+2 layers; the deposit at the bottom, N layers composed of particles, and a layer of clear fluid above. Importantly, the settling velocity of each N layer is controlled by the hindered settling velocity of the largest particle in the region below that interface.

4.2.2 Settling Behaviour of Cohesive Particles

The crystal lattice of a clay mineral consists of one or two silicon tetrahedral sheets and one octahedral alumina or magnesium sheet. However, due to the isomorphous substitution of Al for Si in the tetrahedral or Mg for Al in the octahedral, the clay mineral acquires a net negative charge on the face of the mineral (Van Olphen 1964). Consequently, cations and water molecules will be absorbed onto the exterior surfaces of the clay mineral due to their electrostatic attraction (Van Olphen 1964). As a result, water molecules and cations will form a tight arrangement on the surface of the clay mineral called an adsorbed layer. The greater the distance from the clay mineral, the lesser the attraction (Chien and Wan 1999). Therefore, water molecules further from the particle will only be slightly attracted. This region is called the diffuse layer. Water molecules that are outside the diffuse layer are unaffected by the static electric attraction and continue to move freely in what is called the free water region (Chien and Wan 1999). If two clay minerals are sufficiently close they may share a common adsorbed water and diffusion layer and therefore link together because of the attraction of ions with opposite charges and form aggregates that share a common face with neighbouring clay minerals. The processes by which clay minerals become linked face-to-face is termed aggradation; by analogy, the clay particles create a deck-of-cards framework (Van Olphen 1964).

Additionally, due to lattice imperfections at the edges of the clay minerals, specifically where Si is substituted by Al, there may be a positive double water layer at the edges of broken silica sheets. As a result, clay minerals may carry a positive double water layer despite an overall negative charge (Van Olphen 1964). Clay minerals may then join at their positively charged edges, or at the faces of other clay minerals. The preferential association of clay minerals from

edge-to-edge and edge-to-face is termed flocculation and can create a house-of cards-framework of clay mineral particles (Van Olphen 1964).

In terms of their settling behaviour, and at low concentrations, clay size clay mineral particles will settle according to their settling velocities. However, in high concentrations, collision rates increase, thereby increasing the potential for clay particles to adjoin to neighbouring clay particles (McAnally et al. 2007). Progressive flocculation and aggradation increases the aggregated clay particle size and thus fall velocity. Fluid turbulence may also enhance aggregation by increasing collision rates, but if too intense can break up the delicate clay aggregates (McAnally et al. 2007).

Continued particle growth eventually leads to gelling where clay particles create a volume-filling network. At this point the suspension develops sufficient viscosity to impart strength to the suspension, which then impedes the settling of all particles (Berlamont et al. 1993, Amy et al. 2006). In addition, buoyancy effects increase and further reduces or may arrest the settling of suspended sediments (Berlamont et al. 1993).

4.2.3 Interpretation of the Lateral Facies Succession

Previous studies at Castle Creek (Terlaky 2014, Terlaky and Arnott 2014) have reported that matrix-rich sandstones typically underlie base of slope channels, basin-floor terminal splays and distributary channels. This association suggests that the deposition of matrix-rich sandstones is related to the local activation of the system, most likely due to an upflow avulsion of an up-dip channel (Terlaky and Arnott 2014). Upon exiting the channel, highly energetic flows likely scoured the mud-rich seabed and engorged the through-going turbidity currents with fine-grain sediment (Terlaky and Arnott 2014). Additionally, the common occurrence of delicately

interlaminated silt and mudstone clasts suggests local erosion and only short distance transport (Terlaky and Arnott 2014). Also, the scour based contact of most matrix-poor sandstone beds in the proximal part of the transect indicates that turbulent eddies eroded the seafloor.

Initially, the upward component of fluid turbulence was the predominant sediment support mechanism. However, the presence of granules in matrix-poor sandstones suggests turbulence was not the only sediment support mechanism. Rather, a combination of mechanisms, including hindered settling, buoyancy and dispersive pressure, may also have contributed (Mulder and Alexander 2001). Still, intense turbulent mixing formed a more or less uniformly-mixed suspension in which particles independently settled according to their relative fall velocities, which generally equated to their grain size and resulted in the deposition of a normally graded matrix-poor sandstone (F1.A). Moreover, due to the constant downward mass flux of particles from the suspension to the bed, the composition of the matrix-poor sandstone is thought to be roughly equivalent to the composition of the initial suspension (e.g. Dorrell et al. 2011).

As the suspension continued to move and wane laterally away from the margin of the main jet flow, faster settling particles, such as granules to coarse sand particles, became preferentially depleted from the suspension as they were lost to the bed via deposition. This, in conjunction with the gradual lateral increase in the proportion of fine particles and matrix, as well as the absence of angular bedforms, infers that the dominate depositional mechanism was principally particle settling under high sediment fallout rates in a negligibly sheared suspension. The absence of angular bedforms in matrix-poor sandstones and clayey sandstones suggests the transport distance of individual particles along the bed was minimized, possible due to high sediment fallout rates and rapid bed aggradation (Arnott and Hand 1989).

The progressive transition from normally-graded matrix-poor sandstone to ungraded clayey sandstone at the base of a bipartite bed infers that the suspension rapidly lost sufficient fluid turbulence to keep the suspension adequately dispersed to enable particles to settle unhindered. Therefore, as the suspension progressively collapsed toward the bed, hindered settling effects became the primary sediment support mechanism, which enabled the suspension to laterally advect hundreds of metres away from the margins of the jet flow exiting the area of avulsion. Under these conditions, the deposition of clayey-sandstone (F1.B) most likely occurred under capacity-driven conditions, where particle segregation was partially hindered by the shear generated by escaping fluid, or by grain interlocking (Davies 1968, Lockett and Al-Habbooby 1974). However, further above the near-bed region, the constant downward mass flux of coarser particles caused ambient fluid to be displaced upward, initiating a return flow due to volume conservation (e.g. Dorrell et al. 2011). This return flow applied an upward drag force on particles and swept sufficiently fine grains, in this case mostly clay particles, upward, thereby increasing their concentration in the upper part of the suspension (e.g. Davies 1968).

The sharp, planar interface separating the basal clayey sandstone (F1 b) and the overlying sandy claystone (F2) in bipartite beds is inferred to delineate the level where cohesive clay particles became sufficiently abundant to form a pervasive network. At this point, the suspension was stratified with a basal sand-rich part and a more mud-rich upper part. Collectively, the two parts formed an overall plug-like flow, wherein turbulence and internal deformation were largely absent (Baas and Best 2002, Baas et al. 2011).

The significant proportion of matrix to grains, as well as the occurrence of floating very-coarse to coarse sand particles in the overlying mud-rich portion of the suspension, suggests that the dominate sediment support mechanism was most likely matrix strength (Mulder and

Alexander 2001). Additionally, the lateral increase in matrix content within the sandy-claystone part of the transect, suggests that as the suspension continued to travel, the proportion of clay particles progressively increased as the suspension continued to collapse. This is inferred to be the result of the continued segregation of fine-grained sediment into the upper part of the suspension, while at the same time coarse particles continually fell into the basal sand-rich part of the suspension. However, some coarse to very-coarse sand grains became stranded in the upper sandy claystone due to progressively increasing buoyancy and matrix strength effects in the upper mud-rich portion of the suspension that inhibited their ability to fall. Eventually the basal part of the suspension became completely depleted of sediment through deposition and the now exclusively mud-rich flow resembled a viscous plug flow (Baas and Best 2002, Baas et al. 2011). Further laterally, the entire mud-rich suspension thinned and similarly pinched out due to deposition.

From initiation to termination, the suspension was consistently overlain by a low-density turbidity current. As a result, the underlying deposit was reworked and deposited a very thin- to thin bedded Tcd turbidite (F3.A) that extends beyond the pinch out of the sandy-claystone (F2). Lastly, any clay that remained in suspension formed a near-bed fluid mud layer that eventually gelled depositing a claystone cap (F4) over the entire transect.

4.3 Vertical Facies Associations

Based on abrupt facies changes, three sharply bounded facies associations, or stratal assemblages (SA 1-3), are recognized. These are: intercalated matrix-poor and matrix-rich strata (i.e. clayey sandstone, bipartite beds, and sandy claystone) of stratal assemblage 1 (SA-1), exclusively matrix-rich strata (SA-2), and traction-structured turbidites (SA-3). The boundaries of stratal assemblages are associated with abrupt changes in stratal attributes, including grain size, texture, matrix percentage and bed thickness. Although SA-1 and SA-2 both contain matrix-rich strata, SA-2 consists of five or more stacked matrix-rich beds with no intervening matrix-poor sandstone. The classification, vertical trends and stacking patterns of these facies associations are discussed next.

4.3.1 Terminology

To provide better context in the following descriptions and discussion a hierarchical classification based on facies type and number of beds of a particular facies is constructed (See Table 4-1). At the smallest scale, beds consist of a single facies that are separated by abrupt changes in grain size or by a mudstone layer marking the top of the bed. Multiple beds then stacked to form a bedset. In this study two kinds of bedsets are recognized. The first consists of a dm- to m-thick, matrix-poor sandstone (F1.A) bed overlain sharply by one to four thin- to medium-bedded clayey sandstone, bipartite, or sandy claystone beds (Facies 1.B - 2). The matrix-poor sandstone is consistently thicker and coarser (modal grain size: coarse to medium sand) than the overlying matrix-rich strata (modal grain size: medium to fine sand). The second bedset consists of a stack of 5-20 thin- to medium-bedded clayey sandstone (F1.B), bipartite, or

sandy claystone (F2) beds. Typically, each bed is overlain by a thin-bedded, traction-structured sandstone (F3.A) capped with a claystone layer (F4). Bedset boundaries are abrupt and marked by a change in lithofacies. One or more bedsets then stack to form a stratal assemblage, which is the highest order element in the hierarchy (Figure 4-8).

Hierarchical Level	Components	Thickness
Bed	Facies	1 cm - 1 m
Bedset	Several beds and one or more lithofacies	10's of cm - 2 m
Stratal Assemblage	One or more bedsets	0.5 m - 6 m

Table 4-1. Hierarchy classification.

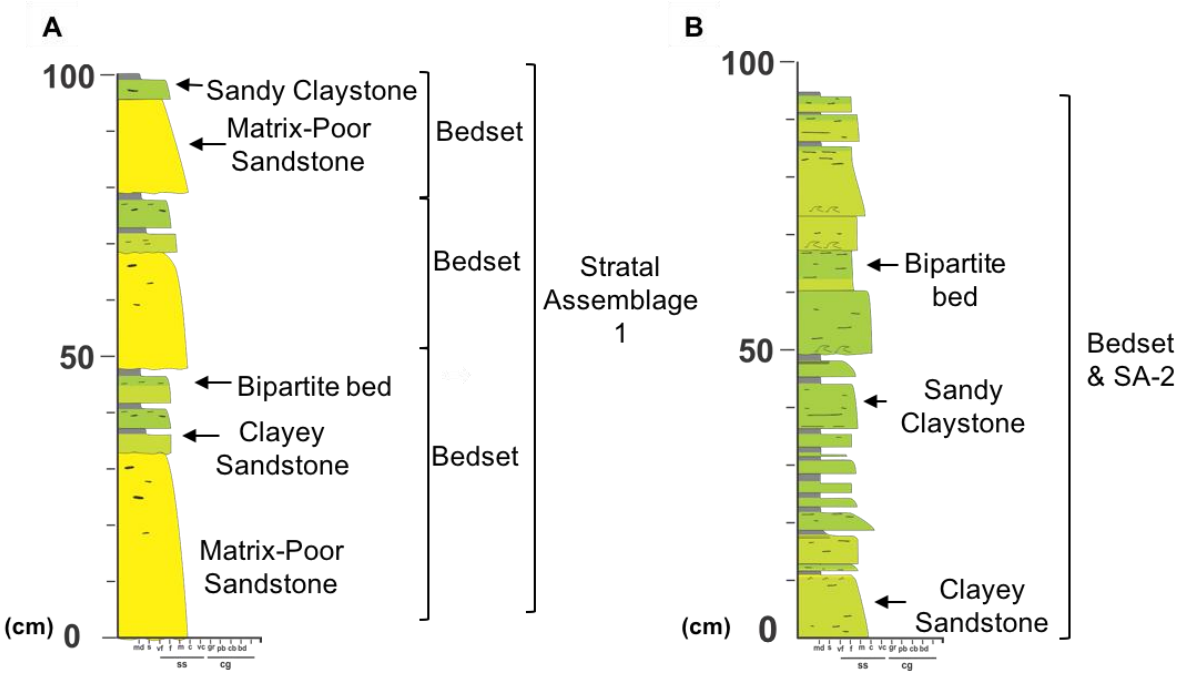

Figure 4-8 Schematic of stratal assemblages 1 (A) and 2 (B).

4.3.2 Stratal Assemblages

4.3.2.1 Stratal Assemblage 1: Intercalated Matrix-Rich and Matrix-Poor Strata

SA-1, which ranges from 1.5-4.5 m thick, comprises one to six bedsets, each consisting of a basal matrix-poor sandstone overlain by matrix-rich beds (Figure 4-9). In each bedset the matrix-poor sandstone thins and changes laterally into clayey sandstone and then a bipartite bed which, as described earlier in Chapter 4, indicates a lateral change to more distal deposition. Additionally, beds in the overlying matrix-rich part of the bedset are commonly partly or completely eroded by the matrix-poor sandstone at the base of an overlying bedset, and as a result the two matrix-poor sandstone beds amalgamate. However, where preserved, beds in the upper matrix-rich part of the bedset exhibit a similar trend to more distal facies laterally. At the stratal assemblage scale, stacked bedsets show negligible upward change in thickness or grain size.

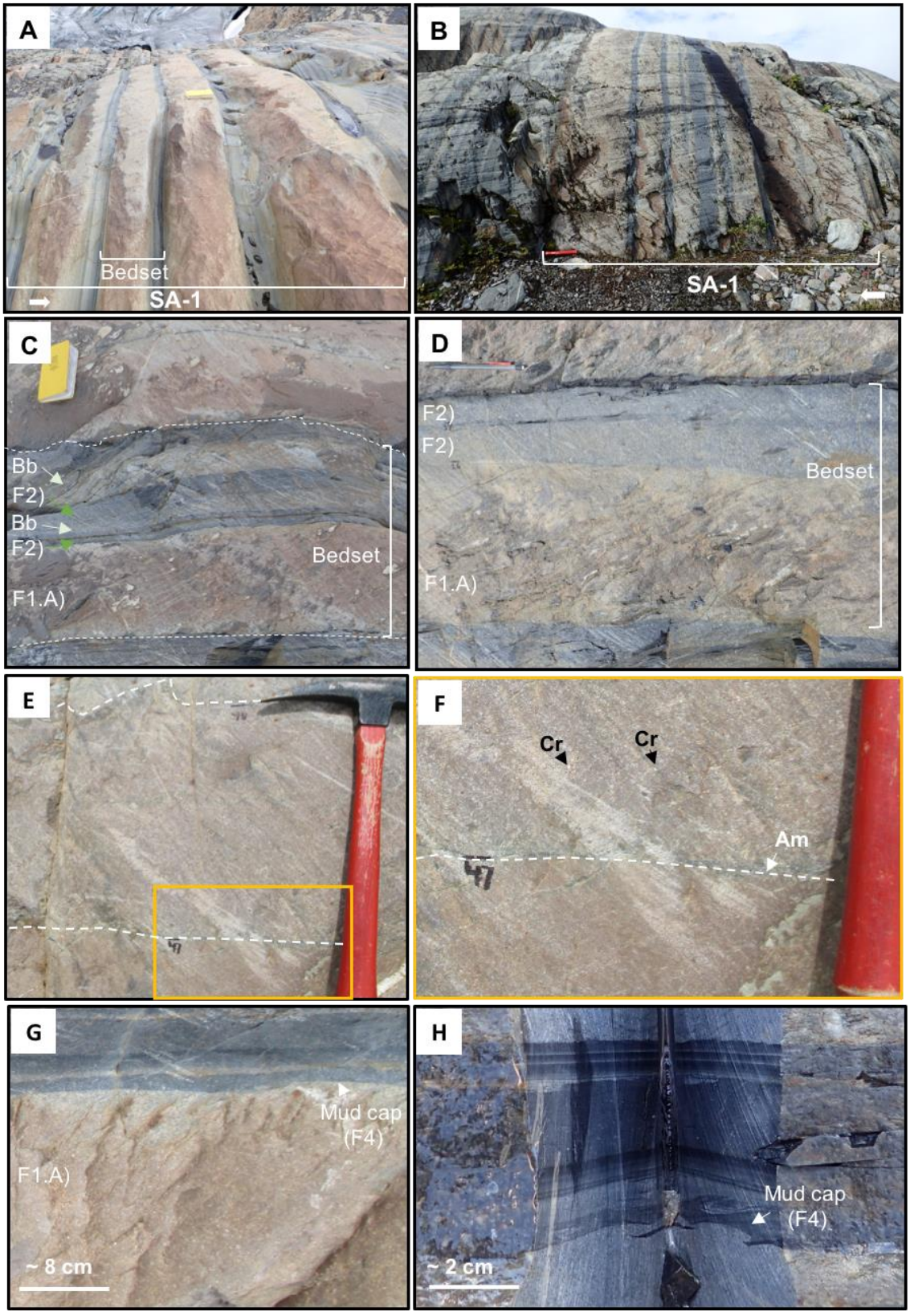

Figure 4-9. Caption on next page.

Figure 4-9 **A)** Photograph along depositional strike (facing SW) of multiple bedsets comprising a single stratal assemblage of intercalated matrix-rich and matrix-poor sandstone. A bedset is indicated by the **white bracket**. Multiple bedsets then stack to form a single stratal assemblage (SA-1). **B)** Photograph of a single (SA-1) stratal assemblage of intercalated matrix-poor and matrix-rich strata. Matrix-poor sandstones are tan-yellow with a subtle pink hue whereas matrix-rich strata are dark grey with a blue hue. Rock hammer for scale. **C)** Single bedset consisting of a basal (F1.A) matrix-poor sandstone overlain by (F2) clayey sandstones, and (Bb) bipartite beds. **D)** Single bedset consisting of a basal (F1.A) matrix-poor sandstone overlain by two (F2) clayey sandstones. **E)** Amalgamated matrix-poor sandstones. Amalgamation surface marked by white dashed line. Orange box indicates the location of photograph F). **F)** Amalgamation surface in (E) indicated by dashed line. Cr points to coarse to very coarse quartz grains. **G)** Photograph of a matrix-poor sandstone overlain by a mud cap (F4). **H)** outcrop photograph of a mud cap overlying a matrix-poor sandstone.

4.3.2.2 Stratal Assemblage 2: Matrix-Rich Strata

Stratal assemblage 2 ranges from 0.5-2 m thick and is composed of a single bedset of intercalated medium bedded, matrix-rich strata (clayey sandstone (F1b), bipartite beds, and sandy claystone (F2) (See Figure 4-10). Beds have characteristically flat bases with only rare scour or load structures and are a typically overlain by a thin-bedded traction-structured sandstone (F3.A) capped by claystone (F4). Within a single occurrence of stratal assemblage 2, beds show little upward change in thickness or modal grain size (medium or fine sand).

Significantly, successive beds within a single assemblage undergo a change in grain size, thickness and matrix percentage at about the same position laterally (Figure 4-11). As a result, each bed in an assemblage changes into progressively more distal facies and pinches out in the same direction (See Figure 4-12). The thin-bedded, traction-structured sandstone (F3.A) and claystone cap (F4) that overlie the matrix-rich strata, however, extend beyond the termination of the underlying matrix-rich part of the bed, and form a distinctively striped stack of alternating light and dark bands, that previously were termed “banded caps” by Angus (2016).

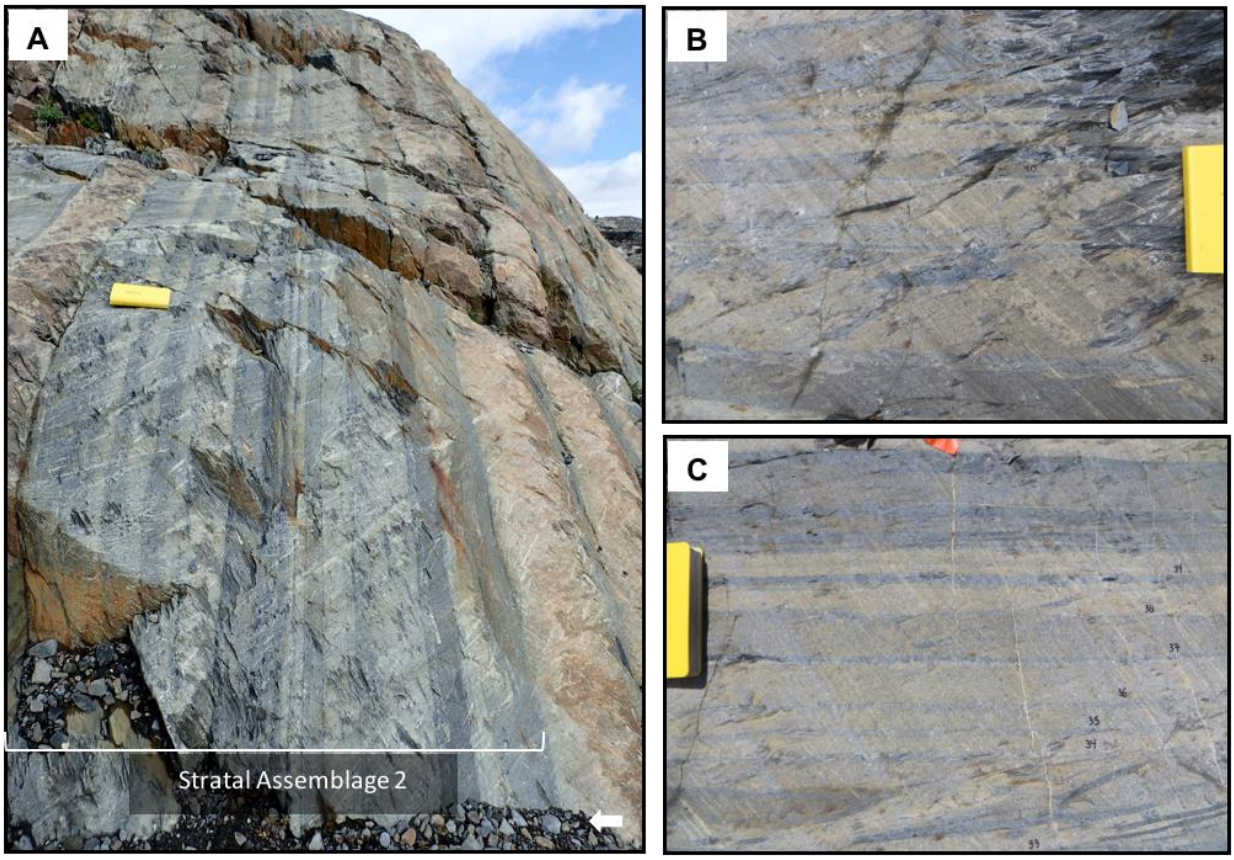

Figure 4-10 **A)** Outcrop photograph taken along depositional strike of stratal assemblage 2. Arrow indicating stratigraphic up. **B)** and **C)** Outcrop photographs of stratal assemblage 2 composed of ~15 matrix-rich beds (clayey sandstone, bipartite beds, and sandy claystone).

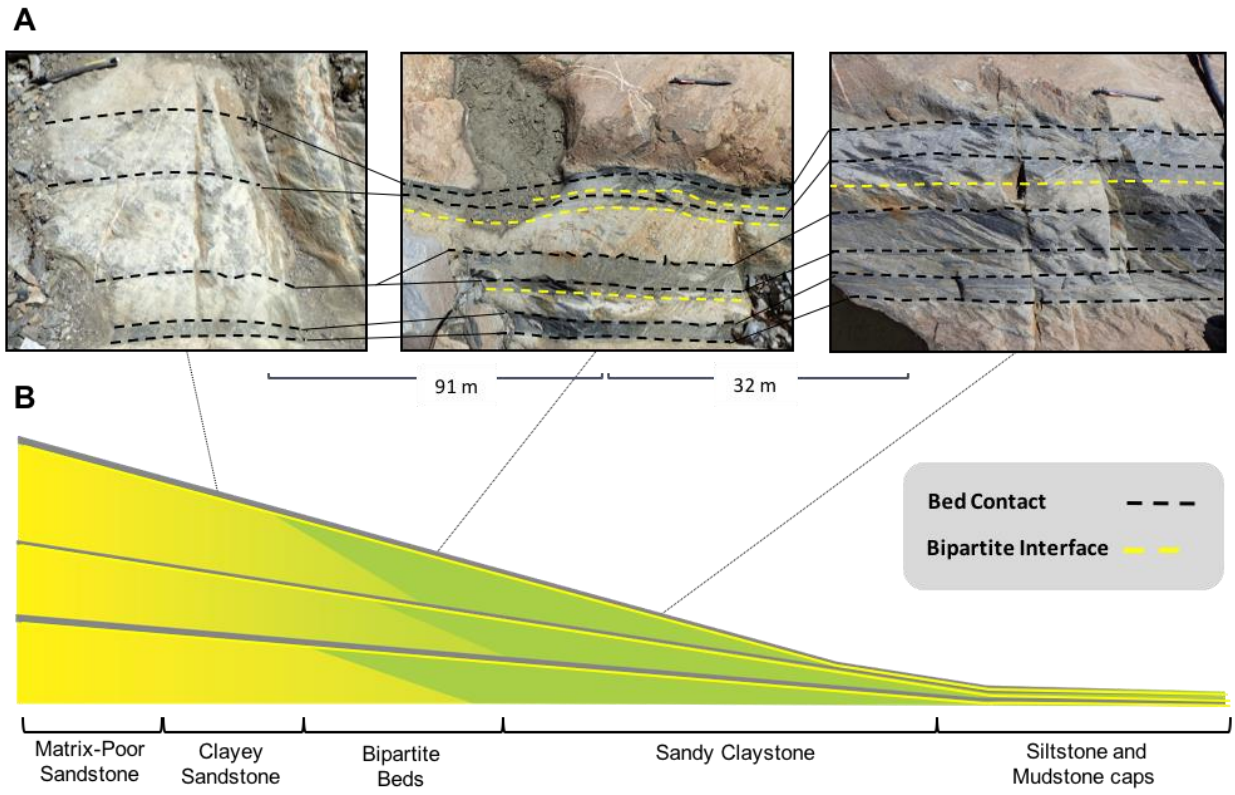

Figure 4-11. **A)** Correlated outcrop photographs illustrating the full lateral facies succession from sand-rich sandstone in the proximal part to matrix-rich sandy claystone more distally. Note that at the bedset scale facies change at about the same positon laterally. **B)** Schematic depicting the vertical stacking pattern of the lateral facies succession (not to scale).

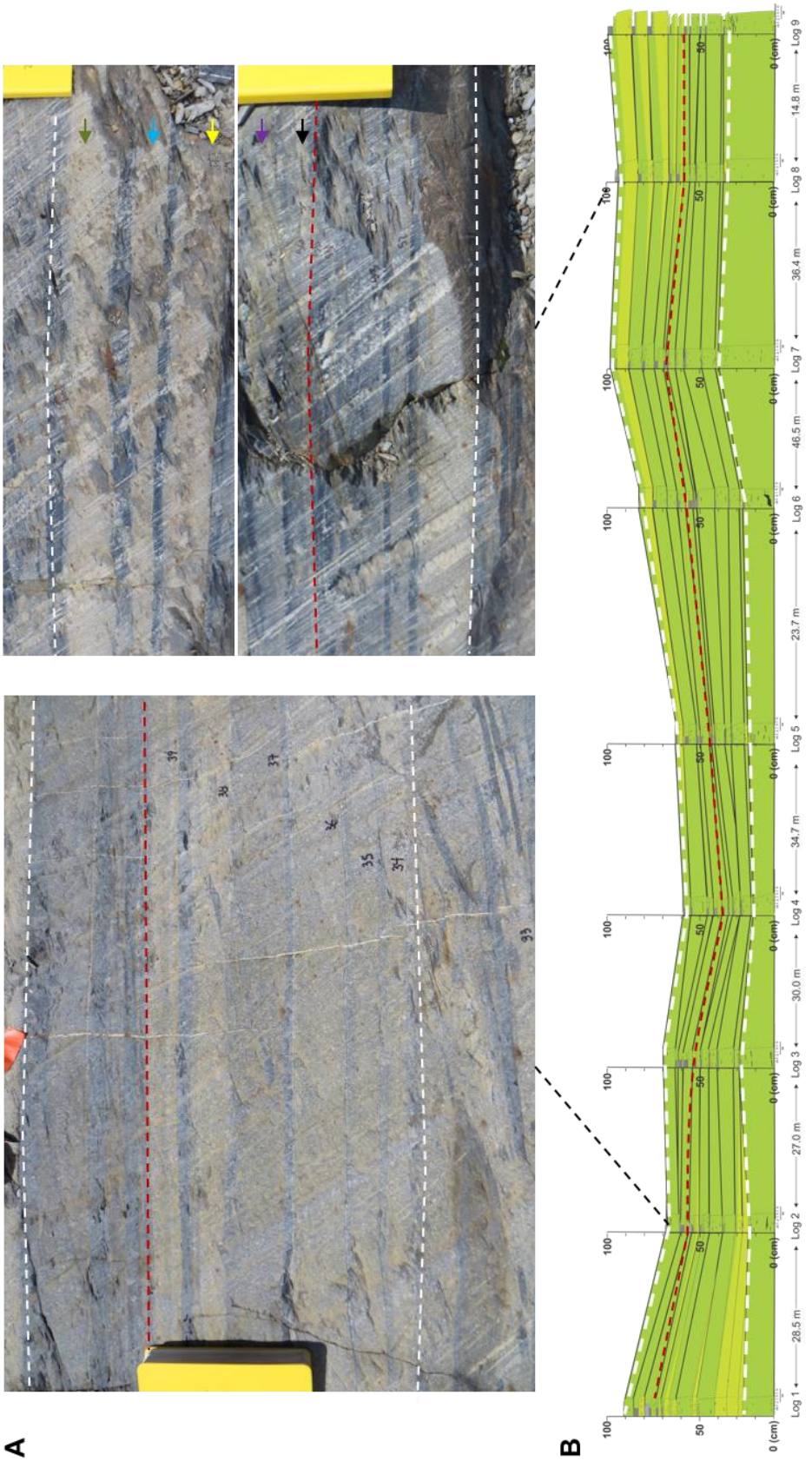
A
B
Log 1
28.5 m
Log 2
27.0 m
Log 3
30.0 m
Log 4
34.7 m
Log 5
23.7 m
Log 6
46.5 m
Log 7
36.4 m
Log 8
14.8 m
Log 9
0 (cm)
50
100

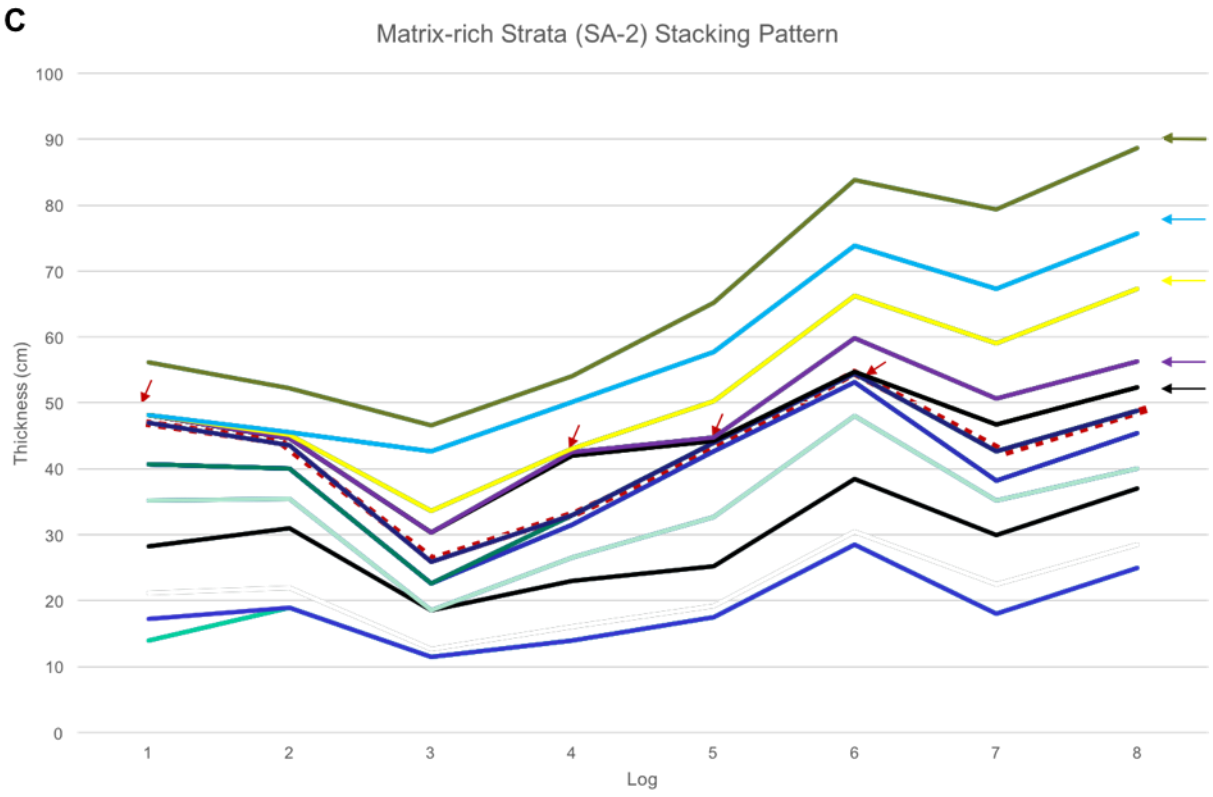

Figure 4-12 **A)** Outcrop photographs and **(B)** accompanying stratigraphic correlation panel of matrix-rich strata of SA-2. White and red dashed lines correspond to the red and white dashed lines in the correlation panel (B) and the red dashed line in (C). Notably, strata above the dashed red line show a pronounced thinning to the left. Coloured arrows in the photographs (A) correspond to the same strata used in the line diagram in (C). **C)** Bed thickness graph of individual beds in a single matrix-rich assemblage. **Red arrows** indicate the pinch out location of a bed.

4.3.2.3 Stratal Assemblage 3: Traction-Structured Turbidites

Stratal assemblage 3 consists of interbedded cm- to dm-thick, matrix-poor, traction-structured turbidites (Facies 3.B Tbd, Tbcd, and Tcd turbidites) that form a stack ranging from 1 – 6 m thick (Figure 4-13). At the bed scale, beds show no change in facies laterally and consist of Tbcd and Tbd turbidites interbedded with thin- to medium-bedded, multiset Tcd turbidites.

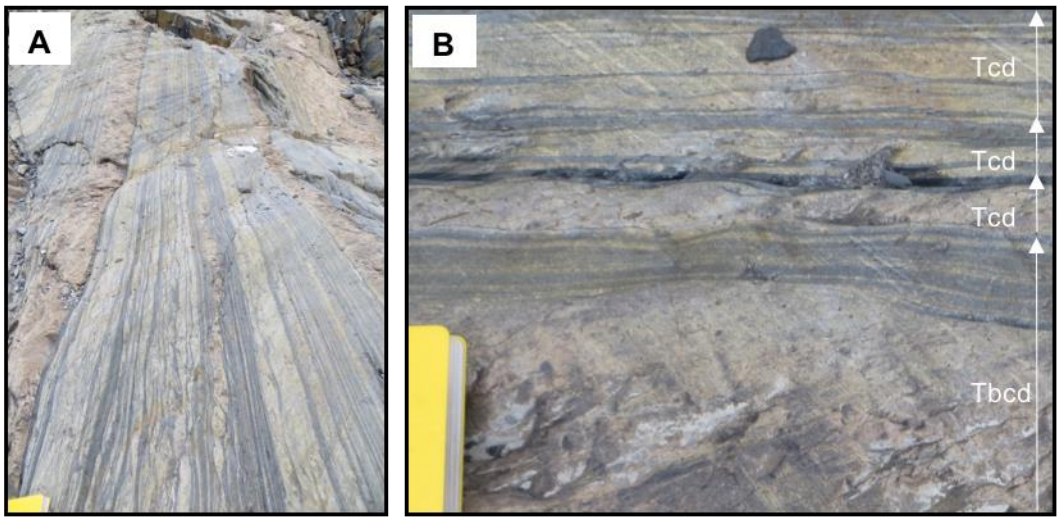

Figure 4-13 **A)** Outcrop photograph of stratal assemblage 3 consisting of Tbcd and Tbd turbidites. **B)** Photograph of Tbcd Tcd turbidites.

4.3.3 Stacking Patterns of Stratal-Assemblages

SA-1 alternates vertically with SA-2 whereas laterally they grade into one another and as a consequence form a wedge shape geometry (Figure 4-14). Moreover, intercalated successions of stacked SA-1 and SA-2 are sharply bounded by traction-structured turbidites of SA-3 (Figure 4-15).

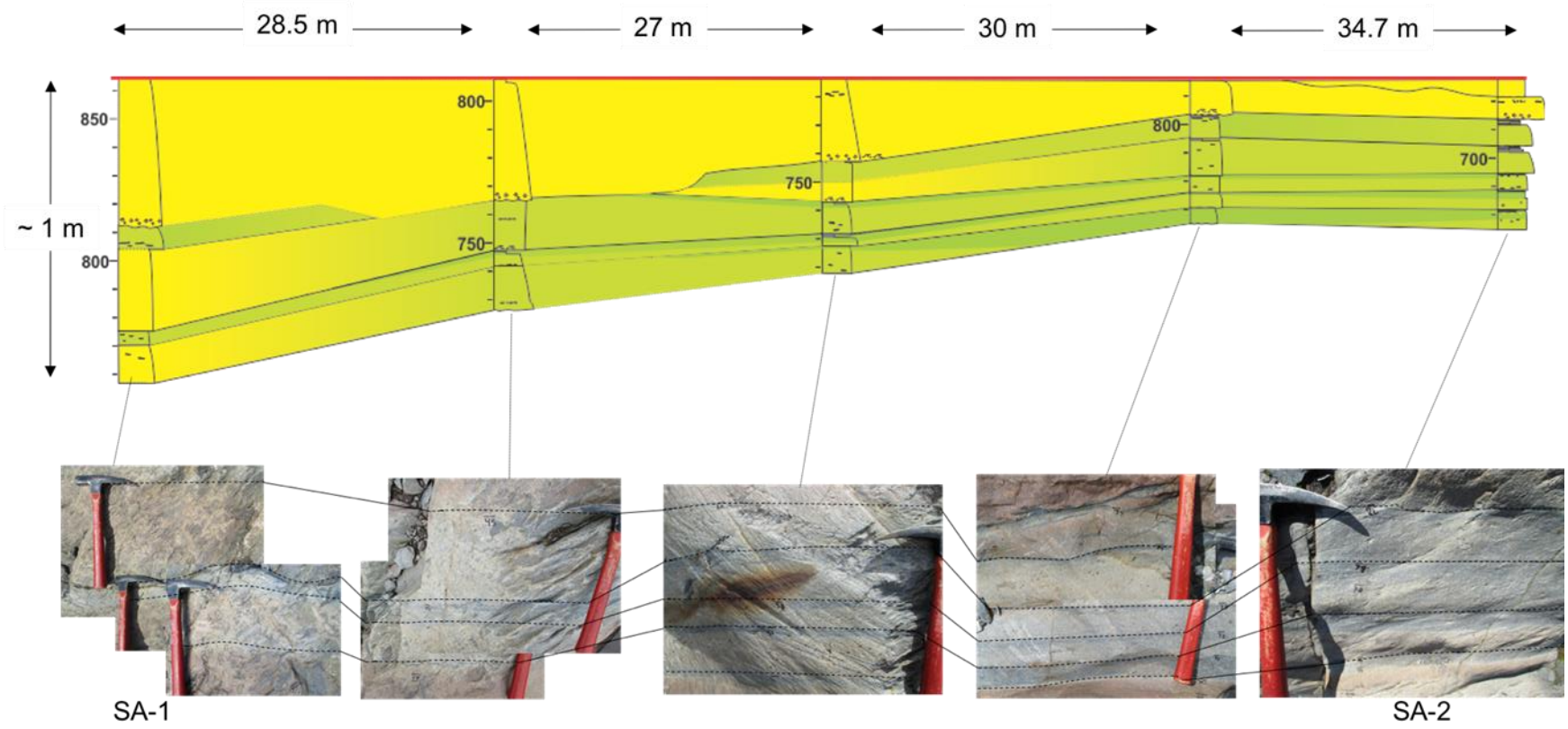

Figure 4-14 Stratigraphic correlation panel and accompanying outcrop photographs of intercalated matrix-rich and matrix-poor strata (SA-1) changing laterally into exclusively matrix-rich strata (SA-2). Blacks dashed lines denote bed contacts.

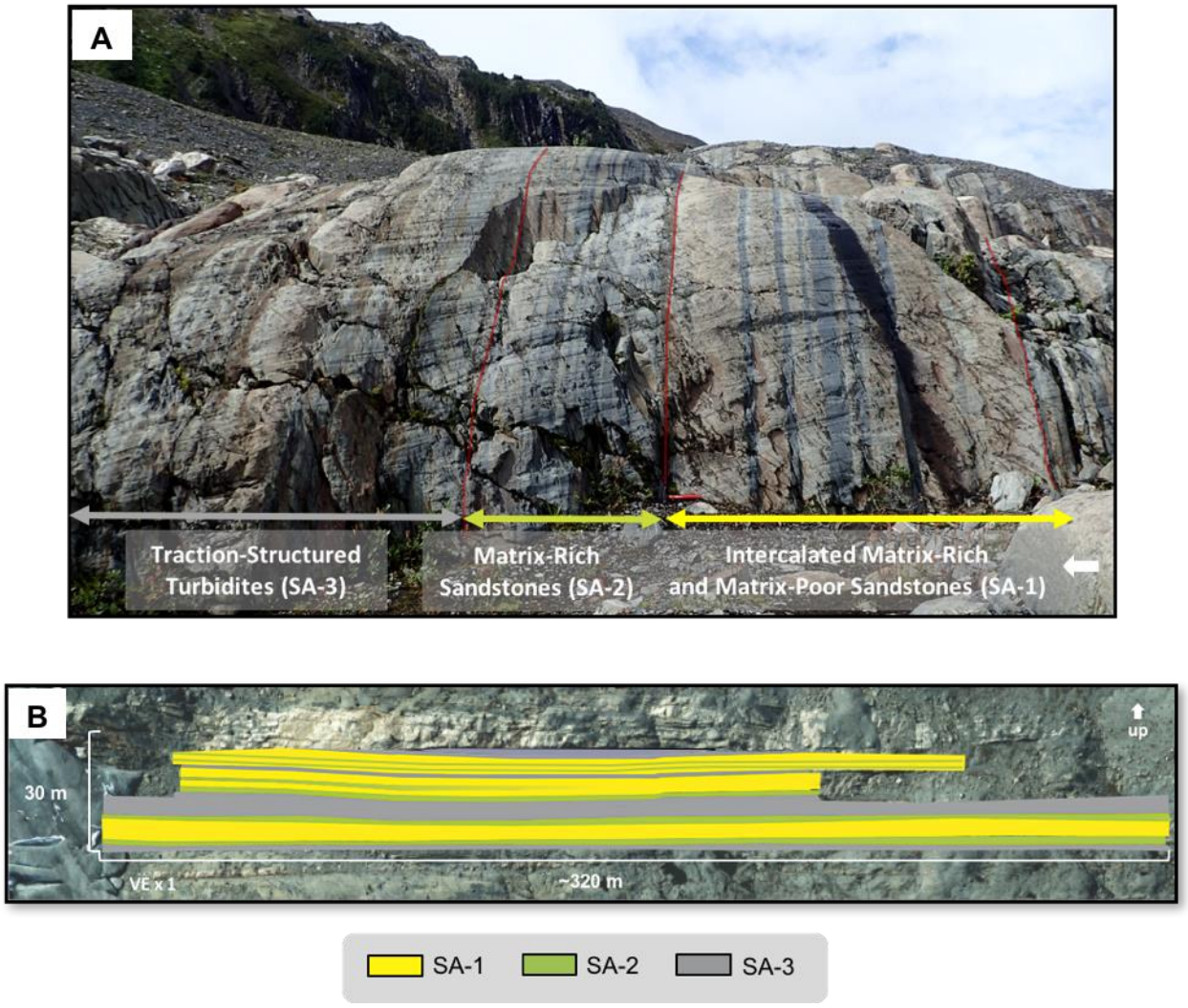

Figure 4-15 **A)** Depositional strike view of a stack of three sharply bounded stratal assemblages. Red lines indicate stratal assemblage boundaries. Rock hammer for scale. **B)** Correlation panel of stratal assemblages in the study area. Stratigraphically upwards SA-1 and SA-2 form a sharply bounded succession. Several metre-thick intervals of stacked SA-1 and SA-2 strata are sharply overlain by SA-3.

4.3.4 Markov Chain Introduction

To identify any statistical pattern in the vertical stacking of beds, a first order Markov chain analysis was conducted (e.g. Terlaky 2014). A Markov chain analysis is a mathematical procedure that describes the change of a system from one discrete state to another at a separate time, space, or any other discrete measurement interval (Schwarzacher 1975). The change from one state to the next is considered a transition and is assumed to depend only on the previous state; an assumption termed the Markov property (Schwarzacher 1975). The transition from one state to the next is assumed to be random and based on the transition probabilities. However, in natural sedimentary systems erosion can preferentially remove certain states, and therefore result in a bias that favours those with better preservation potential. Therefore, analyses, like this one, assume no erosion and that the vertical transitions observed in outcrop can be analyzed by a Markov chain analysis.

4.3.5 Markov Chain Analysis

In this study, a first order Markov chain analysis was conducted on five vertically-continuous stratigraphic logs to determine if the stacking arrangement of facies (i.e. states) exhibited a random or non-random pattern. Each log contained between 104 – 137 beds (i.e. transitions), with each bed made up of one of the four facies, specifically (F1.A) matrix-poor sandstone, (F1.B) clayey sandstone, bipartite bed, or (F2) sandy claystone. The vertical stacking of these facies was then used to construct the transitional matrix.

At the bed scale, thick- and thin-bedded turbidites (F3.B) were always followed by another turbidite. As a result, considering each turbidite as an individual state would skew the

results of the Markov chain analysis in favour of a statistically significant result. Therefore, turbidites were omitted from the analysis in order to better identify stacking patterns within SA-1 and SA-2 assemblages.

4.3.6 Markov Chain Results

Results of the observed and expected vertical transitions are summarized in FigureFigure 4-16. Matrix-poor sandstone (F1.A) comprise 30% of all beds (i.e. states) and are most frequently overlain by a similar matrix-poor sandstone (41% of observed transitions). Less commonly, matrix-poor sandstone is overlain by a sandy claystone (F2) (36%), clayey sandstone (F1.B) (12%) or bipartite bed (11%). Markov chain analysis indicates that matrix-poor sandstone is more commonly overlain by matrix-poor sandstone or clayey sandstone than expected in a random distribution. Additionally, matrix-poor sandstone is statistically less commonly overlain by bipartite bed or sandy claystone than expected.

A

Observed Transition Matrix - Counts					
From/To	F2	Bb	F1.B)	F1.A)	SUM
F2	123	42	17	57	239
Bb	32	24	11	30	97
F1.B)	23	10	10	11	54
F1.A)	60	19	20	68	167
					557

B

Expected Transition Matrix (for random distribution) - Counts					
From/To	F2	Bb	F1.B)	F1.A)	SUM
F2	102.6	41.6	23.2	71.7	239
Bb	41.6	16.9	9.4	29.1	97
F1.B)	23.2	9.4	5.2	16.2	54
F1.A)	71.7	29.1	16.2	50.1	167
					557

C

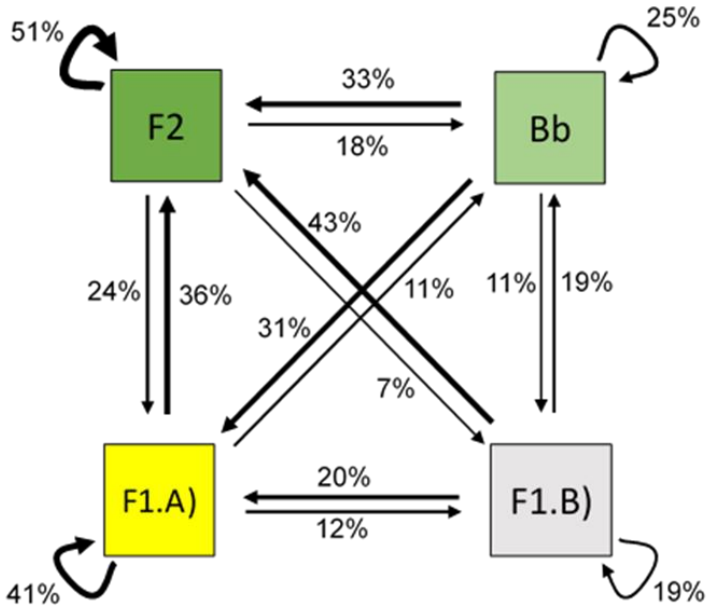

Figure 4-16. Caption on next page.

Figure 4-16 Markov chain analysis results through the study section. In total 557 transitions were used in the analysis. **A)** Observed transition matrix counts; F2 = sandy claystone, Bb = bipartite bed, F1.B = clayey sandstone, F1.A = matrix-poor sandstone. **B)** Expected counts matrix based on a random distribution. **C)** Transitional state diagram; thickness of arrow is proportional to its probability.

Clayey sandstone comprise 10% of all beds in the measured sections and is most frequently overlain by a sandy claystone (43% of observed transitions). However, Markov chain analysis indicates that this relationship is statistically random. Less commonly, a clayey sandstone is overlain by matrix-poor sandstone (20%), another clayey sandstone (19%) or a bipartite bed (19%). Significantly, however, Markov chain analysis indicates that clayey sandstone is statistically more commonly overlain by another sandy claystone. Additionally, a clayey sandstone is less commonly overlain by another matrix-poor sandstone than statistically expected.

Bipartite beds comprise 17% of all beds and are most commonly overlain by a sandy claystone (33%) or matrix-poor sandstone (31%). Less commonly are they overlain by another bipartite bed (25%) or clayey sandstone (11%). Markov chain analysis demonstrates that a bipartite bed is statistically more commonly overlain by another bipartite bed. Furthermore, a bipartite bed is less commonly overlain than expected by a sandy claystone. Additionally, a bipartite bed is randomly overlain by a clayey sandstone or matrix-poor sandstone.

Sandy claystone is the most common facies in the studied section, comprising 43% of all beds and most frequently overlain by another sandy claystone (51%). Less commonly a sandy claystone is overlain by a matrix-poor sandstone (24%), a bipartite bed (18%) or clayey sandstone (7%). Markov chain analysis indicates that sandy claystone is statistically more

commonly overlain by sandy claystone but less commonly by clayey sandstone or matrix-poor sandstone. Furthermore, sandy claystone overlain by a bipartite bed is random.

In general, the first-order Markov chain analysis used here indicates that like facies in addition to matrix-poor overlain by clayey sandstone, typically succeed one another; whereas all other transitions are less than expected or random. In addition, field observations indicate the common occurrence of 2 to 7 beds of similar facies stacked one above the other, which here are termed packages (Figure 4-17 and Figure 4-18). Additionally, within each package beds are similar in terms of lithology and thickness, the significance of which is discussed below (in the vertical stacking patterns interpretations 5.2).

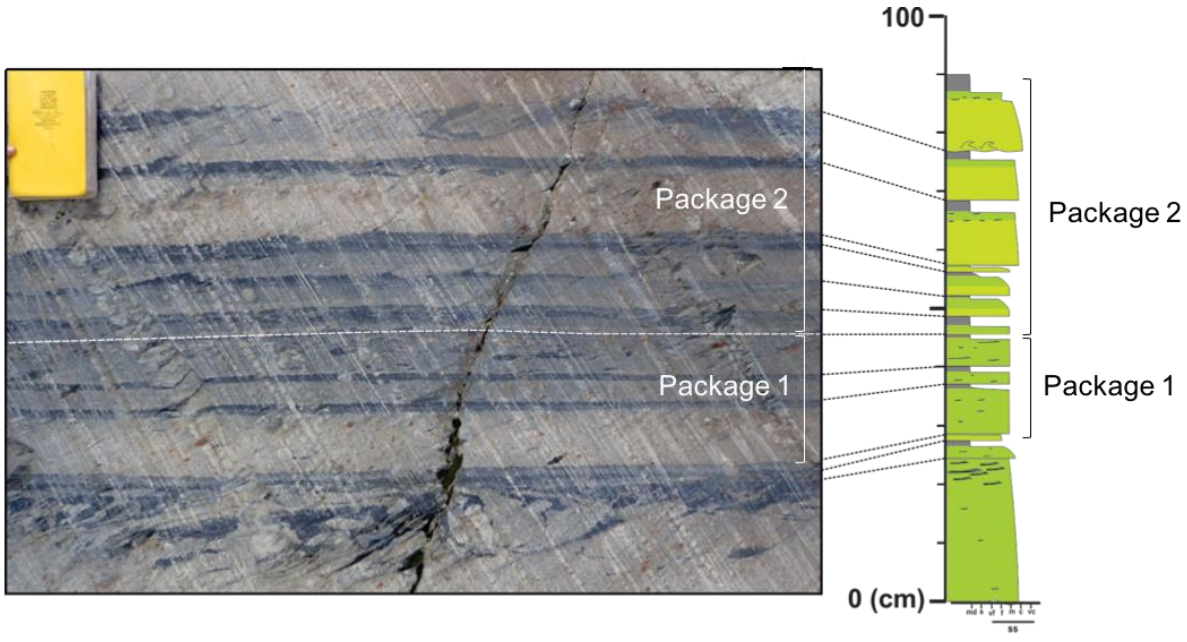

Figure 4-17. Outcrop photograph of two stacked packages (separated by white dashed line) with stratigraphic log on the right. Package 1 consists of stacked sandy claystone beds whereas Package 2 is made up of a stack of bipartite beds. Note the mudstone layer that caps each bed.

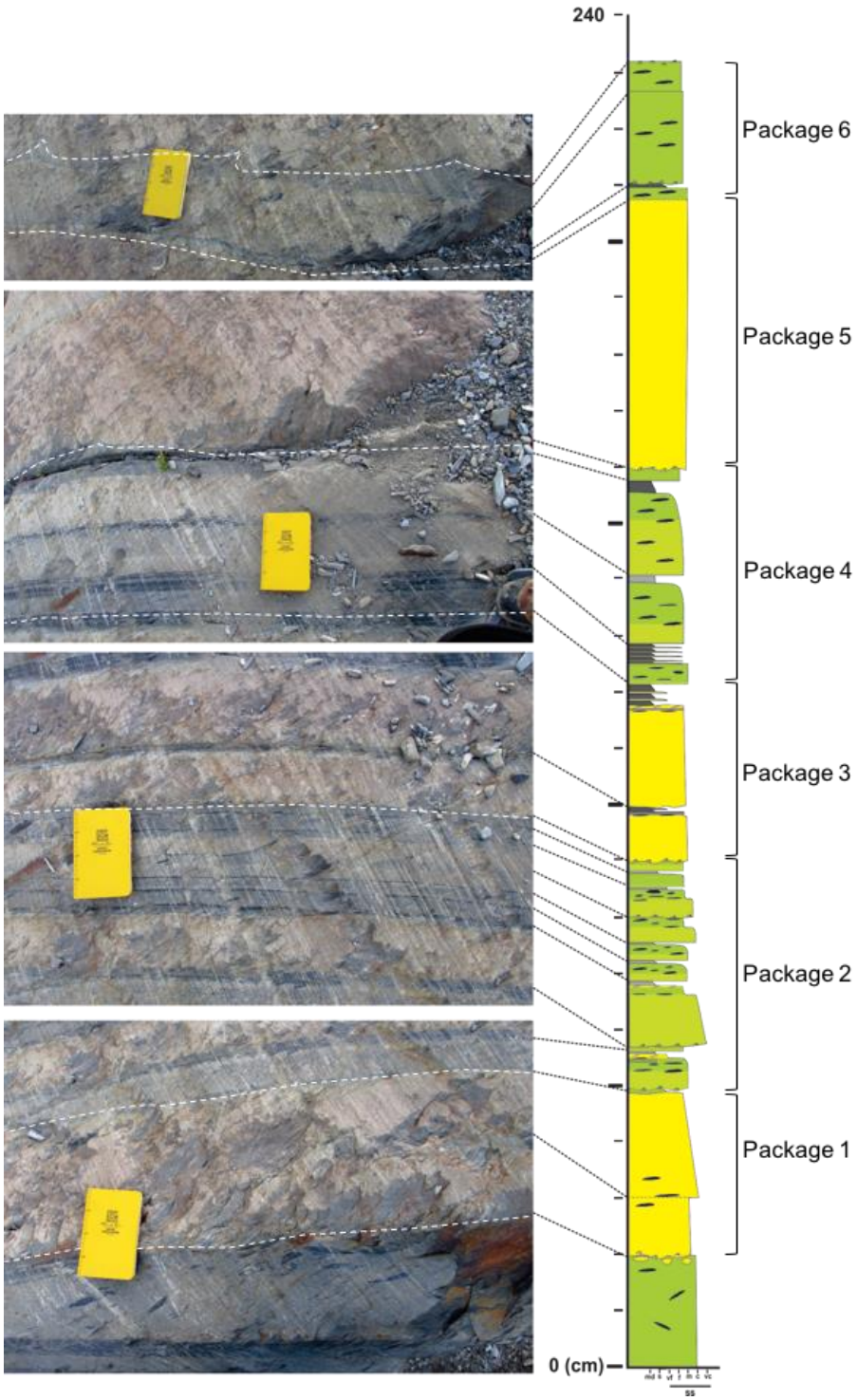

Figure 4-18 Photos and accompanying stratigraphic log of a continuous vertical section showing a stack of 6 packages, each separated by white dashed lines. Package 1, 3, and 5 consist of beds of matrix-poor sandstone, Package 2 and 4 of stacked beds of bipartite beds and Package 6 sandy claystones.

5 Vertical Facies Associations Interpretations

5.1 Summary of observations

A. Facies stack vertically to form three stratal assemblages: intercalated matrix-poor and matrix-rich strata (SA-1), exclusively matrix-rich strata (SA-2), and traction structured turbidites (SA-3).

B. SA-1 comprises multiple bedsets, each consisting of a basal matrix-poor sandstone typically overlain by 1-4 matrix-rich beds (i.e. clayey sandstone, bipartite bed, and/or sandy claystone). However, in many cases the overlying matrix-rich part is partly or completely eroded by the matrix-poor sandstone at the base of an next bedset. At the stratal assemblage scale, stacked bedsets show negligible upward change in thickness or grain size.

C. SA-2 is composed of a single bedset comprising 5-20 matrix-rich beds, each overlain by a thin-bedded, structured sandstone and claystone cap. Vertically, beds within a single bedset show little change in thickness or grain size (medium or fine sand). Additionally, successive beds change to more distal facies at about the same lateral position and in the same direction.

D. SA-3 comprises thick and thin, traction-structured turbidites that no show change in facies laterally.

E. Stratal assemblages 1 and 2 alternate vertically and are bounded sharply by units consisting of traction-structured turbidites (SA-3). Laterally, the basal matrix-poor sandstone is SA-1 will change to more distal facies, and does so in the same direction as the overlying matrix-rich strata. As a result, SA-1 laterally grades into SA-2, consequently forming a wedge shape geometry.

F. Markov chain analysis indicates that like facies and matrix-poor sandstone overlain by clayey sandstone typically succeed one another, whereas all other transitions are less than expected or random.

G. Similar facies stack to form packages of 2 to 7 beds thick. Additionally, beds within each package are similar in terms of lithology and thickness.

5.2 Interpretations of Stacking Patterns

Based on the previous observations the following depositional model is presented, which builds on the earlier models of Terlaky (2014), Arnott and Terlaky (2014), Popović (2016), and Angus (2016).

As previously discussed in chapter 4, previous studies at Castle Creek (Arnott 2007, Terlaky and Arnott 2014) have reported that matrix-rich sandstones typically underlie base-of-slope channels, basin floor terminal splays and distributary channels, which suggests that deposition of matrix-rich sandstones is related to local activation of the system, and is most likely due to avulsion of an up-dip channel. As a consequence of a channel avulsion an unconfined plane-wall jet then scoured the mud-rich sea-floor in the inter-channel area, causing flows to become locally engorged with fine sand to clay particles (Terlaky and Arnott, 2014). Near the axis of the jet, granules to coarse grains settled despite intense turbulent mixing in the dispersion. However, finer sediment consisting of medium sand to clay particles, as well as mud clasts, remained in suspension and became concentrated along the margins of the jet (Terlaky 2014).

Similar to the interpretations made by Angus (2016), the observed lateral transition from matrix-poor (F1.A) to clayey sandstone (F1.B) to bipartite bed to sandy claystone (F2) is interpreted to reflect a systematic pattern of deposition from a negligibly-sheared, sediment-laden plume that became separated from the main jet (Figure 5-1). More specifically, the interaction between the jet and the ambient fluid resulted in the development of Kelvin-Helmholtz instabilities along the margins of the jet, which in turn promoted turbulent mixing and formation of discrete sediment-laden volumes that periodically became detached from the main

jet (Figure 5-1. A). The now detached, negligibly-sheared suspension advected away from main jet and immediately began to collapse (Figure 5-1.C). Systematic particle settling resulted in the lateral facies succession outlined above and described in chapter 4.2.2. At all times the suspension was overlain by a low-density turbidity current that reworked the underlying deposit (Angus 2016). Lastly, any remaining clay particles left in suspension formed a near-bed fluid mud layer that eventually gelled depositing a mudstone cap (F4), marking the end of the depositional episode for a single lateral (facies) succession.

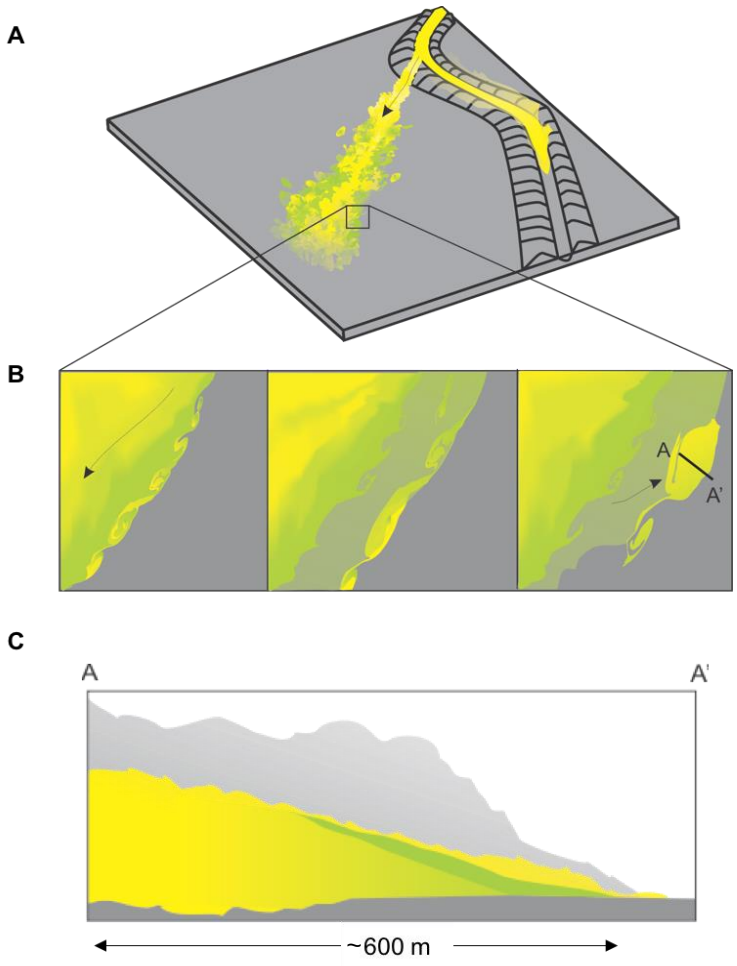

Figure 5-1. Schematic showing of the development and detachment of a sediment-laden plume from the main avulsion jet flow (adapted from Angus 2016). **A)** Avulsion jet flow scours the mud-rich seabed as it enters the interchannel area and entrains abundant sand, silt, clay and mud clasts. Medium to fine sand and mud are preferentially displaced to the margins of the jet where Kelvin-Helmholtz instabilities cause mixing with the ambient fluid. Arrow indicates flow direction of the main jet. **B)** Periodically vortices become shed from the mixing layer and advect outward (arrow indicating flow direction of ejected vortice) (laterally) from the main avulsion flow. A to A' transect indicates the cross-section in part C). **C)** The laterally advecting, negligibly sheared suspension begins to immediately collapse and deposits the systematic succession of lithofacies described in chapter 4.2.2. During a single sedimentation event (i.e. an avulsion jet flow) multiple vortices are shed from the jet. The character of the detached vortices tends to be self-similar for some length of time and results in the deposition of self-similar beds that stack to form a package. However, an abrupt change of local flow conditions, potentially during the same avulsion flow, causes the character of the vortices change and, accordingly, deposition of the next package. Figures are not to scale. See Figure 5-2 for explanation of colour code.

In the vertical succession, Markov chain analysis indicates that like facies, in addition to matrix-poor overlain by clayey sandstone, typically succeed one another whereas all other transitions are less than expected or random. Similar facies stack to form packages composed of 2-7 beds that have similar lithology and thickness. Moreover, within an individual package beds (of similar facies) transition to the next facies at about the same position laterally, and the layer as a whole pinches out at about the same location. Collectively, these observations suggest that individual beds within a single package were deposited from successive flows of similar hydraulic and compositional character. However, superimposed on this temporal regularity is the traction-structured turbidite (F3.A) overlain by mudstone (F4) that caps each bed. Each cap signals a dramatic change in sedimentation conditions, which then reverted back to the previous conditions and deposition of the next bed with similar stratal and dimensional characteristics. This stratal package is then abruptly overlain by the next package made up of 2 or more beds with a different, but nevertheless similarly consistent internal stratal makeup. Each package, then, represents deposition in a discrete but different part of the lateral facies succession. Accordingly, the boundaries separating each package represent the abrupt spatial displacement of the lateral facies succession, followed by a temporary stabilization of flow and sedimentation conditions.

As hypothesized by Terlaky (2014) and Angus (2016), deposition of the strata described here are related to vortex shedding from the lateral margins of an avulsion jet. Deposition begins with the emplacement of a coarse, graded sandstone bed (F1.A) related to a detached high-energy vortex. This, then is followed by a dramatic contraction and then stabilization of the local jet margin, made evident by a stack of 2 or more self-similar beds from a more distal part of the lateral facies transect (i.e. F1B, bipartite bed, or F2). Stabilization is temporary and marked by

the shedding of self-similar vortices that deposit a small number of self-similar beds (i.e. package). These conditions, in turn, become interrupted as conditions along the margin change, which then initiates deposition of the next package of self-similar beds, or if sufficiently dramatic and expansive, deposition of a coarse, graded sandstone. Importantly, the time between successive events, which may last as long as the interval between successive avulsion flows, or potentially also, discrete events during a single avulsion flow, must be of sufficient duration to allow for the emplacement of the structured sandstone and overlying mud cap.

Furthermore, at the decimetre to several-metre stratal assemblage scale, SA-1 and SA-2 are not only vertically, but also laterally juxtaposed. These patterns are suggestive of a lateral offset followed by temporary stabilization of the axis of flow, and therefore seabed scour (Figure 5-2). Conversely, the abrupt superposition of a thick succession of low matrix Tbcd, Tbd, and Tcd turbidites (SA-3) above SA1 or SA2, indicates a fundamental change in sedimentation conditions, specifically particle settling on the margins of an avulsion flow to bedload-transport beneath turbidity currents. In terms of paleogeographic setting, it also indicates a change from sedimentation downflow of an avulsion node to upflow diversion of the channel and general flow overspill along the margins of a younger channel. Alternatively, the abrupt change could reflect the depletion of a locally erodible mud-rich sea floor, quite possibly by being buried in sand, and as a consequence a return to more typical levee sedimentation (Figure 5-2).

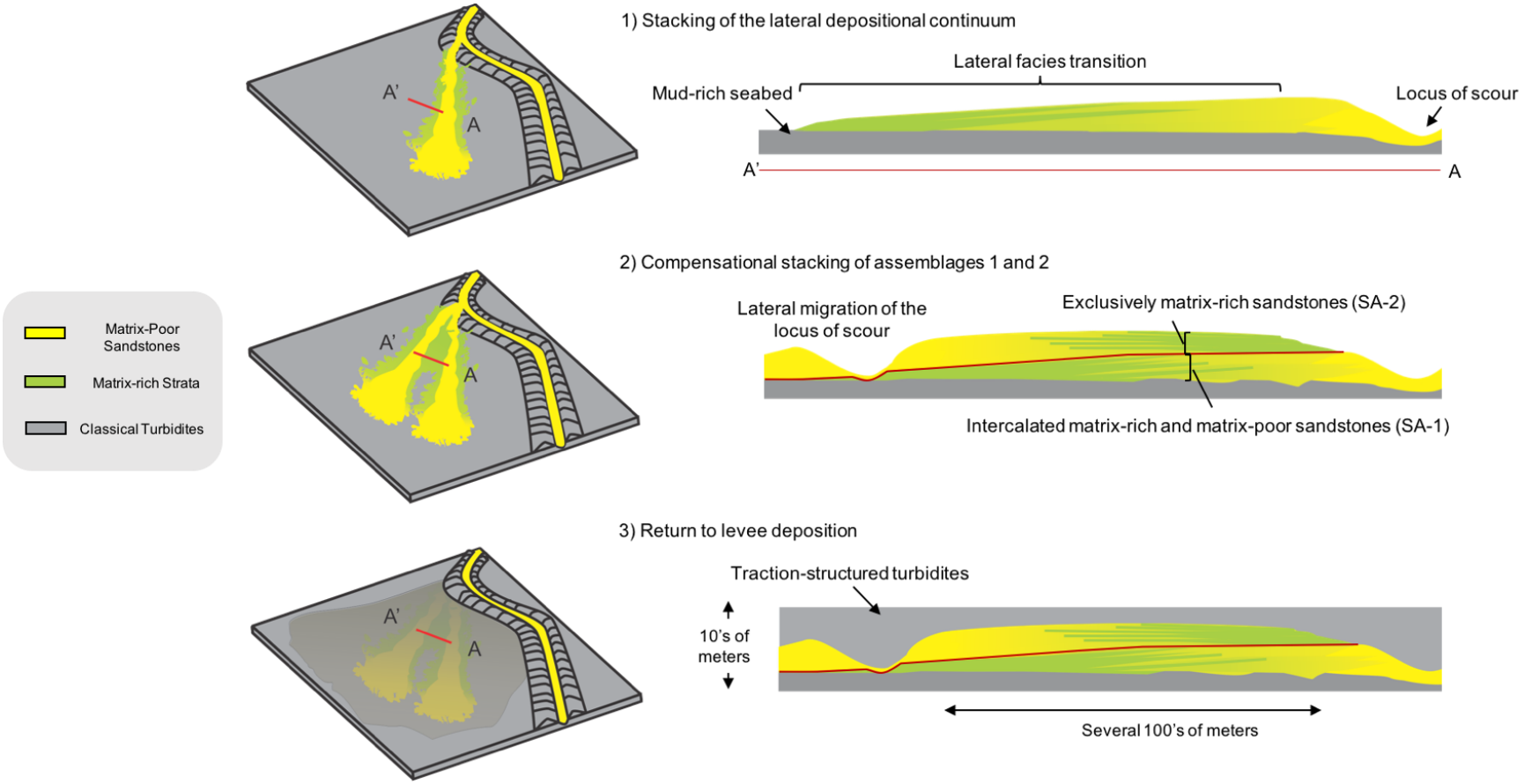

Figure 5-2. Schematic of the stacking patterns at the stratal assemblage scale. **A)** The lateral transition from SA-1 to SA-2, or vice versa, reflects spatial differences in particle settling from a mud-rich, negligibly-sheared turbulent sediment suspension. **B)** The lateral migration of the main avulsion jet results in the compensational stacking at the stratal assemblage scale. **C)** Local resumption of more typical out-of-channel conditions (i.e. levees) and the return of classical turbidites deposited from low-density, fully-sheared flows.

6 Conclusions

Deep-marine sandstones rich in detrital fine-grained (i.e. mud) matrix have become increasingly documented and their modes of deposition interpreted. Most notable are the variously named hybrid event beds, linked debrites, slurry beds, co-genetic turbidite-debrite, amongst others, that typically have been described from the distal margins of basin floor turbidite system and attributed to a transformation from fully turbulent to turbulence-modified or even turbulence-damped flow conditions. However, this work, in addition to the earlier work of Terlaky (2014), Terlaky and Arnott (2014), Popović (2016) and Angus (2016) at the Castle Creek study area, have documented mud-rich sandstones from basin floor and continental slope settings, and whose lithological characteristics and spatial trends differ from these other deep-marine mud-rich sandstones, and, therefore, suggest a potentially different physical origin. In addition to being of academic interest, these mud-rich strata exhibit poor reservoir quality (i.e. porosity and permeability) which makes understanding their origin, and therefore prediction of spatial distribution, essential for more accurately modelling (hydrocarbon) reservoir architecture and performance.

Previous work at Castle Creek (see references above) has focused on the lateral aspects of these strata and documenting their systematic facies changes. This work focuses on the vertical development of these strata, and therefore documenting changes in time rather than space.

Like Angus (2016), detailed thin section analyses, outcrop descriptions and stratigraphic correlations have identified a systematic lateral change in lithofacies. In the most proximal part of the lateral facies succession a scour based, normally graded or massive, structureless, <20% matrix, matrix-poor sandstone (F1.A) transforms laterally into a scour based, massive to

normally graded, 20-50% matrix, structureless, clayey sandstone (F1.B). Further laterally, a sharp planar interface develops separating the clayey sandstone (F1.B) from an upper layer composed of matrix-rich (50-70% matrix), massive, structureless, sandy claystone (F2). Collectively, these two parts form a single bed termed a bipartite bed. Laterally, the basal clayey sandstone (F1.B) progressively thins as the upper sandy claystone (F2) thickens. Eventually, the basal clayey sandstone (F1.B) pinches out, leaving the sharp based, massive, sandy claystone (F2), which then similarly thins and pinches out. The entire lateral facies succession is then overlain by a thin-bedded, traction-structured sandstone (F3.A) capped by a massive to graded mudstone cap (F4).

Vertically, Markov chain analysis indicates similar facies tend to preferentially overlie one another. These beds of like facies then stack to form packages comprising 2-7 beds with similar lithology and thickness. Also notable are beds within an individual package that pinch out and change laterally to the next facies at about the same position. A single stratal package is then abruptly overlain by the next package made up of 2 or more beds with a different, but nevertheless similarly consistent internal stratal makeup. Importantly, all beds, similar or not, are separated by a traction-structured turbidite (F3.A) overlain by mudstone (F4), indicating a time lag between the deposition of each bed.

As suggested earlier by Terlaky (2014) and Angus (2016), deposition of the strata described here are related to vortex shedding from the lateral margins of a turbulent jet related to an upflow channel avulsion. The lateral facies succession is interpreted to reflect deposition from a negligibly-sheared, sediment-laden plume that became separated from the main avulsion flow. The now detached, negligibly-sheared suspension advected away from main jet and immediately began to collapse. Initially, the upward component of turbulence was the primary sediment

support mechanism, enabling particles to settle according to their fall velocity. However, as the suspension moved further away from the main jet and collapsed toward the bed, hindered settling became increasingly important and eventually became the primary sediment support mechanism. Specifically, the downward (constant) mass flux of settling particles resulted in the upward displacement of ambient fluid and easily suspended fine-grained sediment and low-density mud clasts. The buildup of this fine sediment in the upper part of the collapsing suspension formed the sharply-defined sandy clay(stone) layer in the upper part of a bipartite bed. Eventually the basal part of the suspension became completely depleted of sediment through deposition as the upper part continually accumulated clay and developed cohesive matrix strength. The now exclusively mud-rich flow resembled a viscous plug flow, which like the now deposited basal layer, thinned and then pinched out. At all times the suspension was overlain by a low-density turbidity current that formed a well-sorted, traction-structured layer made up of sediment reworked from the underlying deposit (i.e. lateral facies succession). Lastly, any clay that remained in suspension settled forming a near-bed fluid mud layer that eventually gelled depositing a mudstone cap (F4) that marks the end of a single depositional event.

Vertically, deposition begins with the emplacement of a coarse, graded sandstone (F1.A) related to the local introduction of a single high-energy, sediment-laden vortex. This was then abruptly followed by a dramatic contraction of the jet margin and the episodic detachment of self-similar vortices that deposited a 2-7 bed-thick package made up of similar facies. Importantly, time between successive depositional events (i.e. each bed) was of sufficient duration to allow for the emplacement of the structured sandstone and overlying mudstone cap. Systematic stacking patterns are observed also at a larger scale and the lateral and vertical juxtaposition of stratal assemblages SA1 and SA2. This larger scale pattern is interpreted to

reflect the abrupt lateral displacement of the axis of the main avulsion jet followed by a period of temporary stabilization. These avulsion-related strata are then abruptly overlain by a thick stack of classical turbidites (SA-3), which suggests that sedimentation downflow of the avulsion node had been terminated, most probably due to a upflow avulsion, and a return to more typical extrachannel deposition, specifically levee growth. Alternatively, the abrupt superposition of SA3 turbidites could reflect the depletion of a locally erodible mud-rich sea floor, quite possibly due to scour down to a sufficiently compacted subsurface layer, or simply being buried in sand.

6.1 Future Research

A. Compare the vertical stacking patterns of the matrix-rich sandstones described here with other matrix-rich sandstones in the Windermere, but also those reported from other ancient and modern deep-marine basins.
B. Paleocurrent data were not collected in this study, in part because cross-stratification in Facies 3.A is uncommon, poorly exposed and therefore poorly defined and, where present, difficult to assess because of the two-dimensionality of the outcrop. The use of a rock saw and cutting surfaces at multiple angles to the outcrop surface should improve the visibility of the cross-stratification, and thereby make possible more accurate assessment of paleocurrent direction. These data can then be compared to the present interpretation of proximal versus distal, based strictly on changes in lithology (i.e. the lateral facies succession).
C. The use of a Markov chain analysis assumes that the succession exhibits no preservational bias, or stated more simply, once deposited a bed is not removed

by a later event. While appearing to be satisfied in the more distal part of lateral facies succession, the stacking of graded sandstone beds in the most proximal part is suggestive of post-depositional erosion. Therefore, measuring a section where evidence of erosion is absent could provide validation of the analysis performed here.

D. Experimental work focused on mud-rich plane-wall jets, especially mixing characteristics along their lateral margins.

7 References

Aalto, K.R. 1971. Glacial Marine Sedimentation and Stratigraphy of the Toby Conglomerate (Upper Proterozoic), Southeastern British Columbia, Northwestern Idaho and Northeastern Washington. Canadian Journal of Earth Sciences, 8: 753–787. NRC Research Press Ottawa, Canada . doi:10.1139/e71-073.

Aitken, J.D. 1969. Documentation of the sub-Cambrian unconformity, Rocky Mountains Main Ranges, Alberta. Canadian Journal of Earth Sciences, 6: 193–200. NRC Research Press Ottawa, Canada . doi:10.1139/e69-018.

Amy, L.A., Peachey, S.A., Gardiner, A.A., and Talling, P.J. 2009. Prediction of hydrocarbon recovery from turbidite sandstones with linked-debrite facies: Numerical flow-simulation studies. Marine and Petroleum Geology, 26: 2032–2043. doi:10.1016/j.marpetgeo.2009.02.017.

Amy, L.A., Talling, P.J., Edmonds, V.O., and Sumner, E. 2006. An experimental investigation of sand – mud suspension settling behaviour : implications for bimodal mud contents of submarine flow deposits. : 1411–1434. doi:10.1111/j.1365-3091.2006.00815.x.

Angus, K. 2016. Lateral facies trends in deep-marine slope and basin floor matrix-rich beds, Neoproterzoic Windermere Supergroup, British Columbia, Canada (Master's Thesis). University of Ottawa, Ottawa.

Aniekwena, A.U., McVay, A.D., Anr, W.M., Watkins, J.S., 2003. Integrated Characterization of the Thin-bedded 8 Reservoir, Green Canyon 18, Gulf of Mexico. SPE, 84051, pp. 1–11.

Arnott, R, W, C. 2007. Stratigraphic architecture and depositional processes of a proximal crevasse splay and genetically related, sinuous channel fill, Isaac Formation, Brithish Columbia, Canada. In Atlas of deep-water outcrops: AAPG Studies in Geology. *Edited by* T.H. Nilsen, R.D. Shew, G.. Steffens, and J.R.J. Studlick. AAPG Studies in Geology. p. 12.

Arnott, R.W.C. 2010. Deep-marine sediments and sedimentary systems. Facies models, 4: 295–322.

Arnott, R.W.C. 2012. Turbidites, and the case of the missing dunes. Journal of Sedimentary Research, 82: 379–384. doi:10.2110/jsr.2012.29.

Arnott, R.W.C., and Hand, B.M. 1989. Bedforms, primary structures and grain fabric in the presence of suspended sediment rain. Journal of Sedimentary Petrology, 59: 1062–1069.

Arnott, R.W.C., and Hein, F.J. 1986. Submarine canyon fills of the Hector Formation, Lake Louise, Alberta: Late Precambrian syn-rift deposits of the proto-Pacific miogeocline.

Baas, J.H., and Best, J.L. 2002. Turbulence modulation in clay-rich sediment-laden flows and some implications for sediment deposition. Journal of Sedimentary Research, 72: 336–340.

Baas, J.H., Best, J.L., and Peakall, J. 2011. Depositional processes , bedform development and hybrid bed formation in rapidly decelerated cohesive (mud – sand) sediment flows. Sedimentology, 58: 1953–1987. doi:10.1111/j.1365-3091.2011.01247.x.

Berlamont, J., Ockenden, M., Toorman, E., and Winterwerp, J. 1993. The characterisation of cohesive sediment properties. Coastal Engineering, 21: 105–128.

Best, J.I.M. 1992. On the entrainment of sediment and initiation of bed defects: insights from recent developments within turbulent boundary layer research. Sedimentology, 39: 797–811.

Bouma, A.H. 1962. Sedimentology of Some Flysch Deposits. A graphic approach to facies interpretation. Elsevier Publishing Company.

Bouma, A.H. 1985. Submarine Fans and Related Turbidite Systems. Springer-Verlag, New York.

Brown, R.L., Tippett, C.R., and Lane, L.S. 1978. Stratigraphy, facies changes, and correlations in the northern Selkirk Mountains, southern Canadian Cordillera. Canadian Journal of Earth Sciences, 15: 1129–1140. NRC Research Press Ottawa, Canada . doi:10.1139/e78-119.

Campbell, R., Mountjoy, E., and Young, F.. 1973. Geology of the McBirde map-area, Brithish Columbia. Geological Survey of Canada,: 72–35.

Charlesworth, H.A.K., and Remington, D.B. 1960. Precambrian rocks in the vicinity of Jasper, Alberta. Edmonton Geological Society, Second Annual Field Trip Guide Book.

Charlesworth, H.A.K., Weiner, J.L., Akehurst, A.J., Bielenstein, H.U., Evans, C.R., Griffiths, R.E., Remington, R.E., Stauffer, M.R., and Steiner, J. (n.d.). Precambrian geology of the Jasper region, Alberta. Research Council of Alberta Bulletin, 23: 74.

Chien, N., and Wan, Z. 1999. Mechanics of Sediment Transport. American Society of Civil Engineers, Reston, Virginia.

Colpron, M., Logan, J.M., and Mortensen, J.K. 2002. U-Pb zircon age constraint for late Neoproterozoic rifting and initiation of the lower Paleozoic passive margin of western Laurentia. Canadian Journal of Earth Sciences, 39: 133–143. doi:10.1139/e01-069.

Davies, R. 1968. The experimental study of the differential settling of particles in suspension at high concentrations. Powder Technology, 2: 43–51. doi:10.1016/0032-5910(68)80032-4.

Davies, R. 1988. Hindered settling of ... semidilute suspensions. AIChE Journal, 34: 123–129. doi:10.1002/aic.690340114.

Davis, L. 2011. Architecture of deep-marine interchannel deposits: Isaac Formation, Windermere Supergroup (Neoproterozoic), southern Canadian Cordillera (Master's thesis). University of Ottawa, Canada.

Davis, L., and Leena. 2011. Architecture of Deep-Marine Interchannel Deposits: Isaac Formation, Windermere Supergroup (Neoproterozoic), Southern Canadian Cordillera. Université d'Ottawa / University of Ottawa.

Devlin, W.J., Brueckner, H.K., and Bond, G.C. 1988. New isotopic data and a preliminary age for volcanics near the base of the Windermere Supergroup, northeastern Washington, U.S.A. Canadian Journal of Earth Sciences, 25: 1906–1911.

Dorrell, R.M., and Hogg, A.J. 2010. International Journal of Multiphase Flow Sedimentation of bidisperse suspensions. International Journal of Multiphase Flow, 36: 481–490. doi:10.1016/j.ijmultiphaseflow.2010.02.001.

Dorrell, R.M., Hogg, A.J., and Pritchard, D. 2013. Polydisperse suspensions : Erosion , deposition , and flow capacity. Journal of Geophysical Research: Earth Surface, 118: 1939–1955. doi:10.1002/jgrf.20129.

Dorrell, R.M., Hogg, A.J., Sumner, E., and Talling, P.J. 2011. The structure of the deposit produced by sedimentation of polydisperse suspensions. Journal of Geophysical Research: Earth Surface, 116: 1–12. doi:10.1029/2010JF001718.

Druitt, T.H. 1995. Settling behaviour of concentrated dispersions and some volcanological applications. Journal of Volcanology and Geothermal Research, 65: 27–39. doi:10.1016/0377-0273(94)00090-4.

Dumouchel, I.G. 2015. Stratigraphic Architecture and Depositional History of laterally-accreted channel fills in the Lower Isaac Formation, Windermere Supergroup, British Columbia, Canada. Department of Earth Sciences, MSc: 108.

Enos, P. 1969. Shell Development Company, Exploration and Production Research Center, Houston, Texas. 39.

Evans et al., 2000. Evans K.V., Aleinikoff J.N., Obradovich J.D., F.C.M. 2000. SHRIMP U-Pb geochronology of volcanic rocks, Belt Supergroup, western Montana: evidence for rapid deposition of sedimentary strata. Canadian Journal of Earth Sciences, 37: 1287–1300.

Evenchick, C.A., Parrish, R.R., Survey, G., Street, B., Ka, O., Gabrielse, H., and Lake, F. 1984. Precambrian gneiss and late Proterozoic sedimentation in north-central British Columbia: 233–237.

Ferguson, C.A. 1994. Structural geology and stratigraphy of the northern Cariboo Mountains between Isaac Lake and Fraser River, British Columbia. Map, Univsersity of Calgary, Calgary, AB, Canada.

Fisher, R.V. 1971. Features of coarse-grained, high-concentrated fluids and their deposits. Journal of Sedimentary Petrology, 41: 916–927.

Gabrielse, H., & Campbell, R.B. 1991. Upper Proterozoic assemblages. In H. Gabrielse & C. J. Yorath (Eds.), Geology of the Cordilleran Orogen in Canada (125-150). Geological Society of America, Geology of North America, G-2., 150: 127–150.

Grasby, S.E., and Brown, R.L. 1993. New correlations of the Hadrynian Windermere Supergroup in the northern Selkirk Mountains, British Columbia. Geological Survey of Canada, 93–1A: 199–206.

Gussow, W.C. 1956. Lipalian Interval evaluated (Canada). Geological Society of America Bulletin, 67: 1702.

Gussow, W.C. 1957. Cambrian and Precambrian geology of southern Alberta. In Alberta Society of Petroleum Geologists Guidebook, Seventh Annual Field Conference. pp. 7–19.

Haughton, P., Barker, S.P., and Mccaffrey, D. 2003. “Linked” debrites in sand-rich turbidite systems - origin and significance. Sedimentology, 50: 459–482. doi:10.1046/j.1365-3091.2003.00560.x.

Haughton, P., Davis, C., McCaffrey, W., and Barker, S. 2009. Hybrid sediment gravity flow deposits–classification, origin and significance. Marine and Petroleum Geology, 26: 1900–1918.

Heezen, B.C., and Ewing, M. 1952. Turbidity currents and submarine slumps, and the 1929 Grand Banks Earthquake. doi:10.2475/ajs.250.12.849.

Iverson, R.. 1997. Physics of debris flows. Reviews of Geophysics, 35: 245–296.

Kane, I.A., and Pontén, A.S.M. 2012. Submarine transitional flow deposits in the Paleogene Gulf of Mexico. Geology, 40: 1119–1122. doi:10.1130/G33410.1.

Kendall, B.S., Creaser, R.A., Ross, G.M., and Selby, D. 2004. Constraints on the timing of Marinoan “Snowball Earth” glaciation by 187Re-187Os dating of a Neoproterozoic, post-glacial black shale in Western Canada. Earth and Planetary Science Letters, 222: 729–740. doi:10.1016/j.epsl.2004.04.004.

Kubli, T.E. 1990. Geology of the Dogtooth Range, northern Purcell Mountains, British Columbia (Doctroral dissertation). University of Calgary, Calgar, Alberta.

Kubli, T.E. 1994. The Dogtooth Duplex, a model for the structural development of the northern Purcell Mountains. Canadian Journal of Earth Sciences, 31: 1672–1686.

Kubli, T.E., and Simony, P.S. 1992. The Dogtooth High, northern Purcell Mountains, British Columbia. Bulletin of Canadian Petroleum Geology, 40: 36–51.

Kuenen, P.H., and Migliorini, C.I. 1950. The Journal of Geology. 58: 91–127.

Leclair, S.F., and Arnott, R.W.C. 2003. Coarse-tail graded, structureless strata: Indicators of an internal hydraulic jump. SEPM, Gulf Coast Section, Houston.

Link, P.. 1993. Middle and Late Proterozoic stratified rocks of the western U.S. Cordillera, Colorado Plateau, and Basin and Range provinces. Geological Society of America, C-2: 463–595.

Lockett, M.., and Al-Habbooby, H.. 1974. Relative particle velocities in two-species settling. Powder Technology: 67–71.

Lowe, D.R., and Guy, M. 2000. Slurry-flow deposits in the Britannia Formation (Lower Cretaceous), North Sea: a new perspective on the turbidity current and debris flow problem. Sedimentology, 47: 31–70. doi:10.1046/j.1365-3091.2000.00276.x.

Lund, K., Aleinikoff, J.N., Evans, K. V., and Fanning, C.M. 2003. SHRIMP U-Pb geochronology of Neoproterozoic Windermere Supergroup, central Idaho: Implications for rifting of western Laurentia and synchroneity of Sturtian glacial deposits. Geological Society of America Bulletin, 115: 349–372.

McAnally, W.H., Friedrichs, C., Hamilton, D., Hayter, E., Shrestha, P., Rodriguez, H., Sheremet, A., and Teeter, A. 2007. Management of fluid mud in estuaries, bays, and lakes. i: present state of understanding on character and behavior. Journal of Hydraulic Engineering, 133: 9–22. doi:10.1061/(ASCE)0733-9429(2007)133:1(9) CE.

McDonough, M.R. 1989. The structural geology and strain history of the northern Selwyn Range, Rocky Mountains, near Valemount, British Columbia (Doctoral dissertation). University of Calgary, Calgary, Alberta.

McDonough, M.R., and Murphy, D.C. 1994. Geology and structure cross-sections, Valemount, British Columbia (1:50 000). Geological Survey of Canada,.

Monger, J.W.H., Price, R.A., and Tempelman-Kluit, D.J. 1982. Tectonic accretion and the origin of the two major metamorphic and plutonic welts in the Canadian Cordillera.

Mulder, T., and Alexander, J. 2001. The physical character of subaqueous sedimentary density flow and their deposits. Sedimentology, 48: 269–299. Blackwell Science Ltd. doi:10.1046/j.1365-3091.2001.00360.x.

Murphy, D.C. 1987a. Suprastructure/infrastructure transition, east-central Cariboo Mountains, British Columbia: geometry, kinematics and tectonic implications. doi:10.1016/0191-8141(87)90040-X.

Murphy, D.C. 1987b. Kaza Group, eastern Wells Gray Park, British Columbia. Current research, part A. Geological Survey of Canada, Paper,: 735–742.

Murphy, D.C., and Rees, C.J. 1983. Structural transition and stratigraphy in the Cariboo Mountains, British Columbia. Paper - Geological Survey of Canada, 83–1a: 245–252.

Narbonne, G.M., and Aitken, J.D. 1995. Neoproterozoic of the Mackenzie Mountains, northwestern Canada. Precambrian Research, 73: 101–121. Elsevier. doi:10.1016/0301-9268(94)00073-Z.

Navarro, L. 2016. Stratigraphic architecture, depositional processes and reservoir implications of the basin floor to slope transition, Neoproterozoic Windermere turbidite system, Canada. University of Ottawa.

Normark, W. R. Piper, D.J.. 1991. Initiation processes and flow evolution of turbidity currents: implications for the depositional record. Marine Geology.

Van Olphen, H. 1964. Internal mutual flocculation in clay suspensions. Journal of Colloid Science, 19: 313–322.

Parrish, R.R., and Scammell, R.J. 1988. The age of the Mount Copeland syenite gneiss and its metamorphic zircons, Monashee complex, southeastern British Columbia. Radiogenic age and isotopic studies: Report, 2: 82–88.

Perret, D., Locat, J., and Leroueil, S. 1995. Strength development with burial in fine-grained sediments from the Saguenay Fjord, Quebec. Canadian Geotechnical Journal, 32: 247–262. doi:10.1139/t95-027.

Pettingill, H.S., and Weimer, P. 2002. Global deep water exploration: Past, present and future frontiers. The Leading Edge, 21: 371–376.

Piper, D.J.W., and Normark, W.R. 2009. Processes that initiate turbidity currents and their influence on turbidites: A marine geology perspective. Journal of Sedimentary Research, 79: 347–362. SEPM Society for Sedimentary Geology. doi:10.2110/jsr.2009.046.

Popović, N. 2016. Sedimentology and stratigraphy of a matrix-poor to matrix-rich depositional continuum in proximal basin floor strata, upper Kaza Group, Windermere Supergroup, B.C., Canada (Master's thesis). University of Ottawa, Canada.

Posamentier, H.W., and Kolla, V. 2003. Seismic geomorphology and stratigraphy of depositional elements in deep-water settings. Journal of Sedimentary Research, 73: 367–388.

Posamentier, H.W., and Walker, R.G. 2007. Deep water turbidites and submarine fans. *In* Facies Models Revisited, 84th edition. SEPM Special Publication. pp. 399–520.

Postma, G., Nemec, W., and Karen Kleinspehn. 1988. Large floating clasts in turbidites : a mechanism for their emplacement. Sedimentary Geology, 58: 47–61.

R. Lowe, D. 1982. Sediment gravity flows : ii. Depositional models with special reference to the deposits of high-density turbidity currents. Journal of Sedimentary Petrology, 52: 279–297.

R. Lowe, D., Guy, M., and Palfrey, A. 2003. Facies of slurry-flow deposits, Britannia Formation (Lower Cretaceous), North Sea: implications for flow evolution and deposit geometry. Sedimentology, 50: 45–80. doi:10.1046/j.1365-3091.2003.00507.x.

Reedy, G.K., Pepper, C.F., 1996. Analysis of finely laminated deep marine turbidites: integration of core and log data yields novel interpretation model. In: Proceedings of the Society of Petroleum Engineers (SPE) Annual Technical Conference and Exhibition, pp. 119–127.

Reid, L.F., Simony, P.S., and Ross, G.M. 2002. Dextral strike-slip faulting in the Cariboo Mountains, British Columbia: a natural example of wrench tectonics in relation to Cordilleran tectonics. Canadian Journal of Earth Sciences, 39: 953–970. doi:10.1139/e02-017.

Richardson, J.F., and Zaki, W.N. 1954. Sedimentation and Fluidisation: Part I. Chemical Engineering Research and Design, 32. Institution of Chemical Engineers. doi:10.1016/S0263-8762(97)80006-8.

Rocheleau, J. 2012. Depositional architecture of a near-slope turbidite succession: Upper Kaza Group, Windermerer Supergroup, Castle Creek, British Columbia, Canada (Masters Thesis). University of Ottawa, Ottawa.

Root, K.G. 1987. Geology of the Delphine Creek area, southeastern British Columbia: implications for the Proterozoic and Paleozoic development of the Cor- dilleran divergent margin. University of Calgary.

Ross, G. M., Arnott, R.. 2007. Regional geology of the Windermere Supergroup, southern Canadian Cordillera and stratigraphic setting of the Castle Creek study area, Canada. doi:1054646546881d6f468646.

Ross, G. M., McMechan M.E., Hein, F.. 1989. Proterozoic history: the birth of the miogeocline. Canadian Society of Petroleum Geologists, 79–104.

Ross, G.M. 1991. Tectonic setting of the Windermere Supergroup revisited. Geology, 19: 1125. Geological Society of America.

Ross, G.M., Bloch, J.D., and Krouse, H.R. 1995. Neoproterozoic strata of the southern Canadian Cordillera and the isotopic evolution of seawater sulfate. doi:10.1016/0301-9268(94)00072-Y.

Ross, G.M., and Ferguson, C.A. 2003a. Geology and structure cross-sections, Eddy, British Columbia.

Ross, G.M., and Ferguson, C.A. 2003b. Geology and structure cross-sections, Lanezi Lake, British Columbia; Geological Survey of Canada, "A" Series Map, 2001A, scale 1:50,000, 1 sheet.

Ross, G.M., and Murphy, D.C. 1988. Transgressive stratigraphy, anoxia, and regional correlations Within the late Precambrian Windermere grit Of the southern Canadian Cordillera. Geology, 16: 139. Geological Society of America.

Ross, G.M., and Parrish, R.R. 1991. Detrital zircon geochronology of metasedimentary rocks in the southern Omineca Belt, Canadian Cordillera. Canadian Journal of Earth Sciences, 28: 1254–1270. NRC Research Press Ottawa, Canada. doi:10.1139/e91-112.

Rubey, W.W. 1933. Settling velocity of gravel, sand, and silt particles. American Journal of Science, s5-25: 325–338. doi:10.2475/ajs.s5-25.148.325.

Schwarzacher, W. 1975. Sedimentation models and quantitative stratigraphy. *In* Developments in Sedimentology. Elsevier, The Queens University, Belfast, Northern Ireland. pp. 91–121. doi:10.1016/S0070-4571(08)70371-6.

Shanmugam, G. 1996. High-density turbidity currents; are they sandy debris flows? Journal of Sedimentary Research, 66: 2–10. doi:10.1306/D426828E-2B26-11D7-8648000102C1865D.

Shanmugam, G. 2006. Deep-water processes and facies models: Implications for sandstone petroleum reservoirs. Elsevier, New York.

Smith, M.D., Arnott, R.W.C., and Ross, G.M. 2014. The old fort point formation: Redefinition and formal subdivision of a distinctive stratigraphic marker in the neoproterozoic windermere supergroup, southern Canadian cordillera. Bulletin of Canadian Petroleum Geology, 62: 1–13.

Smits, A. 2000. A physical introduction to fluid mechanics. John Wiley, The University of California.

Spurk, H.J., and Aksel, N.A. 2008. Fluid Mechanics. Springer Berlin Heidelberg, Berlin, Heidelberg. doi:10.1007/978-3-540-73537-3.

Stewart, J.H. 1972. John h. stewart. Geological Society of America Bulletin, 83: 1345–1360.

Stipp, M., Stunitz, H., Heilbronner, R., and Stefan, S. 2002. The eastern Tonale fault zone :a natural laboratory for crystal plastic deformation of quartz over a temperature range from 250 to 700 8 C. Journal of Structural Geology, 24: 1861–1884.

Stow, D., and Bowen, A. 1978. Origin of lamination in deep sea, fine-grained sediments. Nature, 274: 324–328.

Sumner, E., Lawrence, A., and Talling, P.J. 2008. Deposit structure and processes of sand deposition from decelerating sediment suspensions. Journal of Sedimentary Research, 78: 529–547. doi:10.2110/jsr.2008.062.

Sumner, E., Talling, P.J., and Amy, L.A. 2009. Deposits of flows transitional between turbidity current and debris flow. Geology, 37: 991–994. doi:10.1130/G30059A.1.

Talling, P.J., Amy, L.A., Wynn, R.B., Peakall, J., and Robinson, M. 2004. Beds comprising debrite sandwiched within co-genetic turbidite: Origin and widespread occurrence in distal depositional environments. Sedimentology, 51: 163–194. doi:10.1111/j.1365-3091.2004.00617.x.

Talling, P.J., Masson, D.G., Sumner, E., and Malgesini, G. 2012. Subaqueous sediment density flows: Depositional processes and deposit types. Sedimentology, 59: 1937–2003. Blackwell Publishing Ltd. doi:10.1111/j.1365-3091.2012.01353.x.

Terlaky, V. 2014. Sedimentology, stratigraphy, architecture and origin of deep-water, basin-floor deposits: middle and upper Kaza Group, Windermere Supergroup, B.C., Canada (Doctoral dissertation). University of Ottawa, Canada.

Terlaky, V., and Arnott, R.W.C. 2014. Matrix-rich and associated matrix-poor sandstones: Avulsion splays in slope and basin-floor strata. Sedimentology, 61: 1175–1197. doi:10.1111/sed.12096.

Terlaky, V., Rocheleau, J., Arnott, R.W.C., and Talling, P.J. 2016. Stratal composition and stratigraphic organization of stratal elements in an ancient deep-marine basin-floor succession, Neoproterozoic Windermere Supergroup, British Columbia, Canada. Sedimentology, 63: 136–175. doi:10.1111/sed.12222.

Tucker, M.E. 1981. Sedimentary Petrology: An introduction.

Walcott, C.D. 1910. Pre-cambrian rocks of the Bow River Valley, Alberta, Canada. Smithsonian Miscellaneous Collections, 53: 423–431.

Warren, M.J. 1996. Geology of the west-central Purcell Mountains, B.C.

Warren, M.J. 1997. Crustal extension and subsequent crustal thickening along the Cordilleran rifted margin of ancestral North America, western Purcell Mountains, southeastern British Columbia (Doctoral dissertation). Queen's University, Kingston, Ontario.

Wilson, M.D., and Pittman, E.D. 1977. Authigenic clays in sandstones: recognition and influence on reservoir properties and paleoenvironmental analysis. Journal of Sedimentary Petrology, 47: 3–31.